NTNU

Norwegian University of
Science and Technology

Welding on Power Pylons in Aluminium

Sigurd Guddal

Civil and Environmental Engineering
Submission date: May 2016
Supervisor: Magnus Langseth, KT
Co-supervisor: Marius Endre Holtermann Andersen, KT

Norwegian University of Science and Technology
Department of Structural Engineering

Department of Structural Engineering
Faculty of Engineering Science and Technology
NTNU – Norwegian University of Science and Technology

ACCESSIBILITY

Open

MASTER THESIS 2016

SUBJECT AREA:	DATE:	NO. OF PAGES: 143
Structural Engineering	25.05.2016	18 + 125

TITLE:

Welding on Power Pylons in Aluminium

Sveising på høgspentmaster i aluminium

BY:

Sigurd Guddal

SUMMARY:

This thesis is written at Structural Impact Laboratory (SIMLab) and Center of Advanced Structural Analysis (CASA) in collaboration with Statnett.

The structural behaviour of aluminium subjected to compression load is investigated for both unwelded and welded cylinders for two different alloys, 6060-T6 and 6082-T6. Only short cylinders are tested in the laboratory, where local buckling is dominating. Laboratory experiments and numerical analysis are performed and compared with regulations from Eurocode 9: Design of Aluminium Structures. The laboratory and numerical results fits very well and the deformation modes are perfectly recreated in the numerical analysis. Compared to EC9, the cylinders tested resists up to twice the load calculated from EC9, depending on whether f_o is taken from EC9 or tensile tests performed in this thesis.

The material parameters for the two alloys are found from classical tensile tests, but in the vicinity of a weld, or the so-called heat affected zone (HAZ), the material parameters are found from previous studies where hardness tests have been conducted.

RESPONSIBLE TEACHER: Magnus Langseth

SUPERVISOR(S): Magnus Langseth and Marius Andersen

CARRIED OUT AT: Norwegian University of Science and Technology (NTNU)

Institutt for konstruksjonsteknikk

FAKULTET FOR INGENIØRVITENSKAP OG TEKNOLOGI

NTNU – Norges teknisk-naturvitenskapelige universitet

MASTEROPPGAVE 2016

for

Sigurd Guddal

Sveising på høyspentmaster i aluminium

Welding on power pylons in aluminum

Statnett ønsker å vurdere bruk av aluminium som konstruksjonsmateriale i høyspentmaster. Enkle beregninger basert på EC9 indikerer en totalvekt på ca 5500 kg for en aluminiummast sammenlignet med 9100 kg for en tilsvarende mast i stål. Foreløpige vurderinger indikerer at denne vektbesparelsen ikke gir tilstrekkelig kostnadsbesparelse til at dette er et interessant prosjekt for Statnett. Dette synliggjør behovet for mere nøyaktige verktøy hvor en optimal kombinasjon av material og geometri kan etableres. Avanserte FEM beregninger tilpasset aluminium som konstruksjonsmateriale kan være et alternativ for å få en tilfredsstillende vektbesparelse.

Denne oppgaven er en del av dette prosjektet. Målet med oppgaven er å etablere validerte numeriske analysemodeller for søyler i aluminium hvor interaksjon mellom lokal og global knekking inntreffer. I dette ligger også en vurdering av hvordan varmepåvirket sone (HAZ) ved opplegg og i felt vil påvirke kapasiteten og hvordan dette skal modelleres. De numeriske analysene skal valideres mot utførte forsøk og vurderes opp mot beregninger etter EC9.

Følgende foreløpige plan er definert for denne oppgaven:

- Det skal gjennomføres et litteraturstudium knyttet til oppførsel og modellering av søyler i aluminium utsatt for aksiallast, samt innvirkningen HAZ har på materialegenskapene og kapasiteten til søylen. Det skal spesielt legges vekt på søyler med sirkulært tverrsnitt.
- Kandidatene skal delta i planlegging og gjennomføring av forsøk i laboratoriet på sveiste og ikke sveiste rør og materialprøver
- Det skal etableres numerisk modeller for global knekking som skal valideres mot de testene som er utført.
- De validerte numeriske modellene skal brukes i et parameterstudie hvor effekter av HAZ-plassering og HAZ-geometrie skal evalueres.
- Predikerte HAZ-effekter skal sammenlignes med beregninger etter EC9.
- Rapportering.

Veiledere: Magnus Langseth og Marius Andersen

Kandidatene kan fravike den foreslåtte plan, men kun etter avtale med veilederne. Hovedoppgaven skal skrives på engelsk og utformes som en forskningsrapport og i henhold til gjeldende regler for en hovedoppgave. Oppgaven skal leveres til Institutt for konstruksjonsteknikk, NTNU innen 14. juni 2016.

NTNU, 14. januar 2016

Magnus Langseth,

Professor

Acknowledgements

This master thesis was written at Structural Impact Laboratory (SIMLab) and Center of Advanced Structural Analysis (CASA) – Center for Research-based Innovation in collaboration with Statnett. SIMLab and CASA is located at the Department of Structural Engineering at Norwegian University of Science and Technology (NTNU). SIMLab and CASA works on developing tools and numerical methods for product development of structures and materials in partnership with Hydro Aluminium, Statoil, SINTEF, SSAB Swedish Steel, Benteler Aluminium Systems, BMW, Audi and Norwegian Defence Estates Agency (NDEA).

In this master thesis I have had the opportunity to both use a advanced numerical software and perform relevant laboratory experiments with great help from Trond Auestad. It has been both academically challenging and educational, but also a great experience to use the knowledge I have acquired during my time at NTNU on such an exciting field.

I would like to thank my supervisors Professor Magnus Langseth and PhD Marius Andersen for their guidance and engagement on this thesis. Additionally, I would like to thank Egil Fagerholt for his guidance and help with Digital Image Correlation (DIC), Professor Emeritus Per Kristian Larsen for academically inputs and Amund Døssland Helvik and Jostein Dale Arnesen for help with graphical design and grammar corrections.

Trondheim, 25.05.2016

Sigurd Guddal

Abstract

This master thesis has investigated the behaviour of aluminium cylinders subjected to compression for both unwelded and welded cross sections. Three different combinations of material and geometry has been tested in the laboratory, but also numerical analysis has been carried out by a numerical software, such as finite element programme. The aluminium alloys tested in this thesis are the heat treatable alloys 6060-T6 and 6082-T6.

Material tests, such as tensile tests have been performed to get accurate material models in the numerical study. These tensile tests were performed without significant problems, but a notable large scatter was found from alloy 6082-T6. Digital Image Correlation (DIC) was used to find the strains.

Only stub tests were performed in the laboratory due to unfinished design of the test rig used for long columns. The lengths performed were two and four times the diameter of the cylinders tested, and these tests were performed for both unwelded and welded cross sections. When welding was applied on the cylinders, only a surface weld was performed. The welds were welded symmetrical on two sides in the longitudinal axis at the mid-center of the cylinders with a length equal to the radius of the cylinders. Welded cross sections are of interest due to the significant lower material strength parameters in the vicinity of a weld. This area is called the heat affected zone (HAZ). The material parameters in the HAZ are found from previous studies, where hardness tests of the material were performed to find the yield and ultimate tensile strength.

The results from laboratory stub tests showed that unwelded cross sections localised the deformation symmetrical near one of the ends, but the welded cross sections triggered the cylinders to buckle at the mid-sections.

Analytical formulas for both shells independent of length, and long columns have been derived. Formulas for shell subjected to axial compression have been compared with laboratory experiments with a good degree of accuracy.

Numerical analysis have been able to recreate the deformation modes excelent for both unwelded and welded cross sections. The critical buckling stress and force-displacement curve is very accurate for alloy 6060-T6, but numerical results are a little conservative for alloy 6082-T6. This may be due to the large scatter from tensile test of 6082-T6. For welded cross sections, the critical buckling stress found from numerical analysis fits actually slightly better the laboratory results then what the results from unwelded cylinders do.

Much time is spent on measuring accurate geometry of the cylinders and the welds on every cylinders tested by use of a ultrasound device and a classical caliper. There were not much deviation in the measured geometry, so the mean values were used in the numerical analysis.

The laboratory results were compared with calculations from Eurocode 9: Design of Aluminium structures for both unwelded and welded cross sections and the results shows that the cylinders tested can resist up to twice the load calculated by EC9, depending on whether f_o is taken from EC9 or the tensile test performed in this study.

Samandrag

Denne masteroppgåva har sett på oppførselen til aluminiumsylindrar påført aksialt trykk for både usveiste og sveiste tverrsnitt. Tre ulike kombinasjonar av material og geometri har vorte testa i laboratoriet, men også numeriske analysar har vorte undersøkt med hjelp av eit numerisk dataprogram. I denne oppgåva er det nytta elementmetodeprogram og aluminiumslegeringane som er nytta er dei varmebehandla legeringane 6060-T6 og 6082-T6.

Strekktestar av materiala er utført for å få nøyaktige materialmodellar i dei numeriske analysane. Desse strekktestane vart utført utan problem, men resultata frå legering 6082-T6 var veldig sprikande. Digital Image Correlation (DIC) vart nytta for å finne tøyningane i strekktestane.

På grunn av at testriggen i laboratoriet ikkje var klargjort så vart det inga testing av lange søyler, kun korte sylindrar med lengde hhv. to og fire ganger diameteren til sylindrane for både usveiste og sveiste tverrsnitt. Sveiselarva vart lagt på overflata til sylindrane symmetrisk på to sider i lengdeaksen med senter i midten av lengda på sylindrane med ei lengde lik radiusen til sylindrane. Eit sveist tverrsnitt er interessant å utforske grunna droppet i materialstyrkjen kring sveisen som vert kalla varmtvirka sone (HAZ). Materialparametrane i HAZ er funne frå tidlegare studier der det er vorte tatt utgangspunkt i hardhetstestar.

Resultat frå laboratorietestar av korte sylindrar viser at usveise tverrsnitt lokaliserer deformasjonsmønsteret symmetrisk nær ein av endane, men sveiste tverrsnitt derimot får utløyst eit knekkmønster ved midten av sylindrane.

Analytiske formlar for både skal uavhengig av lengda, og lange søyler har vorte utleiia. Formlar for skal påført aksialt trykk er vorte samanlikna med resultat frå laboratorietestar med rimelig god nøyaktighet.

Dei numeriske analysane har klart å simulert eksakt deformationsmønster for både usveiste og sveiste tverrsnitt. Den kritiske knekkspenninga og kraft-forskuvningskurva er meget lik resultata frå laboratoriet for legering 6060-T6, men litt konservativ for legering 6082-T6. Dette skuldast mest sannsynleg den store spreiinga frå strekktestane av 6082-T6. For sveiste tverrsnitt så passar resultata frå numeriske analysar betre laboratorie resultata enn kva dei usveiste gjer.

For best mulig numeriske resultat så er det nytta mykje tid for nøyaktige målingar av geometrien til både sylindrane og sveisane ved bruk av vanleg skyvelær og eit ultralyd måleapparat. Det var veldig lite avvik frå målingane og gjennomsnittsverdiane er nytta.

Laboratorieresultata er samanlikna med utrekningar frå Eurokode 9: Prosjektering av aluminiumskonstruksjonar for både usveiste og sveiste tverrsnitt og resultata syner at sylindrane som er testa kan tole opp til det dobble av kva som er utrekna frå EC9, avhengig av om flytespenninga er tatt frå EC9 eller strekktestane utført i denne masteroppgåva.

Contents

Notation

Notations and symbols used in this report are defined in the text when they occur.

Symbol	Meaning
A	Area of a specimen
A_{curved}	Area of curved cross section in tensile test
A_{eff}	Effective cross section area
$A_{rectangular}$	Area of rectangular cross section in tensile test
A_{tot}	Totale area of cross section
A_w	Area of cross section applied to welding
A_0	Initial area of specimen
Al	Aluminium
C	Factor
$C_{circumference}$	Circumference around a cylinder
C_i	Hardening parameters for ith parameter in Voce rule
D	Diameter to mid-thickness of a cylinder
D_b	Bending rigidity
F	Force applied in tensile test
E	Young`s modulus
E_s	Secant modulus
E_t	Tangent modulus
HV	Vickers Hardness
I	Second moment of inertia
L	Length of specimen or cylinder
L_0	Initial length of specimen
ΔL	Incremental change in length of a specimen
L_w	Length of weld
M	Moment
M_a	Axial half-waves
M_{el}	Elastic moment
Mg	Magnesium
M_{Rk}	Characteristic moment resistance
M_z	Moment about z-axis
N	Applied load
$N_{b,Rd}$	Design value for flexural buckling
$N_{c,Rd}$	Design value for compression
N_{cr}	Critical buckling load
N_E	Euler buckling load
N_{el}	Elastic loading
N_{Rk}	Characteristic buckling resistance
N_x, N_{xy}, N_y	Axial, circumferential and shear loads applied to the cylinder

P	Applied load
Q	Net heat input from the current
Q_i	Hardening parameters for ith parameter in Voce rule
S	Strain energy stored in the cylinder
$S, mises$	Mises stress
Si	Silicon
T	Temperature
T_0	Initial temperature
W_{el}	Elastic modulus
W_z	Elastic modulus about z-axis
Y_0	Yield stress
Z_L	Factor
a	Cantilever distance for rig part
b_{haz}	Width of HAZ
d	Distance from column end to rotation center
e	Max deflection of a column
e_0	Initial imperfection of a column
f_o	Corresponding stress value for 0.2% permanent strain
$f_{o,haz}$	0.2% proof strength in HAZ
$f_{Tensile\ test}$	Stress from tensile test
f_u	Ultimate tensile strength
$f_{u,Vickers}$	Ultimate stress from Vickers Hardness test
$f_{Vickers\ test}$	Stress from Vickers Hardness test
$f_{0.2}$	Corresponding stress value for 0.2% permanent strain
$f_{0.2,Vickers}$	0.2% proof strength from Vickers Hardness test
$f_{0.1}$	Corresponding stress value for 0.1% permanent strain
f_{ε_o}	Corresponding stress value for 0.2% permanent strain
i	Area radius of gyration
k_c	Compressive buckling coefficient
m	Wavenumber in axial direction of a cylinder
m_{crown}, n_{crown}	Represents square deformation waves.
n	Wavenumber in circumferential direction of a cylinder
n_{RO}	Material parameter in Ramberg & Osgood materialmodel
n_e	Material parameter in Ramberg & Osgood for buckling
n_u	Material parameter in Ramberg & Osgood for ultimate capacity
p	Pressure applied to the cylinder
pc	Volume heat capacity
q	Unit line load from cylinder wall
r	Middle radius of a cylinder
r_{haz}	Radius prevalence of the heat affected zone
$\bar{r}$	Inner radius in rig part not subjected to bending
s	Unit strain energy
t	Thickness of cylinder wall
t_{cyl}	Thickness of cylinder wall
t_{eff}	Effective thickness due to cross section class 4
t_r	Thickness of rig part for 2nd choice of design
t_w	Time during welding
u, v, w	Longitudinal, circumferential and thickness displacement of a cylinder
u_{tot}	Total displacement of tensile test

u_1, u_2	Displacement of the specimen and test rig for a tensile test, respectively.
w_0	Initial displacement in thickness direction
$w_{,xx}$	Second derivative of deflection
$w_{,x}$	First derivative of deflection
α	Factor
β	Factor
β_n	Factor
ε	Strain
ε	$= \sqrt{250/f_o}$
ε_e	Engineering strain
ε_L	Logarithmic strain
ε_{Lu}	Ultimate logarithmic strain
ε_o	0.2% permanent strain
ε_u	Strain corresponding to ultimate strength
$\varepsilon_x, \varepsilon_y, \gamma_{xy}$	Strain in x and y direction and shear strain
$\varepsilon_{xx}, \varepsilon_{xy}, \varepsilon_{yx}, \varepsilon_{yy}$	Components in strain matrix
$\varepsilon_1, \varepsilon_2, \varepsilon_3$	Strain in longitudinal, circumferential and thickness directions
χ	Reduction factor for the relevant buckling mode
χ_1, χ_2, χ_3	Corresponding curvature in longitudinal, circumferential and thickness directions
ε^{el}	Elastic strain
ε^{pl}	Plastic strain
$\bar{\varepsilon}$	Accumulated plastic strain in Voce rule
$\overline{\varepsilon_L}$	Mean logarithmic strain
σ	Stress
σ_{cr}	Critical buckling stress
σ_e	Engineering stress
σ_t	True stress
$\sigma_x, \sigma_y, \tau_{xy}$	Stress in x and y direction and shear stress
σ_Y	Yield stress in Voce rule
σ_0	Yield stress
${\sigma_{cr}}^{el}$	Elastic critical buckling stress
κ	Factor to allow for weakening effects of welding
γ_{M1}	Partial factor for resistance of cross section
ψ	Relative tensile strength
ψ_u	Relative ultimate tensile strength
$\psi_{0.2}$	Relative 0.2% proof strength
$d\theta$	Unit distance around a cylinder
η	Factor
μ	Aspect ratio between deformation waves in longitudinal and circumferential axis
μ_f	Coulombs coefficient of friction
λ	Slenderness
λ_T	Thermal conductivity
λ_n	Half-wave length
$\bar{\lambda}$	Factor
υ	Poissons`ratio

υ_e	Elastic Poisson`s ratio
υ_p	Plastic Poisson`s ratio
ω	Factor
ρ	Relative buckling stress
ρ_c	Factor to factor down the thickness of a cylinder
$\rho_{o,haz}$	HAZ softening factor for the corresponding 0.2% permanent strain
Π_p	Total potential energy
U	Strain energy
Ω	Potential energy
λ_j	Eigenvalues
$\{\boldsymbol{D}\}$	Degree of freedom matrix
$[\boldsymbol{K}]_g$	Geometrical stiffness matrix
$[\boldsymbol{K}]_m$	Material stiffness matrix
$[\boldsymbol{K}]_t$	Resultant tangent matrix
$\{\boldsymbol{R}\}$	Force matrix
$\{\boldsymbol{\varphi}\}_j$	Eigenvectors
$\frac{\partial \mathrm{R}^{\mathrm{res}}}{\partial \lambda}$	Load vector for each time increment

Appendix A-G

C	Curvature on a parametric curve
R	Radius of curvature
$f(x)$	A general plane curve
n_{el}	Number of elements
t	Time
v	Length of velocity vector
κ	Curvature of a unit tangent vector
$\boldsymbol{a}$	Acceleration vector
$\widehat{\boldsymbol{N}}$	Unit normal vector
$\boldsymbol{r}$	Parametric curve
$\widehat{\boldsymbol{T}}$	Unit tangent vector
$\boldsymbol{v}$	Velocity vector
$[\boldsymbol{B}]$	Strain-displacement matrix
$[\boldsymbol{E}]$	Modulus matrix
$[\boldsymbol{G}]$	Strain-displacement matrix
$[K]_g$	Nodal geometric stiffness matrix
$[\boldsymbol{K}]_g$	System geometric stiffness matrix
$[K]_m$	Nodal material stiffness matrix
$[\boldsymbol{K}]_m$	System material stiffness matrix
$[\boldsymbol{L}]$	Connectivity matrix
$[\boldsymbol{N}]$	Shape functions
$[\boldsymbol{S}]$	9x9 stress matrix
$[\boldsymbol{\sigma}]$	3x3 stress matrix

Abbreviations

CASA	Center of Advanced Structural Analysis
DIC	Digital Image Correlation
DOF	Degree of Freedom
EC	Eurocode
FEA	Finite Element Analysis
FEM	Finite Element Method
FSW	Friction-Stir Welding
HAZ	Heat Affected Zone
MIG	Metal Inert Gas
NDEA	Norwegian Defence Estates Agency
TIG	Tungsten Inert Gas

1 Introduction

1.1 Background

Statnett is a national company that is responsible for the entire power grid in Norway. They are searching for more efficient ways to build power pylons, and the material choice is therefore of crucial importance. Aluminium alloys have many important properties which make them competitive with other metals, such as high corrosion resistance, low manufacturing costs and low self-weight. When designing power pylons, the absolute most important property is self-weight. Due to mountains and lack of available roads, many power pylons have to be flown to the construction site and a low self-weight is therefore favourable. If the pylons are heavy, they also require bigger foundations, and then again more helicopter trips.

Simple calculations based on Eurocode 9 (2007) indicates a total weight of 5500 kg for a power pylon made by aluminium compared to 9100 kg for one made by steel. Temporary calculations indicates that this weight reduction is not sufficient enough when it comes to costs. Statnett therefore wants research on optimum combinations between material and geometry by use of advanced numerical tools customized to be used for aluminium, so that the total weigth can be reduced even further.

Like other metals, aluminium alloys have the property to undergo large permanent (plastic) deformations so that any collaps of a pylon will give a warning, unlike glass or ceramic. This property is called ductility. When optimizing aluminium alloys, its known that no metals can be both ductile and have a high strength, and therefore a combination have to be chosen. When research of different alloys are performed, high strength is naturally favourable due to less material needed with a stronger material. But there need to be a balance so that large plastic deformations occur before failure and gives a collapse warning. Ductile behaviour reduces the need for calculations of stress and strain concentrations for statically loaded structural joints and connections because of the ability of the structure to redistribute forces and moments to be in accordance with the assumed static model, Matusiak (1999).

The design of the structural joints have a high influence on the cost effectiveness of the pylons. Today there are many different joining techniques available, but still welding is frequently used, and in some cases necessary. Traditional bolts are for example almost impossible to use when cylinders are connected, and welding is therefore required.

The so-called T6 heat-treatable aluminium alloys are made by a process that gives highest strength and are obtained from age-hardening Al-Mg-Si alloys. These alloys are often used in welded structures, and Statnett is also interested in these alloys. When age-hardened alloys are welded, many different changes in the microstructure take place simultaneously in the vicinity of a weld, and Al-Mg-Si alloys in T6 condition suffers from severe softening in the heat-affected zone (HAZ) due to reversion of Mg_2Si precipitation during the weld thermal cycle.

Precipitation hardening is a method to decide the strength of a heat-treatable aluminium alloy, Altenpohl (1982).

1.2 Objectives and Scope

The objective of the present study is to investigate how aluminium behave when compression is performed by means of laboratory experiments and numerical analysis. This study will only investigate cylinders for two different aluminium alloys, 6060-T6 and 6082-T6. The study will investigate three different combinations of material and geometry. The two different geometries that will be subjected to axial loading have r/t-ratio equal to 10.4 and 35.3, corresponding to D=100 mm, t=4.8 mm and D=127 mm, t=1.8 mm, respectively. One important objective will therefore be to establish how conservative the regulations in Eurocode 9 (2007) actually are so that buckling of aluminium cylinders can be designed more correctly and aluminium structures can be better utilized. To ensure local buckling of the cylinders, stub tests of short cylinders will be performed with lengths equal to two and four times the diameter, both experimentally and numerically. Longer cylinders that buckles globally will not be investigated by laboratory experiments, but some numerical analysis and analytical equations will be derived. The reason why laboratory experiments of long cylinders are not performed, is because the testing rig in the laboratory was not finished during this master thesis. So this part is left for further work. A another objective is to investigate how aluminium cylinders will behave in compression when they are welded. The cylinders will be welded with two symmetrical welds on both sides, positioned at the center of the cylinder, and the length of the welds will be half of the cylinders diameter.

1.3 Previous Studies

Some information are available in the literatures on structural behaviour of aluminium, but very little considering welds and there are absolutely no available information regarding buckling of welded aluminium cylinders.

Hopperstad, Langseth and Hanssen (1997) performed tensile tests for unwelded aluminium alloy 6082-T6 and fitted it to the five parameter Voce model and performed laboratory buckling tests of cruciforms for different b/t ratios, and compared with numerical analysis.

Hopperstad, Langseth and Hanssen (2000) carried out an extensive experimental study for aluminium alloy 6060-T6 for unwelded cylinders subjected to axial loading. In the study, the r/t ratio varried in the range 17-28, and the deformation modes were non-axisymmetric/ diamond form.

Ting Wang (2006) have performed a large study based on Matusiak (1999), on behaviour of welded 6082-T6 alloy for tensile tests and beam bending. The study gives correct material properties in the HAZ, based on tensile tests cutted out from the vicinity of a butt weld of a plate.

A. Alisibramulisi, O.R. Myhr, O.G. Lademo, P.K. Larsen (2010) studied the material parameters in the HAZ for aluminium alloy 6060-T6 and found a relation between Vickers hardness and yield stress for natural ageing.

1.4 Approach for the Study

Axial compression of aluminium will be investigated to establish their exact behaviour and load resistance. For short cylinders (stub tests) analytical calculations, numerical analysis, laboratory experiments and calculations from Eurocode 9 will be applied and compared together for both welded and unwelded cross sections. For longer cylinders, only some numerical analysis by the finite element software, Abaqus will be applied to validate the chosen design decided to build in the laboratory. Analytical formulas will also be derived for long aluminium columns. Comparing laboratory results with numerical analysis for long columns will be suggested in further work.

The correct stress strain relation will be found from tensile tests conducted from the same cylinders as the ones tested in the laboratory, where strains will be found from Digital Image Correlation (DIC).

2 Theory

2.1 Buckling Theory

Buckling is a physical phenomena that happens due to compression forces, where small changes in the longitudinall axis causes huge sudden deflections in the transversal axis. All cross sections, and particular thin-walled cylinders have a membran-strain energy which will be transversed into bending-strain energy, and compression and tension will occur on opposite sides (Deeks & Hao, 2005). When a column buckles out in the middle, its called global buckling. This happens when the longitudinal axis differs from its initial state (Figure 2.1a). Local buckling is a complex phenomena, but basically it happens when the deformation form has its longitudinal axis constant during failure (Figure 2.1b). Local buckling happens because the load required to buckle out the entire member for short cylinder is larger than the load required to buckle the thin-wall members locally.

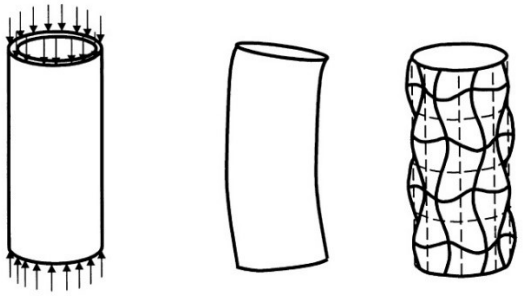

a) b)

Figure 2.1 – Buckling mode for a) global and b) local buckling.

For a compression loaded member the total potential energy from the system is given as

$$\Pi_p = U + \Omega = \frac{1}{2}\{\boldsymbol{D}\}^T\left([\boldsymbol{K}]_m + [\boldsymbol{K}]_g\right)\{\boldsymbol{D}\} - \{\boldsymbol{D}\}^T\{\boldsymbol{R}\} \qquad [2.1]$$

where $[\mathbf{K}]_\mathrm{m}$ is the material stiffness matrix, $[\mathbf{K}]_\mathrm{g}$ is the geometrical stiffness matrix (Appendix B), $\{\boldsymbol{R}\}$ is the load matrix, $\{\boldsymbol{D}\}$ is the degrees of freedom matrix and U and Ω are the strain and potential energy, respectively. Buckling occurs when the resultant tangent stiffness matrix, $[\boldsymbol{K}]_t$ goes towards zero

$$[\boldsymbol{K}]_t = [\boldsymbol{K}]_m + [\boldsymbol{K}]_g \rightarrow [\mathbf{0}] \qquad [2.2]$$

For solving [2.2] the determinant of the equation is obtained to find the singularity, by either displacement controll or load controll. The difference is that load controll fails at point A in figure 2.2, but displacement controll fails at point B. In a buckling analysis of a column its not

of interest to go further than point A, since the structure has failed when point A is reached. Anyhow, displacement controll is used to obtain the buckling load, both analytical and numerically, because its more reliable and robust around point A.

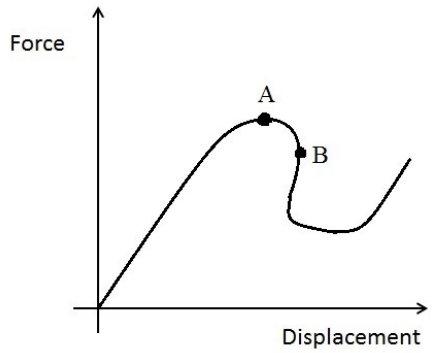

Figure 2.2 – Force vs displacement for a buckling phenomena.

Equation [2.2] then becomes a eigenvalue problem

$$\left([\boldsymbol{K}]_m + \lambda_j [\boldsymbol{K}]_g\right)\{\boldsymbol{\varphi}\}_j = \{\mathbf{0}\} \qquad [2.3]$$

where λ_j is the eigenvalues, $\{\boldsymbol{\varphi}\}_j$ is the eigenvector, $P_j = \lambda_j P$ and P is the load applied.

Equation [2.3] gives a set of eigenvectors. The critical buckling load is found at point A for a column in compression, and here the tangent is horizontal. This is therefore a limiting point (the load can not go above this value). For a limit point the following relation yields

$$\{\varphi\}^T \frac{\partial R^{res}}{\partial \lambda} \neq 0 \qquad [2.4]$$

where $\frac{\partial \mathrm{R}^{\mathrm{res}}}{\partial \lambda}$ is the loadvector for each time increment.

2.2 Material Theory

2.2.1 Ramberg & Osgood material model

In the 40's there were several experiments going on for different aluminium alloys, and the conventional description of the stress-strain curve of metals by only the Young's Modulus and the yield strength were not good enough for aluminium. By looking at the test stress-strain curve it looked like at least one additional parameter should be introduced. A generalised constitutive law $\varepsilon = \varepsilon(\sigma)$ for aluminium alloys were proposed by Ramberg & Osgood (1943)

$$\varepsilon = \frac{\sigma}{E} + \varepsilon_0 \left(\frac{\sigma}{f_{\varepsilon_0}}\right)^{n_{RO}} \quad [2.5]$$

where normally $\varepsilon_o = 0.002$ and the corresponding $f_{\varepsilon_o} = f_{0.2}$. Aluminium does not have a clear yielding point, so from experiments its a good representation to take the stress value that gives 0.2% permanent strain. The n_{RO}-value is a material parameter. Today its taken from curve-fitting by numerical tools, but some analytical expressions are also valid. Since its almost impossible to fit a experimental curve entirely, two expressions for n_{RO} are given (Matusiak, 1999).

When buckling is of interest, a classical formulation yields

$$n_{RO} = n_e = \frac{\ln 2}{\ln\left(\frac{f_{0.2}}{f_{0.1}}\right)} \quad [2.6]$$

When the ultimate capacity of the cross section is of interest, a general formlation yields

$$n_{RO} = n_u = \frac{\ln\left[500\left(\varepsilon_u - \frac{f_u}{E}\right)\right]}{\ln\left(\frac{f_u}{f_{0.2}}\right)} \quad [2.7]$$

where f_u is the ultimate strength and ε_u is the uniform elongation corresponding to the ultimate strength.

Tangent E-module

The E-module is constant during the elastic domain, but in the plastic domain its changing. By differentiate [2.5] with respect to the stress, an expression for the tangent E-module at a given point in the plastic domain can be obtained

$$\frac{d\varepsilon}{d\sigma} = \frac{1}{E} + \varepsilon_o n_{RO} \left(\frac{\sigma}{f_{\varepsilon_o}}\right)^{n_{RO}-1} \frac{1}{f_{\varepsilon_o}} \quad [2.8]$$

$$E_t = \frac{d\sigma}{d\varepsilon} = \frac{E}{1 + \frac{\varepsilon_o n_{RO} E}{f_{\varepsilon_0}} \left(\frac{\sigma}{f_{\varepsilon_0}}\right)^{n_{RO}-1}} \quad [2.9]$$

If the tangent modulus is used in Eulers formula for column buckling, the critical buckling load is a function of the parameter n_{RO}, which represents the hardening of the material.

2.2.2 Tensile test of aluminium

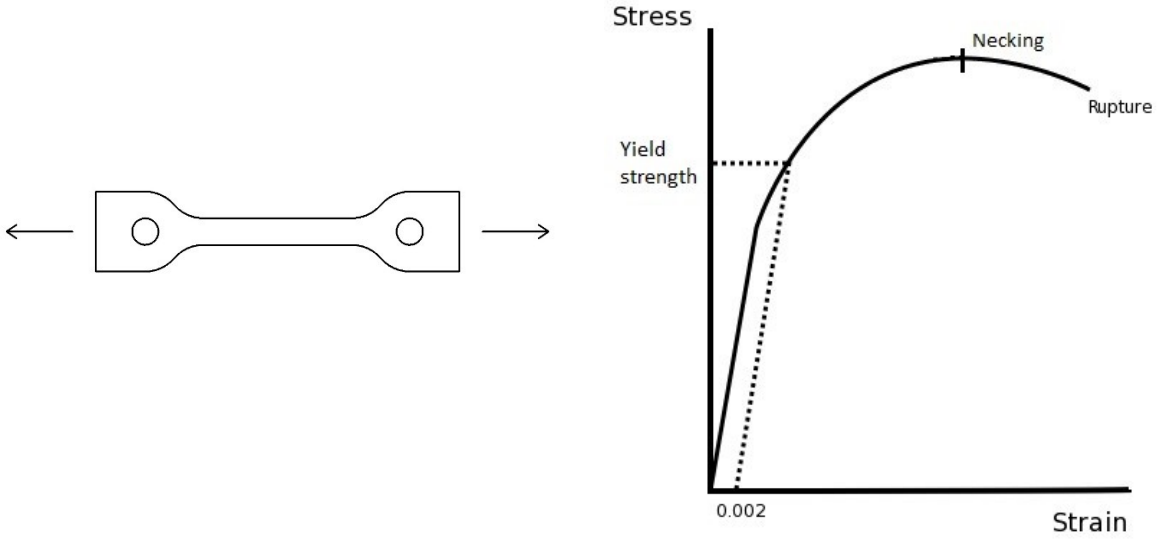

a) b)

Figure 2.3 – a) Specimen of a tensile test with the corresponding b) stress strain curve.

The engineering strain is given as the relative elongation of a material, hence

$$\varepsilon_e = \int_{L_0}^{L} \frac{dL}{L_0} = \frac{\Delta L}{L_0} = \frac{L - L_0}{L_0} = \frac{L}{L_0} - 1 \qquad [2.10a]$$

$$\frac{L}{L_0} = 1 + \varepsilon_e \qquad [2.10b]$$

The logaritmic strain is given as

$$\varepsilon_L = \int_{L_0}^{L} \frac{dL}{L} = \ln\left(\frac{L}{L_0}\right) = \ln(1 + \varepsilon_e) \qquad [2.11]$$

The assumption of constant volume is used

$$A_0 L_0 = AL \qquad [2.12]$$

$$A = A_0 \frac{L_0}{L} = A_0 \frac{1}{1 + \varepsilon_e} \qquad [2.13]$$

$$A = A_0 \frac{1}{\exp(\varepsilon_L)} \qquad [2.14]$$

Equation [2.14] can be used to establish the relation between the engineering stress and true stress. The true stress is found from updating the area for all values of strain

$$\sigma_t = \frac{F}{A} = \frac{\exp(\varepsilon_L)\, F}{A_0} = \sigma_e \exp(\varepsilon_L) \quad [2.15]$$

From a elastic-plastic materialmodel the constitutive equation for strain is given as

$$\varepsilon = \varepsilon^{el} + \varepsilon^{pl} \quad [2.16]$$

and the plastic strain is then found by using the constitutive equation $\varepsilon^{el} = \sigma/E$

$$\varepsilon^{pl} = \varepsilon - \frac{\sigma}{E} \quad [2.17]$$

The diffuse necking point can be derived from equation [2.15] by establishing the engineering stress

$$\sigma_e = \sigma_t \exp(-\varepsilon_L) \quad [2.18]$$

Necking is found when the stress reaches its maximum, or when the incremental change in engineering stress is zero. The product rule gives

$$d\sigma_e = d\sigma_t \exp(-\varepsilon_L) - \sigma_t \exp(-\varepsilon_L)\, d\varepsilon_L = 0 \quad [2.19]$$

$$= (d\sigma_t - \sigma_t d\varepsilon_L) \exp(-\varepsilon_L) = 0 \quad [2.20]$$

$$\frac{d\sigma_t}{d\varepsilon_L} = \sigma_t \quad [2.21]$$

Equation [2.21] is known as the Considére`s criterion and is illustrated in figure 2.4.

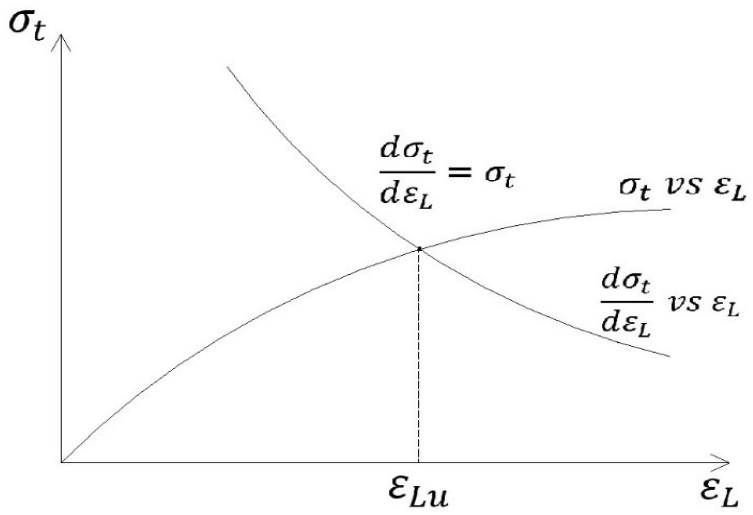

Figure 2.4 - Considére`s criterion for finding the necking point.

2.2.3 The five parameter extended Voce rule

Its convenient to represent the stress strain curve by a mathematical expression. So based on previous studies on aluminium alloys, the five parameter extended Voce rule is frequently used to fit the stress vs plastic strain curve, hence

$$\sigma_Y(\bar{\varepsilon}) = Y_0 + Q_1(1 - \exp(-C_1\bar{\varepsilon})) + Q_2(1 - \exp(-C_2\bar{\varepsilon})) \qquad [2.22]$$

where Y_0 is the yield stress, C_i and Q_i are hardening parameters and $\bar{\varepsilon}$ is the accumulated plastic strain.

2.2.4 Baushinger effect

Since all the material tests are performed in tension, and buckling is a compression situation, there might be some problems related to this when it comes to the material behaviour. When a material with isotropic hardening is loaded and reloaded it will not always behave equal in tension and compression, this is called the Bauschinger effect. The greater the tensile cold working, the lower the compressive yield strength. This is illustrated in figure 2.5.

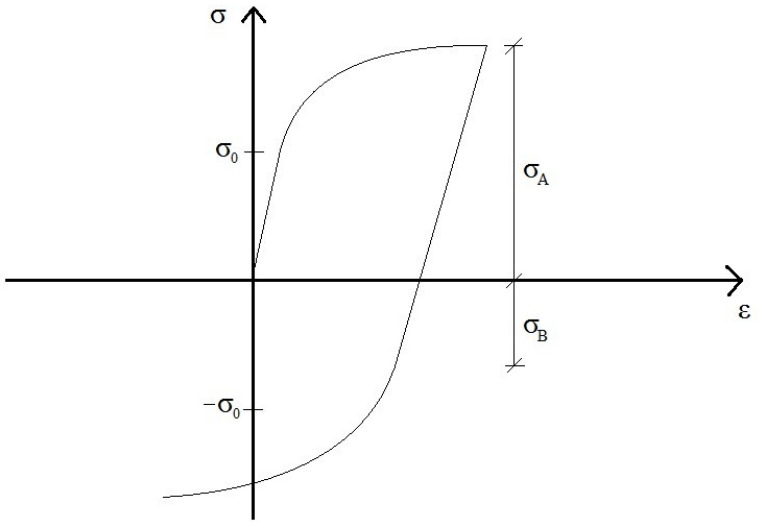

Figure 2.5 – Baushinger effect for isotropic hardening.

$|\sigma_A| > \sigma_0$ and $|\sigma_B| < |\sigma_A|$. When σ_A increases, σ_B decreases and will sometimes become $|\sigma_B| < \sigma_0$.

Therefore, compression tests should be perform to get an idea of how large this deviation is, but due to time limitation laboratory compression tests are not performed in this study. It is, however suggested in further work.

2.3 Welding Theory

2.3.1 Introduction

This is not a study for deep understanding of welding, but some knowledge should be established to be able to make sufficient assumptions and conclusions when performing tests and processing data. Welding is a tool for gluing components together. Welding is a expression that usually is used when combining metals, but it can also be used when combining polymeres and some other materials. Traditionally welding means that electricity is used to melt materials together by making a tiny space between the material and the weld-pin. This makes an electric arc between an electrode (weld pin) and the base material. Welding of regular structural steel is a easy and widespread method, and does not effect the strength of the steel in a appreciable way. Welding aluminium on the other hand, is a very complex metallurgical process that reduces the strength of the material severely. The weld itself does usually have a higher yielding point than its base material, and its designed to not be the weakest link in a joint, for several reasons such as sudden and brittle collaps. From the welding process, TIG, MIG, FSW, or other arc welding methods, there will always be a appreciable amount of heat at the weld tip, and locally around the weld it will be high temperature gradients and rapid temperature fluctuations as well (Grong, 1997). Because of this high temperature, the microstructure in aluminium changes and as a function of temperature, metall, thickness and method, there will be a zone where the material strength is reduced. This zone is called heat affected zone, or HAZ. In this zone, the material parameters changes, usually to weaken the material. For some cases the yielding point can be decreased by 50% just around the weld, and then following a typical curve as shown in figure 2.6, where hardness is linear related to the yield and ultimate strength.

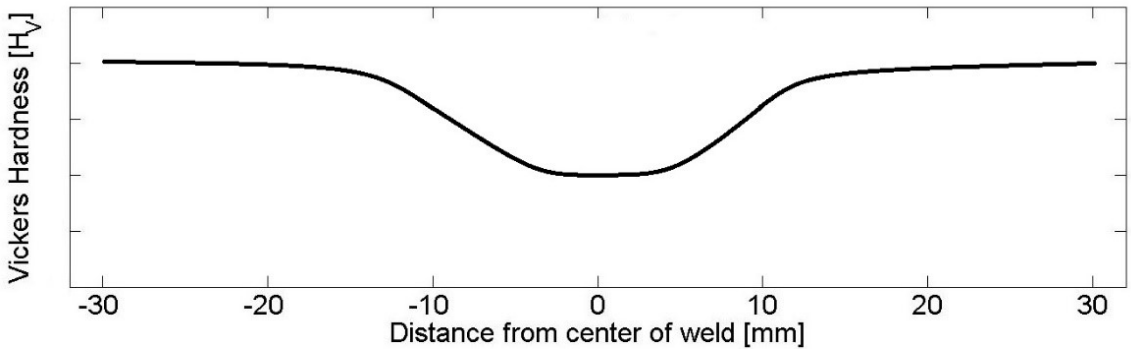

Figure 2.6 – Vickers hardness in the vicinity of a weld center.

Since welding requires a high amount of heat, its reasonable to neglect all other sources for temperature so that the general fundamental differential equations for heat conduction in solids are valid and can be written for uniaxial heat conduction as

$$\frac{\partial T}{\partial t} = \frac{\lambda_T}{pc}\frac{\partial^2 T}{\partial x^2} \qquad [2.23]$$

and for triaxial heat conduction as

$$\frac{\partial T}{\partial t} = \frac{\lambda_T}{pc}\left(\frac{\partial^2 T}{\partial x^2} + \frac{\partial^2 T}{\partial y^2} + \frac{\partial^2 T}{\partial z^2}\right) \quad [2.24]$$

where T is the temperature, t_w is the time, x is the heat flow direction, λ_T is the thermal conductivity and pc is the volume heat capacity. If arc welding is applied at a surface on a isotropic metall, such as aluminium, the heat will flow in a isoterm way into the base material, as shown in figure 2.7.

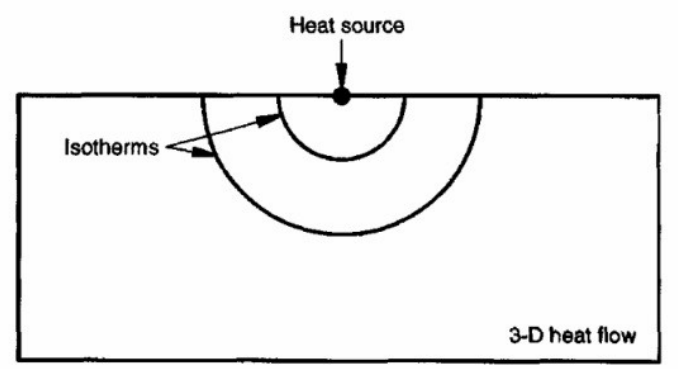

Figure 2.7 – Heat spreading in a isotropic material.

Further, its assumed that the heat is applied instantaneous at time $t_w = 0$, and equation [2.24] can be solved (Grong, 1997)

for a long cylinder with weld around the whole cross section

$$T - T_0 = \frac{\frac{Q}{A_w}}{pc\sqrt{4\pi\frac{\lambda_T}{pc}t_w}}\exp\left(-\frac{x^2}{4\frac{\lambda_T}{pc}t_w}\right) \quad [2.25]$$

or a line weld on a surface

$$T - T_0 = \frac{\frac{Q}{t_{cyl}}}{4\pi\lambda_T t_w}\exp\left(-\frac{{r_{haz}}^2}{4\frac{\lambda_T}{pc}t_w}\right) \quad [2.26]$$

where T_0 is the initial temperature, Q is the net heat input from the current, A_w is the cross section area, t_{cyl} is the thickness of the cylinder and ${r_{haz}}^2 = x^2 + y^2$, which represents the radius prevalence of the heat affected zone. This is an analytical method, and if dimensionless parameters are introduced and its solved numerically, it will be impossible to find data for very small values of time, since its based on instantaneous applied heat at $t_w = 0$. Anyhow, it can be used to get an idea of how large the heat affected zone will be, but it can not determine material parameters, such as yield and ultimate tensile strength. To establish these data, which are important for the numerical analysis of compressed cylinders, some other methods will be

considered, such as hardness methods. Standard tensile tests are different to perform for a material with HAZ, because it would fail for the weakest point, and therefore not consider the variating material properties throughout the zone. A way to performe tensile tests for material with HAZ is to cut out small pieces from different places in the HAZ, but hardness tests are easier and cheaper because it just presses a hard indenter into a flat surface of the test material, without destroing the specimen. To get reliable testresults, a material much harder than the test material is used, i.e. diamond or sapphire. These have also low coefficient of friction against other metals. Some tests uses a sphere, others a cone for the indenter. Its also possible to perform nanoindentation tests of high accuracy, but this will not be done in this master thesis, as the traditionall hardness tests gives sufficient results.

2.3.2 Vickers hardness test

The Vickers Hardness test presses a square diamond pyramide into the test material and gives the hardness in form of load/area.

For aluminium alloy 6082-T6, Hydro Aluminium and EC9 report the yield and ultimate stress as 260 MPa and 310 MPa, respectively. Matusiak (1999) proposed a linear relation between the hardness and the strength for butt welds, on the basis of Vickers hardness and uniaxial tensile tests, which yields

$$f_{0.2}(MPa) = 3.6HV - 81 \quad [2.27a]$$

$$f_u(MPa) = 2.6HV + 54 \quad [2.27b]$$

where HV is the Vickers hardness and $f_{0.2}$ and f_u are the yield and ultimate stress, respectively. This formula gives only two points on the stress strain curve, but Wang (2006) has used experimental tensile test data from Matusiak (1999) and established the hardening parameters for both butt and fillet welds for aluminium alloy 6082-T6. These results are given in section 5.3 and will be used for the numerical studie.

3 Analytical Formulas

3.1 Donnels Equation for Elastic Buckling of Thin-Wall Cylinders

The relation between the displacement and the middle-surface strain variations, and the curvature are given as:

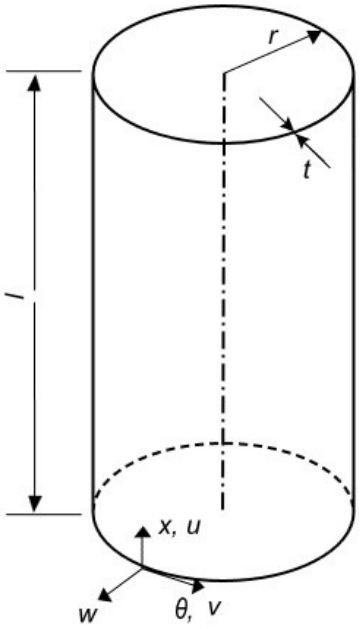

$$\epsilon_1 = \frac{\partial u}{\partial x}$$

$$\epsilon_2 = \frac{1}{r}\frac{\partial v}{\partial \theta} + \frac{w}{r}$$

$$\epsilon_3 = \frac{1}{2}\left(\frac{\partial u}{r\partial \theta} + \frac{\partial v}{\partial x}\right)$$

$$\chi_1 = \frac{\partial^2 w}{\partial x^2} \qquad [3.1]$$

$$\chi_2 = \frac{\partial^2 w}{r^2 \partial \theta^2}$$

$$\chi_3 = \frac{\partial^2 w}{r\partial x \partial \theta}$$

Figure 3.1 – Thin-wall cylinder.

By inserting equations [3.1] into the equilibrium equations for compression load

$$\sum F_x = 0, \quad \sum F_\theta = 0, \quad \sum F_w = 0 \qquad [3.2]$$

and using deformation plasticity theory, a set of equilibrium equations can be established for plastic buckling of thin-wall cylinders to be used to derive Donnell`s eight-order equation for elastic buckling (Gerard, NACA 3783). Here showed for radial displacement

$$D_b \nabla^8 w + \frac{Et}{r^2}\frac{\partial^4 w}{\partial w^4} + \nabla^4\left(N_x \frac{\partial^2 w}{\partial x^2} + 2N_{xy}\frac{\partial^2 w}{r\partial x \partial \theta} + N_y \frac{\partial^2 w}{r^2 \partial \theta^2} + p\right) = 0 \qquad [3.3]$$

where D_b is the bending rigidity equal to $Et^3/12(1-{v_e}^2)$, p is the pressure applied and N_x, N_{xy} and N_y are the axial, circumferential and shear loads applied to the cylinder, respectively.

By inserting boundary conditions into these equations, very different solutions will occur depending on how long the cylinders are, because the effect from fixed conditions will disappear when the cylinders are long. On the other hand, short cylinders will depend on how the boundaries are designed. When a simple supported cylinder in compression is considered, the edges correspondes to $w = 0$, $v = 0$ and $u \neq 0$, and a double sine-series which satisfies the boundary conditions is proposed as a solution to Donnell`s differential equation (Batdorf, NACA 1341)

$$\mathrm{w} = \mathrm{w}_0 \sin\frac{\pi \mathrm{y}}{\lambda_n} \sin\frac{\mathrm{m}\pi \mathrm{x}}{\mathrm{L}} \qquad [3.4]$$

$\lambda_n = \pi r/n$ is the half-wave length in the circumferential direction, θ and m is the axial wavenumber. Solving equation [3.3] with equation [3.4] and the fact that $N_y = N_{xy} = 0$, the compressive buckling coeffisient, k_c and the critical buckling stress, σ_{cr} yields

$$k_C = \frac{(m^2 + {\beta_n}^2)^2}{m^2} + \frac{12{Z_L}^2 m^2}{\pi^4 (m^2 + {\beta_n}^2)^2} \qquad [3.5]$$

where

$$\beta_n = \frac{L}{\lambda_n}$$

$$Z_L = \frac{L^2}{rt}\sqrt{1 - {\upsilon_e}^2}$$

υ_e is the elastic Poisson`s ratio.

$$\sigma^{el}{}_{cr} = \frac{k_C \pi^2 E}{12(1 - {\upsilon_e}^2)}\left(\frac{t}{L}\right)^2 \qquad [3.6]$$

where E is the Young`s modulus. For the two cylinder geometries in this study, A and B with geometries D=127 mm, t=1.8 mm and D=100 mm, t=4.8 mm, respectively, a plot of Z_L is shown for different lengths:

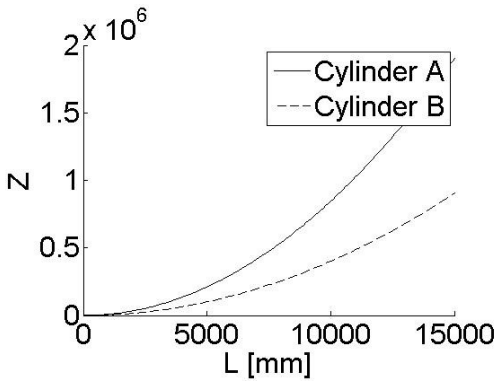

Figure 3.2 - Z_L vs length for cylinder D=127 mm and D=100 mm.

To calculate the critical value of k_c, the lowest value has to be identified, and is found from minimization of equation [3.5] to be for long cylinders

$$k_C = \frac{4\sqrt{3}}{\pi^2} Z_L = 0.702 Z_L \quad [3.7]$$

Equation [3.5] is differentiated with respect to $(m^2 + {\beta_n}^2)^2/m^2$ and set equal to zero. Thus

$$\frac{(m^2 + {\beta_n}^2)^2}{m^2} = \sqrt{\frac{12{Z_L}^2}{\pi^4}} \quad [3.8]$$

and by solving for β_n

$$\beta_n = \sqrt{\left(\frac{12{Z_L}^2}{\pi^4}\right)^{\frac{1}{4}} m - m^2} \quad [3.9]$$

A real (positive) value of m and n have to be contented, therefore the lowest value is $m = 1$ and $n = 0$. Hence,

$$Z_L \geq \frac{\pi^2}{\sqrt{12}} = 2.85 \quad [3.10]$$

Cylinder A and B, diameter 127 mm and 100 mm, respectively, will therefore have a limit equal to $L^A \geq 18.35$ mm and $L^B \geq 26.12$ mm. For cylinders shorter than these values, k_c can be found from substituting the limiting values $\beta_n = 0$ $(n = 0)$ and $m = 1$ into equation [3.5]

$$k_C = 1 + \frac{12{Z_L}^2}{\pi^4} = 1 + 0.1232{Z_L}^2 \quad [3.11]$$

Below are the k_c-values plotted against the length of the cylinder

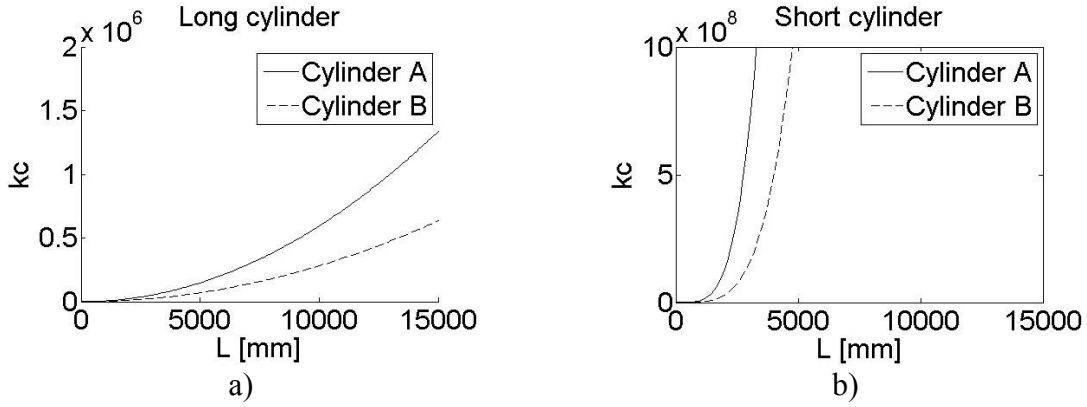

Figure 3.3 - k_c vs length of cylinder A (D=127 mm) and B (D=100 mm) for a) long cylinders and b) short cylinders when $Z_L \leq 2.85$.

Its observed that k_c is 1 when $L = 0$ for short cylinders, and that it increases rapidly when L increases. For a long cylinder, equation [3.7] is substituted into equation [3.6] with $\upsilon_e = 0.3$ and matches the classical buckling stress for an axially compressed thin-wall cylinder

$$\sigma^{el}{}_{cr} = \frac{0.702\frac{L^2}{rt}\sqrt{1-\upsilon_e{}^2}\pi^2 E}{12(1-\upsilon_e{}^2)}\left(\frac{t}{L}\right)^2 = \frac{0.57737}{\sqrt{1-\upsilon_e{}^2}}\frac{Et}{r} = 0.606\frac{Et}{r} \qquad [3.12]$$

Equation [3.12] is derived for shells with small values of t/r and no imperfections, so to use this formula on the cylinders in this study will be very unconservative, as shown in figure 3.4. The stress is plotted against the length of the cylinder on cylinder A (D=127 mm) and B (D=100 mm), and also on two thin-wall cylinders with small values of t/r.

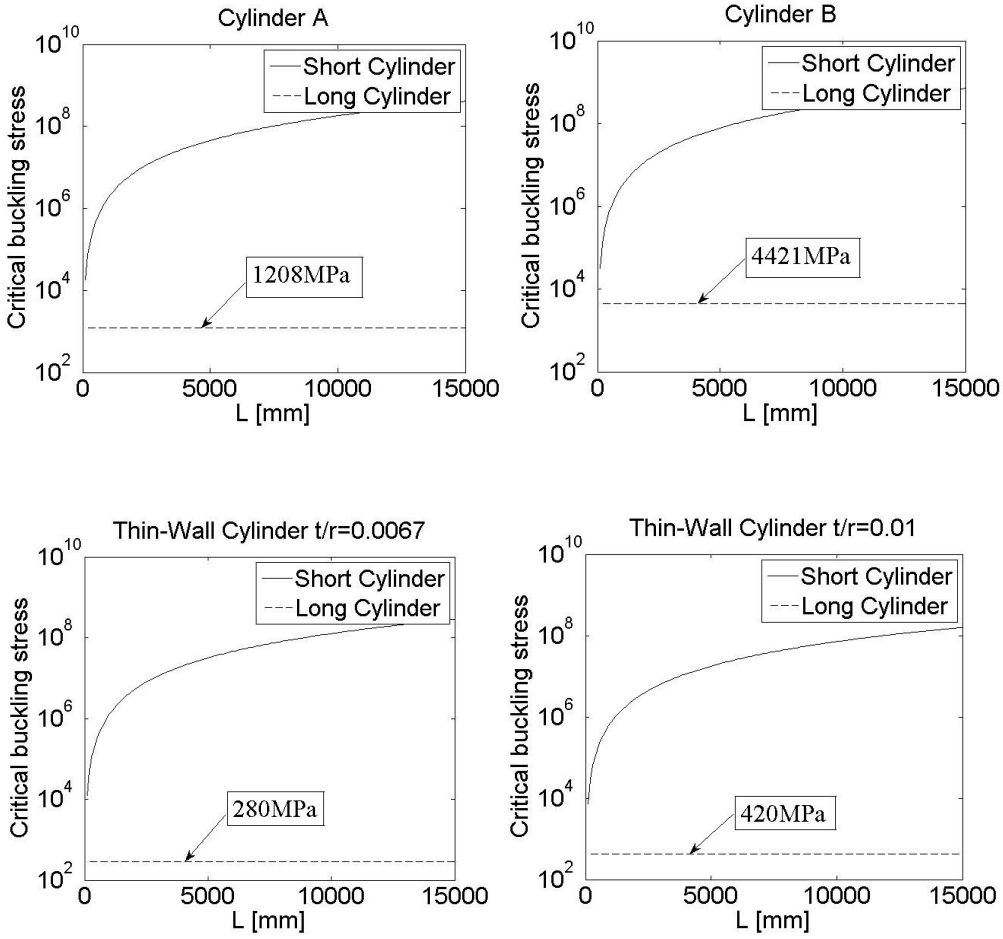

Figure 3.4 – Critical buckling stress calculated with equations for short and long cylinders for different geometry.

Its observed that the values of critical buckling stress increases rapidly for the theory for short cylinders, therefore it can be concluded that the theory is only valid when the cylinders are very short. The elastic buckling stress calculated for long cylinders from equation [3.12] gives very high stresses as shown in figure 3.4 and its clearly that plasticity needs to be involved. This is derived in section 3.3.

3.2 Strain Energy Equation

When a cylinder is loaded in axial compression up to the buckling load, the strain energy stored in the cylinder is equal to the external work done by the force, thus

$$S(\epsilon_1) = \int_0^{\epsilon_1} P\epsilon \, d\epsilon \qquad [3.13]$$

where ε_1 is the strain in the longitudinal axis of the cylinder because of the deformation from the load. When the strain energy is calculated, a relation between several parameters are derived to find the critical buckling stress (Tsien, 1942):

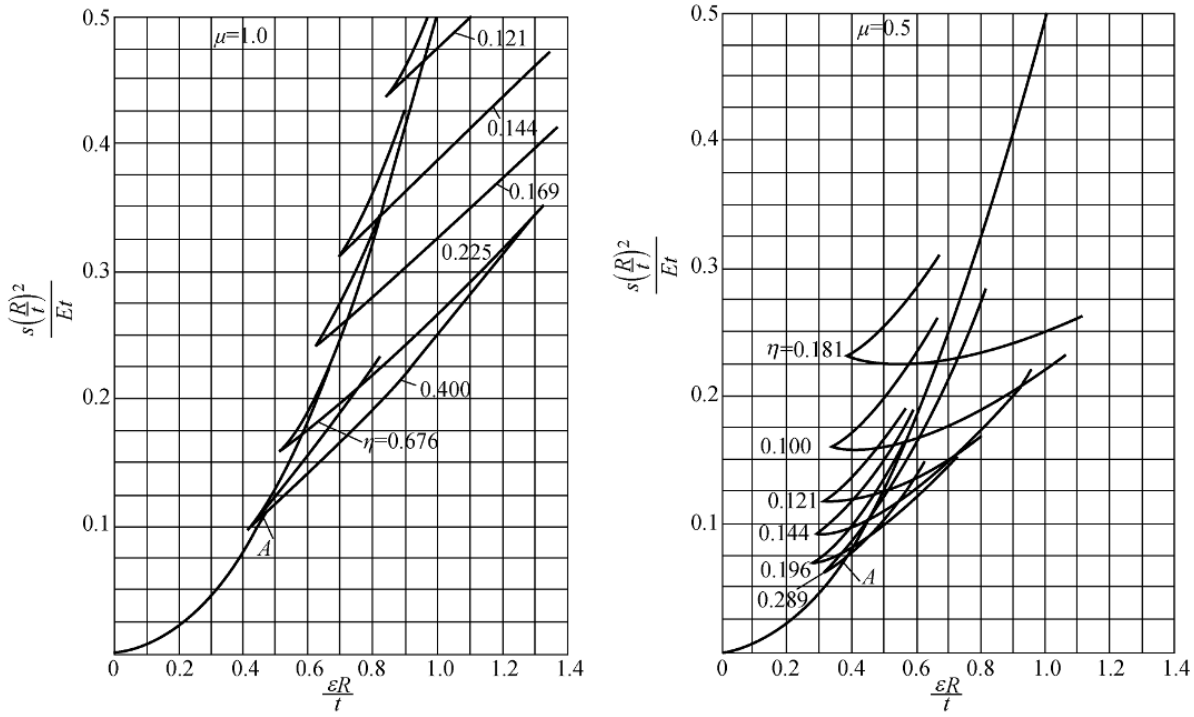

a) b)

Figure 3.5 – Relation between the unit strain energy s and the unit end shortening ε for cylindric shells under axial compression with the aspect ratio μ of the waves equal to a) 1.0 and b) 0.5.

The different parameters are the radius of the cylinder, r, the thickness, t, Youngs-modulus, E, the aspect ratio between waves in x and θ direction, $\mu = m/n$ and the parameter $\eta = n^2 t/r$. n is as known the wave number in circumferential direction. From figure 3.5a and 3.5b the critical buckling stress is found when the strain energy curve for a certain value of η crosses the unbuckled equilibrium curve. For example, $\mu = 1$ and $\eta = 0.4$ correspondes to point A in figure 3.5a where $\varepsilon r/t = 0.46$.

$$\frac{\varepsilon r}{t} = \frac{\sigma^{el}{}_{cr} r}{Et} = 0.46 \qquad [3.14]$$

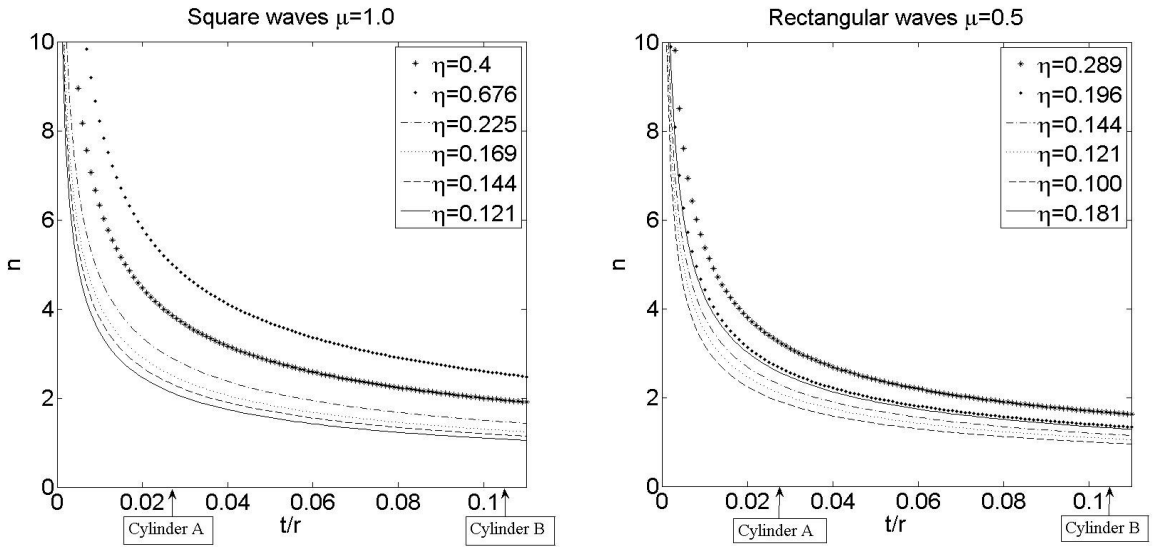

a) b)

Figure 3.6 – The relation between t/r and n for μ equal to a) 1.0 and b) 0.5.

By introducing a factor C into the equation $\sigma^{el}{}_{cr} = CEt/r$, the critical buckling stress versus t/r can be computed for values from figure 3.5.

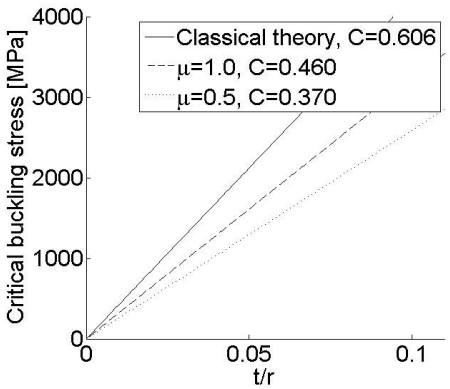

Figure 3.7 – Critical elastic buckling stress for different C values.

3.3 Plastic Buckling of Axially Compressed Shell with Membrane Prebuckling Deformations

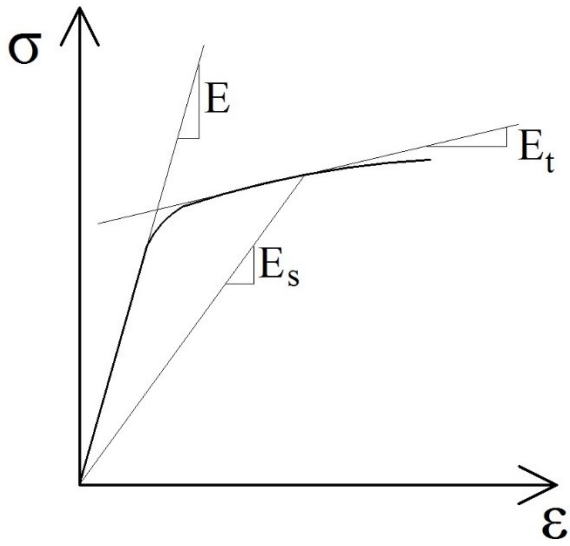

Figure 3.8 – Secant and tangent modulus.

The critical elastic buckling stress is shown in section 3.2 and its clearly that plasticity needs to be taken into account due to very high critical buckling stress. When deformation theory of plasticity is assumed ($\upsilon_p = 0.5$) the following relations between stress and strain yields

$$\sigma_x = \frac{4}{3}E_s\left(\varepsilon_x + \frac{1}{2}\varepsilon_y\right) \quad [3.15]$$

$$\sigma_y = \frac{4}{3}E_s\left(\varepsilon_y + \frac{1}{2}\varepsilon_x\right) \quad [3.16]$$

$$\tau_{xy} = \frac{1}{3}E_s\gamma_{xy} \quad [3.17]$$

where E_s and E_t is the secant and tangent modulus for the stress vs plastic strain relation for the material. The tangent modulus, E_t could be found by equation [2.9], but its taken more accurate from iteration from the tensile tests performed in section 5. From Langseth (2016) axisymmetric buckling is assumed and the following critical plastic stress is derived

$$\sigma^{pl}{}_{cr} = \frac{2}{3}E_s\frac{t}{r}\sqrt{\frac{E_t}{E_s}} \quad [3.18]$$

By using the relation

$$\upsilon = 0.5 - \frac{E_s}{E}(0.5 - \upsilon_e) \quad [3.19]$$

and the elastic critical buckling stress given in equation [3.12], an equation for the critical buckling stress yields

$$\sigma_{cr} = \sqrt{3\sqrt{1-\upsilon^2}E_s}\frac{t}{r}\sqrt{\frac{E_t}{E_s}} \qquad [3.20]$$

This formula uses the secant and tangent modulus for a given point on the stress vs plastic strain curve for a material to calculate the critical buckling stress. The intersection point between equation [3.20] and the stress strain curve gives the critical buckling stress. Results for the three cylinders investigated are found in section 9.5.

3.4 Circumferential Wavenumber

Since a sinusoidal mode shape is assumed in both directions, Koiter (1945) derived for very thin shells a formula that could give possible waveforms expressed as a semi-circle in "wavenumber space", given by Hunt (2003)

$$(m - m_{crown})^2 + n^2 = {m_{crown}}^2 \qquad [3.21]$$

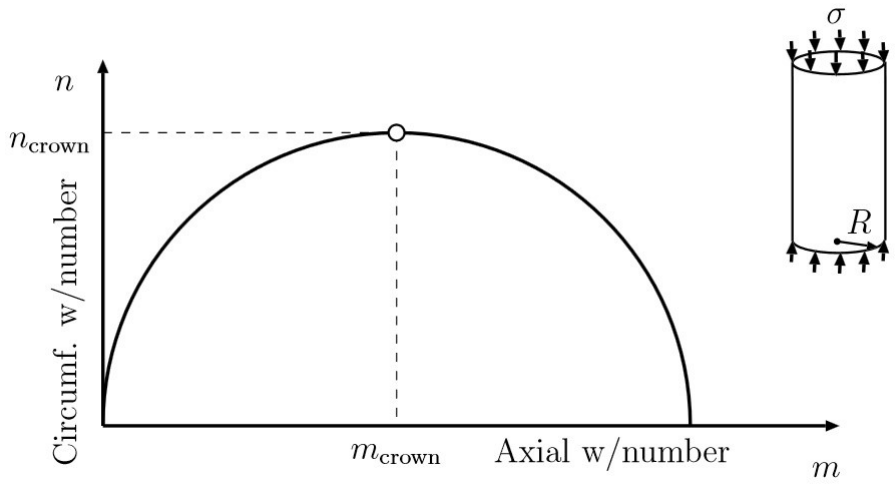

Figure 3.9 – Relationship between axial and circumferential wavenumber m and n, respectively.

The crown represents square wavenumbers, and the axial wavenumber $m \leq 2m_{crown}$ can be any positive value for a infinitely long cylinder, but the circumferential wavenumber $n \leq n_{crown}$ must be an integer. Donnells equation with a given sinusoidal mode shape from equation [3.4] can be used to find the circumferential wavenumber, n. Inserting $\beta_n = Ln/\pi r$ into equation [3.9] gives

$$\frac{Ln}{\pi r} = \sqrt{\left(\frac{12{Z_L}^2}{\pi^4}\right)^{\frac{1}{4}} m - m^2} \quad [3.22]$$

$$n^2\left(\frac{L}{\pi r}\right)^2 = \left(\frac{12\left(\frac{L^2}{rt}\sqrt{1-{v_e}^2}\right)^2}{\pi^4}\right)^{\frac{1}{4}} m - m^2 \quad [3.23]$$

Since the crown represents square waves it means that the length in both axial and circumferential direction will have to be equal, therefore its convienient to put $L = C_{circumference} = 2\pi r$.

$$n^2\left(\frac{2\pi r}{\pi r}\right)^2 = \left(\frac{12(2\pi r)^4(1-{v_e}^2)}{\pi^4(rt)^2}\right)^{\frac{1}{4}} m - m^2 \quad [3.24]$$

$$n^2 = \frac{2\pi r}{\pi\sqrt{rt}}\left(12(1-{v_e}^2)\right)^{\frac{1}{4}} m\frac{1}{4} - m^2\frac{1}{4} \quad [3.25]$$

$$n^2 = \frac{1}{2}\sqrt{\frac{r}{t}}\left(12(1-{v_e}^2)\right)^{\frac{1}{4}} m - m^2 \quad [3.26]$$

$$n^2 + m^2 = \left[\left(\frac{3}{4}\right)(1-{v_e}^2)\right]^{\frac{1}{4}}\sqrt{\frac{r}{t}}m \quad [3.27]$$

Equation [3.27] gives the value for the crown wavenumber for both axial and circumferential waves for a cylinder with length equal to $2\pi r$

$$n_{crown} = m_{crown} = \left[\left(\frac{3}{4}\right)(1-{v_e}^2)\right]^{\frac{1}{4}}\sqrt{\frac{r}{t}} \quad [3.28]$$

For cylinders with different length than $2\pi r$, a rescaling is required. M_a is introduced to represent the number of axial half-waves at the point of buckling in the shell of length L. Rescaling to a length $2\pi r$ and set $m = M_a\pi r/L$ and inserting into equation [3.26] yields

$$n^2 = M_a\pi\frac{r}{L}\sqrt{\frac{r}{t}}\left(12(1-{v_e}^2)\right)^{\frac{1}{4}} - {M_a}^2\pi^2\left(\frac{r}{L}\right)^2 \quad [3.29]$$

This is an equation for thin walled cylinder shells, and the cylinders investigated in this master thesis are not very thin, in fact they are not even in cross section class 4. Plots for

cylinders with different lengths are given in Appendix C compared to numerical analysis. In figure 3.10, different cylinders are plotted for $M_a = 6$ to get a overview of how n changes for different lengths, but from results given in Appendix C, its observed that n changes a lot when M_a changes.

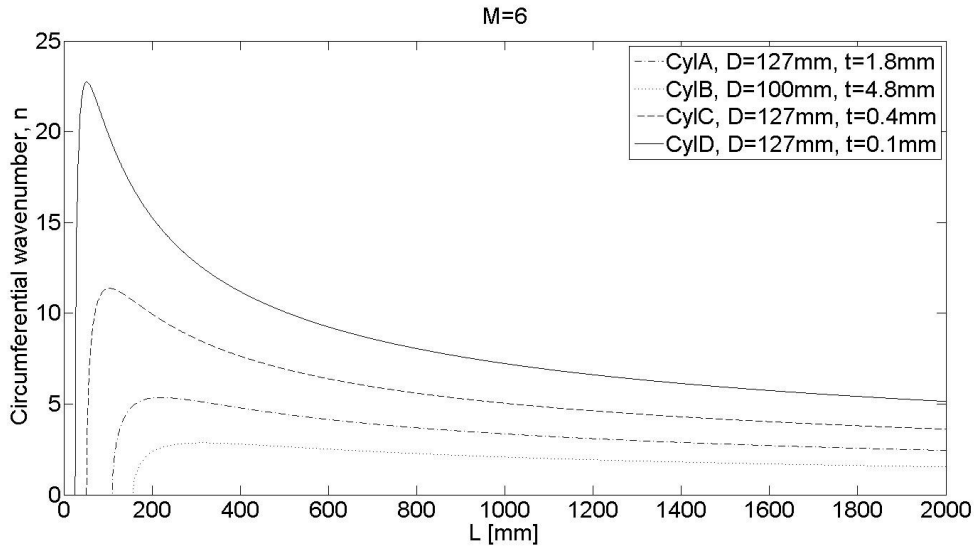

Figure 3.10 – Circumferential wavenumber from equation [3.29].

From the data from figure 3.10 its observed that equation [3.29] is only valid down to lengths equal to 18 mm and 16 mm for cylinder A and B, respectively. This fits great to the limiting results from equation [3.10], where the results are $L^A \geq 18.35$ mm and $L^B \geq 26.12$ mm. For shorter cylinders when the thickness are 1.8 mm and 4.8 mm, there will be less buckling effects and more like a compression test. Numerical analyses for cylinders in the range $20 < L < 400$ mm are given in Appendix C, compared with the analytical results. Laboratory experiments will not be performed in this master thesis due to time issue and the fact that these cylinders are not very thin, so the wavepattern will not occur on cylinder A and B. Figure 3.11 gives a visual result from one of the numerical analysis from Appendix C, cylinder C with length L=100 mm. Here its easy to identify the wavenumber in both axial and circumferential direction. M_a is 3 and n is 7. Equation [3.29] gives $n = 9.9$.

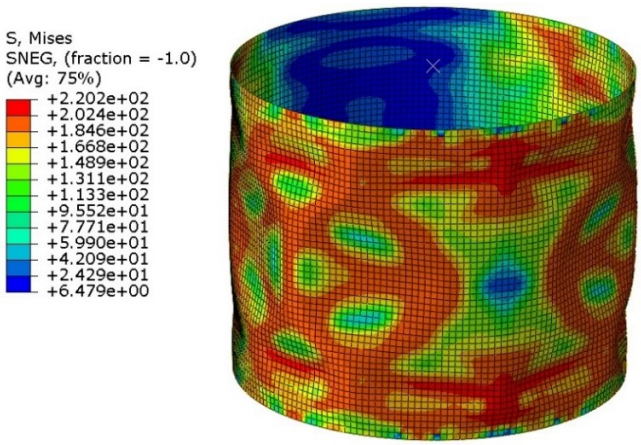

Figure 3.11 - Wavepattern using Riks method and S4R shell elements for D=127 mm, t=0.4 mm, L=100 mm.

For a very thin cylinder, its observed from figure 3.12 that the numerical and analytical analysis fits very well. Figure 3.13 is the associated cylinder with length L=100 mm. The analytical result is 18.7 compared to 23 for the numerical. From Appendix C the results does not give a perfect comparison between equation [3.29] and numerical analysis, and the reason can be that those cylinders are not very thin, therefore cylinder B (D=100 mm, t=4.8 mm) is not even considered because it is too thick.

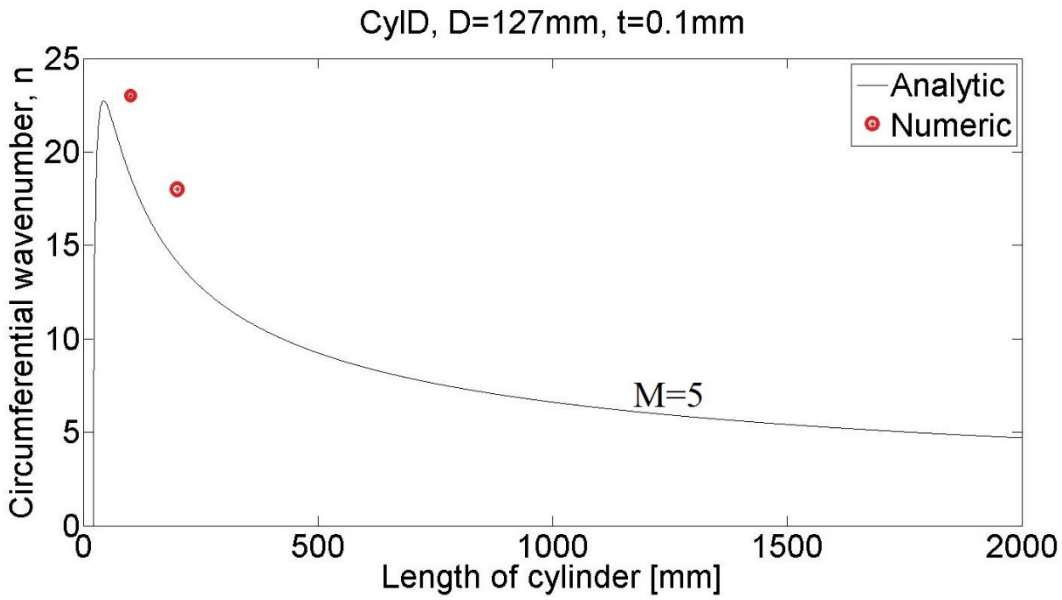

Figure 3.12 – Length versus circumferential wavenumber, n.

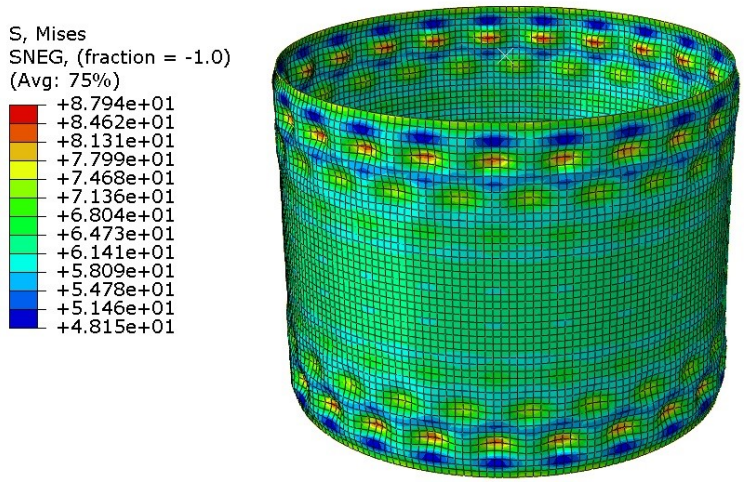

Figure 3.13 - Wavepattern from numerical analysis using Riks method and S4R shell element for D=127 mm, t=0.1 mm, L=100 mm. Displacement is 0.09 mm and deformation scale factor is 40.

3.5 Buckling Load for Pin-Ended Column

3.5.1 Buckling load for a column without imperfection

A sinusoidal curve is assumed for the deformation mode.

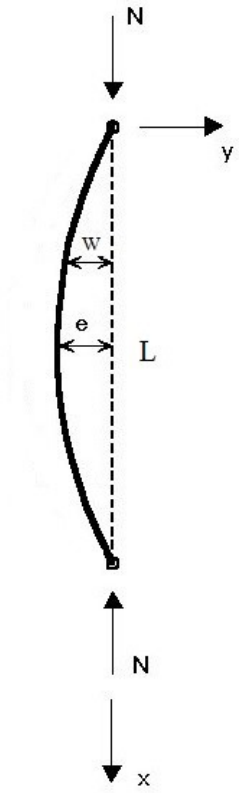

$$w = e \sin\frac{\pi x}{L} \qquad [3.30]$$

Figure 3.13 – Buckling of pin-enden column.

The relationship between the approximated curvature, deflection and the internal moment is known mechanic knowledge

$$\frac{1}{R} = w_{,xx} \qquad [3.31]$$

$$M = -EI\frac{1}{R} = -EIw_{,xx} \qquad [3.32]$$

Equilibrium gives

$$M = Nw = -EIw_{,xx} \qquad [3.33]$$

$$Ne \sin\frac{\pi x}{L} = eEI\left(\frac{\pi}{L}\right)^2 \sin\frac{\pi x}{L} \qquad [3.34]$$

Which gives the Euler buckling load

$$N_E = \frac{\pi^2 EI}{L^2} \quad [3.35]$$

If the exact expression for curvature from Appendix A is used, the stable form of the buckling load is shown:

$$\frac{1}{R} = \frac{w_{,xx}}{(1 + {w_{,x}}^2)^{\frac{3}{2}}} \quad [3.36]$$

$$Ne \sin\frac{\pi x}{L} = EI \frac{e\left(\frac{\pi}{L}\right)^2 \sin\frac{\pi x}{L}}{\left(1 + (e\frac{\pi}{L}\cos\frac{\pi x}{L})^2\right)^{\frac{3}{2}}} \quad [3.37]$$

$$N = EI \frac{\left(\frac{\pi}{L}\right)^2}{\left(1 + (e\frac{\pi}{L}\cos\frac{\pi x}{L})^2\right)^{\frac{3}{2}}} \quad [3.38]$$

Introducing series expansion of the cosine

$$\cos x = 1 - \frac{x^2}{2!} + \frac{x^4}{4!} - \frac{x^6}{6!} + \ldots \quad [3.39]$$

and dividing by N_E, an approximated solution can be found

$$\frac{N}{N_E} = 1 + \frac{\pi^2}{8}\frac{e^2}{L^2} \quad [3.40]$$

By plotting relative load vs relative deflection its observed that a stable post-buckling curve occur because the load capacity increases after buckling. It can also be noted that this is therefore a stable bifurcation point.

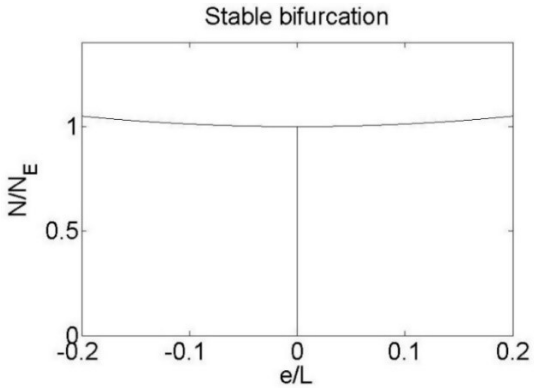

Figure 3.14 – Stable bifurcation.

3.5.2 Buckling load for a column with initial imperfection

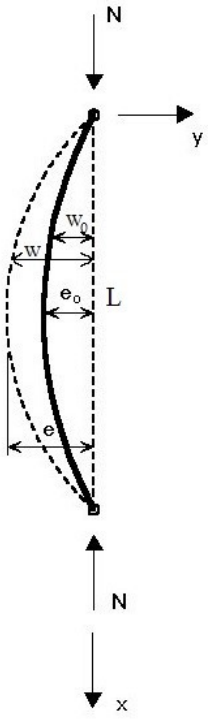

$$w_0 = e_0 \sin\frac{\pi x}{L} \quad [3.41a]$$

$$w = e \sin\frac{\pi x}{L} \quad [3.41b]$$

Figure 3.15 – Initial imperfection.

Moment equilibrium gives

$$Nw = -EI\left(w_{,xx} - w_{0,xx}\right) \quad [3.42]$$

$$Ne = EI\left(\frac{\pi}{L}\right)^2 (e - e_0) \quad [3.43]$$

$$Ne = N_E(e - e_0) \quad [3.44]$$

$$e = \frac{e_0}{1 - \frac{N}{N_E}} \quad [3.45]$$

Equation [3.45] is the imperfection factor including the initial imperfection, e_0. In a column with homogeneous pressure over the cross section, the critical yielding stress including the moment from the imperfection is given as

$$\sigma_y = \frac{N}{A} + \frac{M}{W_{el}} \quad [3.46]$$

Introducing $N_{el} = A\sigma_y$, $M_{el} = W_{el}\sigma_y$ and the fact that the moment comes from the deflection, $M = Ne$ and dividing [3.46] with σ_y gives

$$\frac{N}{N_{el}} + \frac{Ne}{M_{el}} = 1 \qquad [3.47]$$

Equation [3.45] will follow its path untill it reaches the Euler load, but the cross section will fail somewhere before that, following equation [3.47]. So the intersection between these to graphs will be the critical buckling load, N_{cr}.

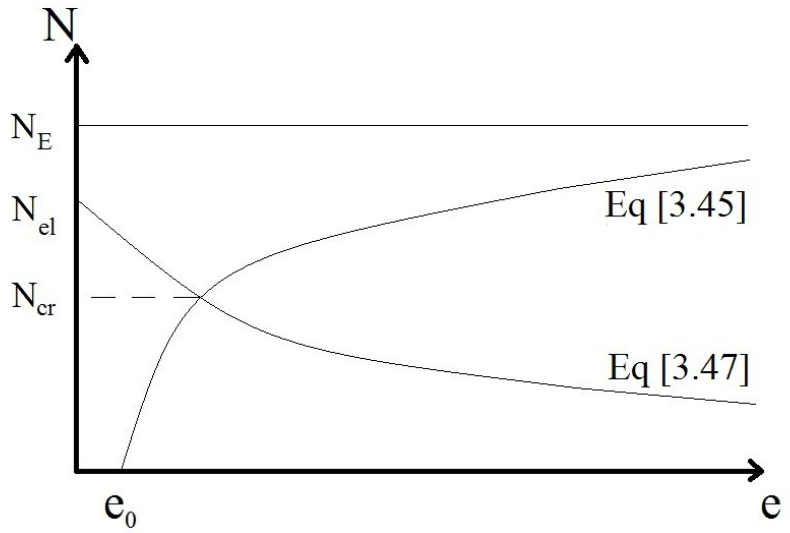

Figure 3.16 – Critical buckling load due to cross section capacity.

Observe that decreasing e_0 will increase N_{cr}, as it should be. The intersection point N_{cr} is found from inserting [3.45] into [3.47]

$$\frac{N_{cr}}{N_{el}} + \frac{N_{cr}}{M_{el}}\left(\frac{e_0}{1 - \frac{N_{cr}}{N_E}}\right) = 1 \qquad [3.48]$$

$$\frac{N_{cr}}{N_{el}} + \frac{N_{cr}}{N_{el}}\frac{N_{el}}{M_{el}}\left(\frac{e_0}{1 - \frac{N_{cr}}{N_{el}}\frac{N_{el}}{N_E}}\right) = 1 \qquad [3.49]$$

Introducing some scalars, $\bar{\lambda}^2 = N_{el}/N_E$ and $\alpha = e_0 N_{el}/M_{el}$

$$\frac{N_{cr}}{N_{el}} + \frac{N_{cr}}{N_{el}}\left(\frac{\alpha}{1 - \frac{N_{cr}}{N_{el}}\bar{\lambda}^2}\right) = 1 \qquad [3.50]$$

Solving this for N_{cr}, a function of imperfection, length, cross section capacity and the residual stresses can be obtained

$$N_{cr} = \frac{N_{el}}{2}\left(1 + \frac{1+\alpha}{\bar{\lambda}^2} - \sqrt{\left(1 + \frac{1+\alpha}{\bar{\lambda}^2}\right)^2 - \frac{4}{\bar{\lambda}^2}}\right) \quad [3.51]$$

3.5.3 Buckling load for a column in axial compression and bending at ends

By putting on equal moments on each side, an equal homogen moment-diagram will occur, and the critical cross section stress can be calculated.

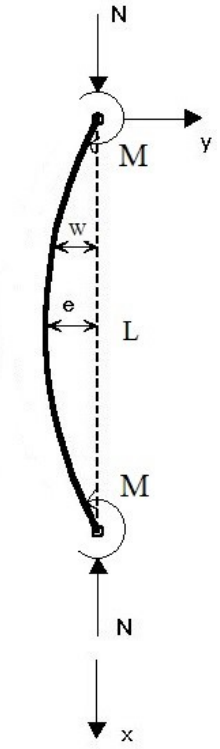

Figure 3.17 – Axial compression and bending at ends.

If axial load is the only force acting, then

$$N_{Rk} = \chi A f_o \quad [3.52]$$

where χ is a reduction factor for the relevant buckling mode. Further, its assumed that failure occurs when the maximum compression stress at the mid section reaches the yield stress f_o, and equation [3.46] is therefore valid

$$\frac{N_{Rk}}{A} + \frac{N_{Rk}e}{W_z} = f_0 \quad [3.53]$$

$$e = \frac{W_z f_o}{N_{Rk}}\left(1 - \frac{N_{Rk}}{A f_o}\right) \quad [3.54]$$

$$w = e \sin\frac{\pi x}{L} \quad [3.55]$$

If now bending moments are acting at the ends, the total maximum compressive stress is

$$f_o = \frac{N}{A} + \frac{M_z}{W_z} + \frac{Nw}{W_z} \quad [3.56]$$

Inserting equation [3.55] into equation [3.56] yields

$$f_o = \frac{N}{A} + \frac{M_z}{W_z} + \frac{N W_z f_o}{W_z N_{Rk}}\left(1 - \frac{N_{Rk}}{A f_o}\right)\sin\frac{\pi x}{L} \quad [3.57a]$$

$$f_o = \frac{N}{A} + \frac{M_z}{W_z} + \frac{N f_o}{N_{Rk}}\left(1 - \frac{N_{Rk}}{A f_o}\right)\sin\frac{\pi x}{L} \quad [3.57b]$$

$$\frac{N}{f_o A} + \frac{M_z}{f_o W_z} + \frac{N}{N_{Rk}}\left(1 - \frac{N_{Rk}}{A f_o}\right)\sin\frac{\pi x}{L} = 1 \quad [3.57c]$$

$$\frac{N}{f_o A} + \frac{M_z}{f_o W_z} + \frac{N}{N_{Rk}}(1 - \chi)\sin\frac{\pi x}{L} = 1 \quad [3.57d]$$

$$\frac{N}{N_{Rk}}\left(\frac{N}{f_o A}\frac{N_{Rk}}{N} + (1 - \chi)\sin\frac{\pi x}{L}\right) + \frac{M_z}{M_{Rk}} = 1 \quad [3.57e]$$

$$\frac{N}{\chi A f_o}\left(\chi + (1 - \chi)\sin\frac{\pi x}{L}\right) + \frac{M_z}{M_{Rk}} = 1 \quad [3.57f]$$

$\chi + (1 - \chi)\sin\frac{\pi x}{L}$ has its maximum when $x = L/2$, which means that the midsection of a column is the most critical point. By introducing a factor ω equation [3.57f] yields

$$\frac{N}{\omega \chi A f_o} + \frac{M_z}{M_{Rk}} = 1 \quad [3.58]$$

where

$$\omega = \frac{1}{\chi + (1 - \chi)\sin\frac{\pi x}{L}} \quad [3.59]$$

This factor is found in EC9 as well and its usefull for calculations of welds for flexural buckling. L is the buckling length in the buckling plane considered and x is the distance to the weld from the upper end. This factor is linear related to the critical buckling load for flexural buckling.

4 Calculations from Eurocode 9

4.1 Flexural Buckling

Eurocode 9 gives the buckling load for a given cylinder. Due to lack of research on aluminium and possible conservative statements, these rules are most likely very conservative. Figure 4.1 shows the relation between critical buckling load and length for the three unwelded cylinders investigated in this study, and its corresponding relative buckling curves are given in figure 4.2 when the length ranging from 0 to 5 m. Its observed for short cylinders that the critical buckling load is almost identical due to local buckling.

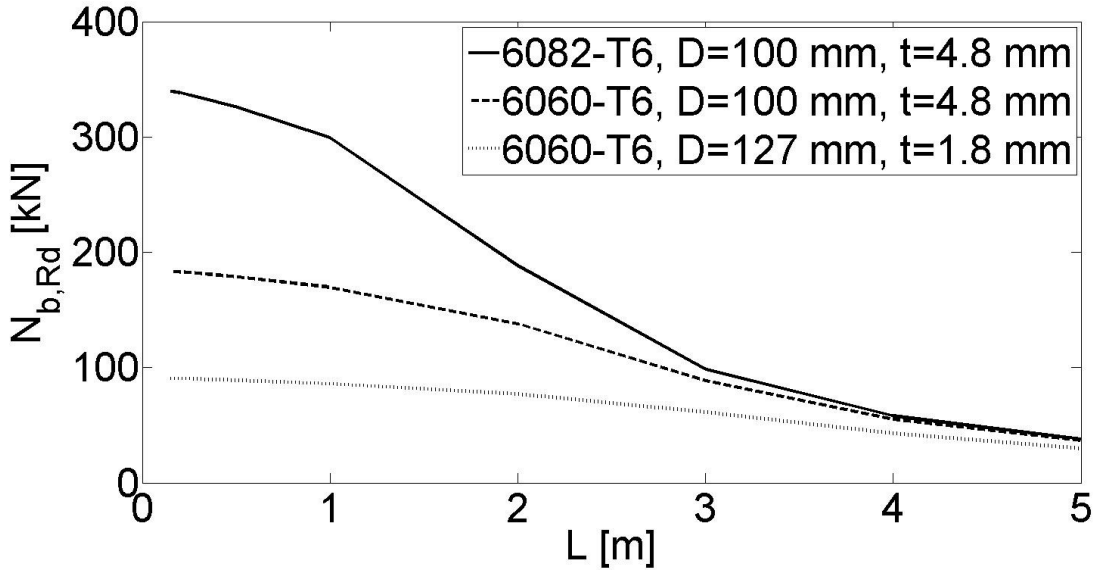

Figure 4.1 – Critical buckling load calculated by EC9.

The critical buckling load for flexural buckling is given in EC9 as

$$N_{b,Rd} = \kappa \chi A_{eff} f_o / \gamma_{M1} \quad [4.1]$$

where κ is a factor to allow for the weakening effects of welding. Without welds $\kappa = 1$. χ is the reduction factor for the relevant buckling mode, and for short cylinders $\chi = 1.0$ due to local buckling. f_o and γ_{M1} is the characteristic value of 0.2% proof strength and partial factor for resistance of cross sections equal to 1.1, respectively, and the effective area is equal to the cross section area, A for cross section class 1,2 and 3. For class 4, the area is multiplied by a factor ρ_c to factor down the thickness of the cylinder.

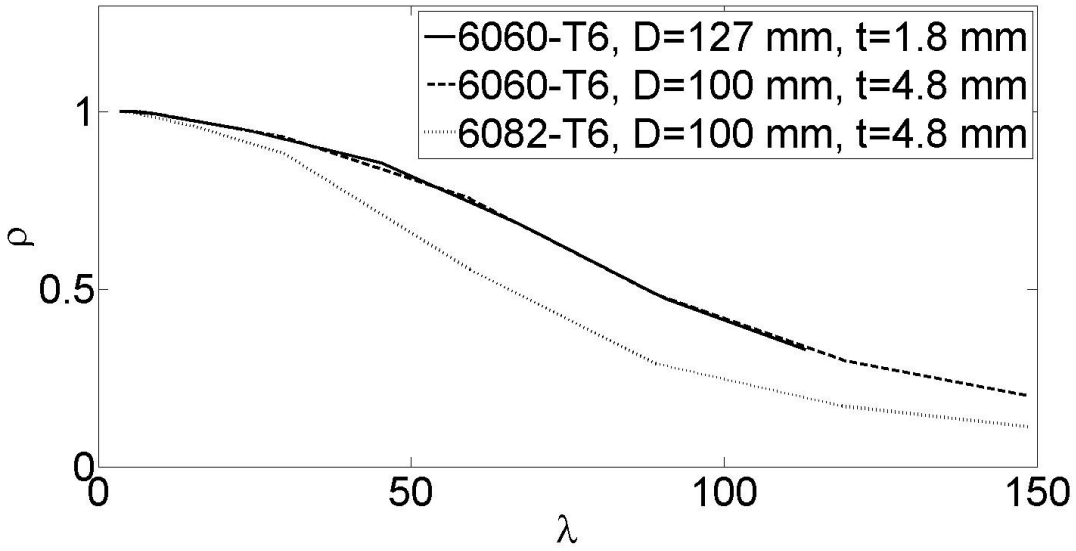

Figure 4.2 – Relative buckling stress vs slenderness.

Figure 4.2 is given by the slenderness, λ and the relative buckling stress, ρ, where $\lambda = L/i$, $\rho = \sigma_{cr}/f_o$, $i = \sqrt{I/A}$ and $\sigma_{cr} = N_{b,Rk}/A$.

4.2 Local Buckling

As observed from figure 4.1 the critical buckling load is almost the same for short cylinders, due to local buckling. Local buckling is given in Eurocode 9 (2007) as

$$N_{c,Rd} = A_{eff} f_o / \gamma_{M1} \qquad [4.2]$$

where the effective area is the same as for flexural buckling, but when welds are applied, its calculated as shown on the next page. For a cylinder subjected to welding in cross section class 1,2 and 3, the effective area is reduced around the weld as shown in figure 4.4a by introducing the factor $\rho_{o,haz}$, which is given in EC9. When cylinders are in cross section class 4, the effective area is reduced for the whole cross section as well. But for cylinders in class 4, the reduction around the welds can not be less than the reduction for the rest of the cross section, EC9 (2007).

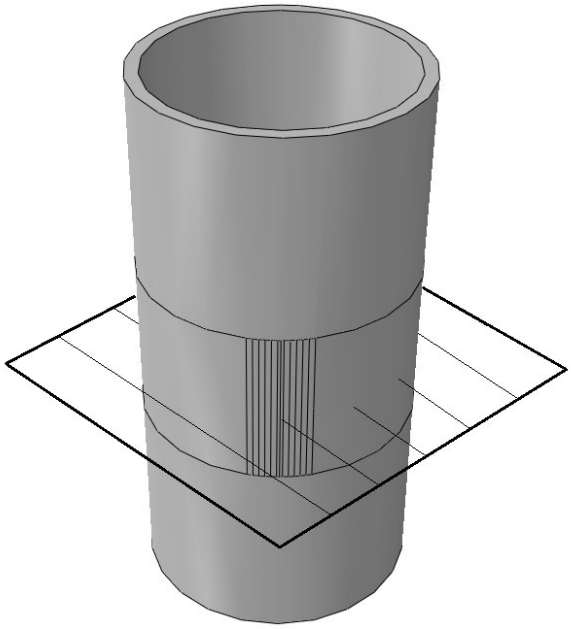

Figure 4.3 – Datum of welded cross section corresponding to figure 4.4.

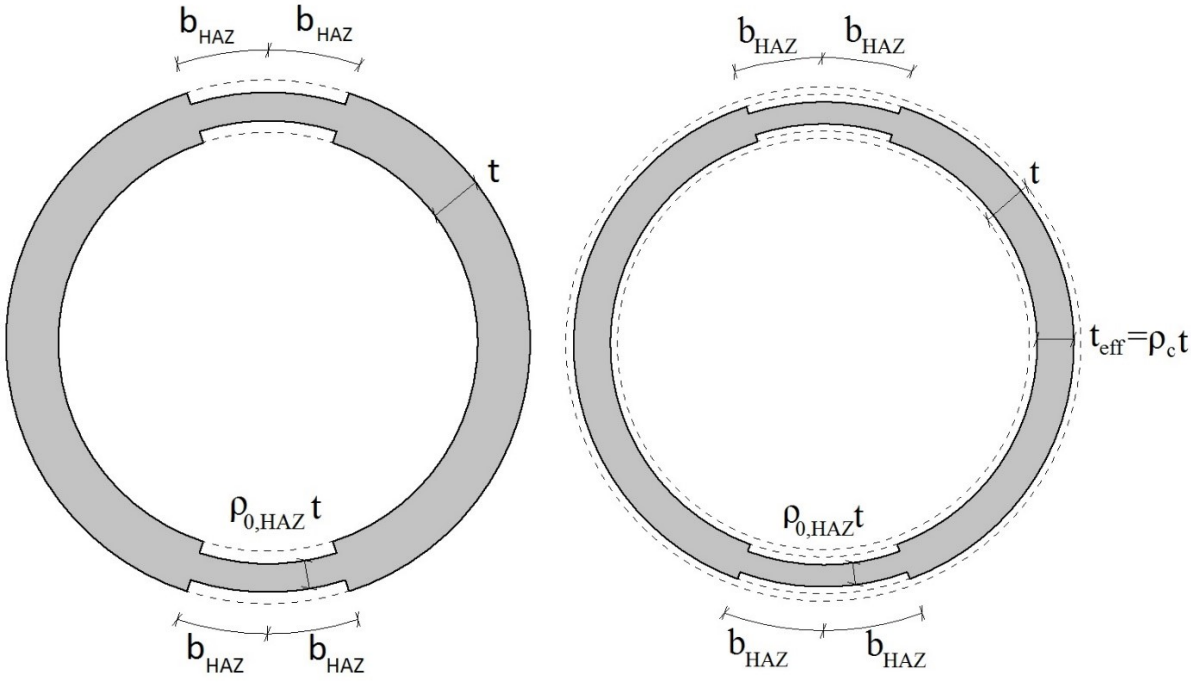

Figure 4.4 – Reduced area due to weld effects for a) class 1,2 and 3 and b) class 4.

By using the geometry in figure 4.4a, the equation for the effective area for cross section class 1,2 and 3 becomes

$$A_{eff} = A_{tot} - 2\left(2b_{haz}\left(t - \rho_{o,haz}t\right)\right) \qquad [4.3]$$

$$A_{eff} = A_{tot} - 4b_{haz}t(1 - \rho_{o,haz}) \quad [4.4]$$

where the total area is

$$A_{tot} = 2\pi rt \quad [4.5]$$

For cross section class 4, the effective area is calculated the same way but now the thickness is replaced with a effective thickness for the cross section, t_{eff}

$$t_{eff} = \rho_c t \quad [4.6]$$

Around welds for class 4, the reduction factor is taken as

$$min\{\rho_{o,haz}t;\ \rho_c t\} \quad [4.7]$$

In this study, two cylinders in class 1,2 or 3 and one cylinder in class 4 are investigated. The 6060-T6, D=127 mm, t=1.8 mm cylinder is in class 4 when subjected to welding. The ρ_c factor for this cylinder when subjected to welding is found to be 0.984. The $\rho_{o,haz}$ factor is 0.43 and 0.48 for alloy 6060-T6 and 6082-T6, respectively and is given in EC9 as:

$$\rho_{o,haz} = \frac{f_{o,haz}}{f_o} \quad [4.8]$$

EC9 assumes that throughout the heat affected zone (HAZ) the strength properties are reduced on a constant level, but section 5.3 shows that this is not right and results comparing EC9 and laboratory experiments for welded cross sections are given in section 9.

5 Material Test

5.1 Introduction to DIC

Material tests are necessary to establish the correct stress strain relation for the investigated cylinders, and tensile tests are the cheapest way to get this relation. This is done by cutting out a dog-bone looking piece from the given cylinder and putting it into a stretching machine. This machine logs both force and displacement, and the stress strain relation can therefore be found. Due to many parts between the specimen and the machine, the displacement logged is not as accurate as it should be, based on earlier experiments. All parts in the machine are made out of steel and even though steel has much higher Young`s modulus than aluminium, the total elongation in these parts makes it non-accurate. Therefore, a another much more expensive method was used, digital image correlation (DIC). This method takes high resolution pictures during the tests and by analysing the pictures afterwards, the strain can be found and fitted with the stress values from the tensile machine. Strain is a dimensionless number and its usually found from elongation of a known length of a specimen, but DIC uses relative pixel sizes found from the pictures. Therefore, very many pictures are needed during one tensile test to get an accurate result. The tests performed in this study are quasi static, which means they are loaded very slowly. In fact its deformation controll to ensure the correct force. One test took about ten minutes, and five pictures were taken every second so in total about 3000 pictures for every test. This is to ensure absolute every changes that happens in the material, specially around yielding and necking. The changes are found from meshing the specimen so every points inside one element will follow its position inside the given element. Figure 5.1a and b shows how a 25x25 pixel Q4 element is meshed onto a tensile specimen for the initial and last picture before necking, respectively. The principal strain, ε_1 is mapped in figure 5.1c.

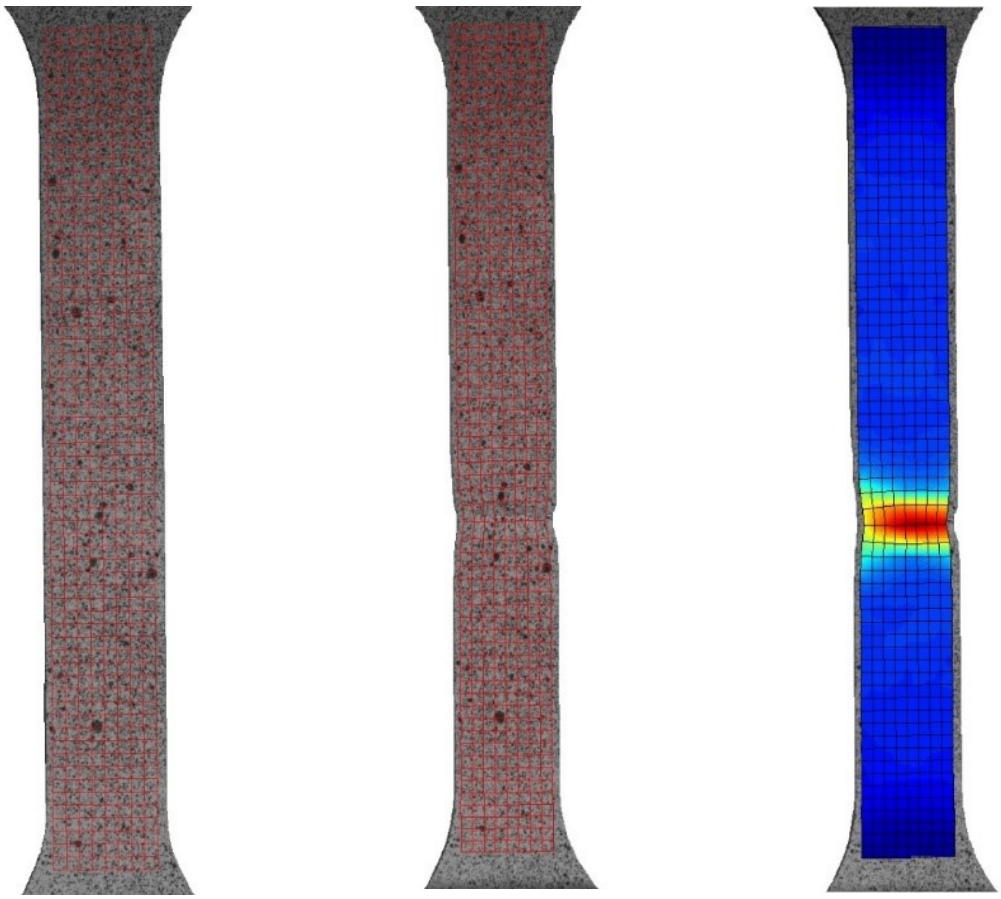

a) b) c)

Figure 5.1 - 25x25 pixels Q4 element is meshed onto a tensile specimen for the a) initial and b) last picture before necking. The principal strain, ε_1 is mapped in c).

Unlike FEA, the mesh in DIC can not be refined so it converges to a limit. The elements in DIC needs a suitable size to ensure that every point stays at that point within the element. If the element size was so small that there only was one dot in every picture, the analysis would fail. Therefore, a size 25x25 pixels are used, which is a great balance between enough dots and capable of representing a accurate strain behaviour. With this size, there was eight elements over the width to represent the strain for the elements were necking occurs, and due to different unit vector of these elements, some shear strain will affect the results and therefore the whole logaritmic strain matrix has to be concerned. Further is the mean value assumed for the strain.

$$\bar{\varepsilon}_L = \begin{bmatrix} \varepsilon_{xx} & \varepsilon_{xy} \\ \varepsilon_{yx} & \varepsilon_{yy} \end{bmatrix} \quad [5.1]$$

Figure 5.2 shows a Q4 element used in this analysis with enough dots inside to establish an accurate result. The dots are painted on each specimen.

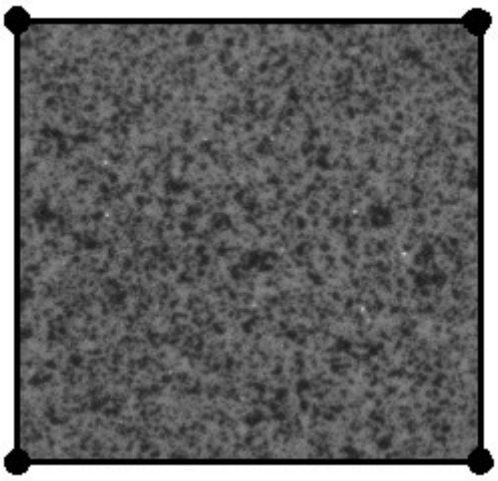

Figure 5.2 – 25x25 pixels Q4 element.

5.2 Tensile Test

Three tensile tests were performed for each of the three different cylinders in this master thesis, in total 9 tests. The design of the tensile test is shown in figure 5.3, including the cameras for the DIC analysis. Its clearly that there are many components that will in some degree have an elastic elongation when tension is applied even though they are made out of steel, so strains are found by DIC. In figure 5.4, the specimens are shown. It was observed that the elastic domain was equal for every tests and that Young`s modulus was 70 GPa, as expected. The plastic domain however, gave a fine and smooth graph when plotting the plastic strain vs the true stress for aluminium alloy 6060-T6, but gave a large scatter for alloy 6082-T6, as seen in figure 5.5a, b and c, respectively. Its also noted that the graph fits very good for all of the three tests in the beginning and in the transition from elastic to plastic domain. This is a good observation because buckling is probably very sensitive in this region. The necking point is not very coordinated for none of the tensile tests, and the engineering knowledge about buckling should be applied when choosing values to be used in the numerical analysis. Since the tests gave a large scatter for alloy 6082-T6, its obviously that more tensile tests should be performed, but due to time issue, the numerical analysis will be based on these tests. When tensile tests are performed with some scatter in the result, the mean values from the tests are normally used to establish the stress strain relation in numerical analysis. A reason for the large scatter, special in alloy 6082-T6 is most likely due to an extrusion weld made when producing the cylinders.

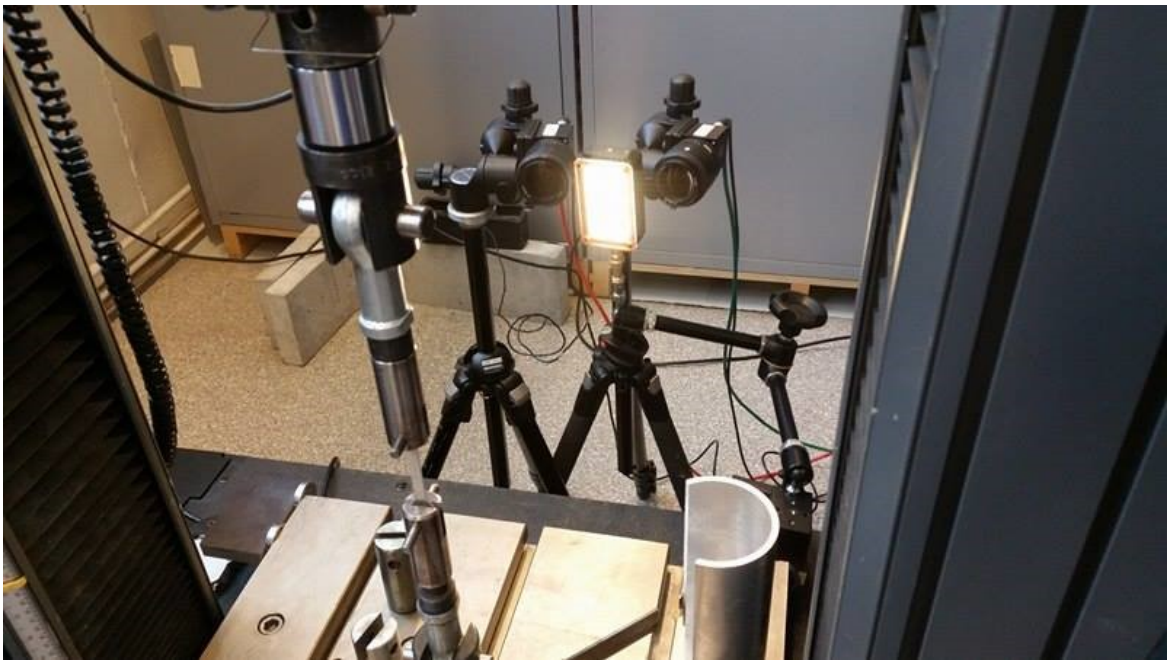

Figure 5.3 – Design of the tensile test.

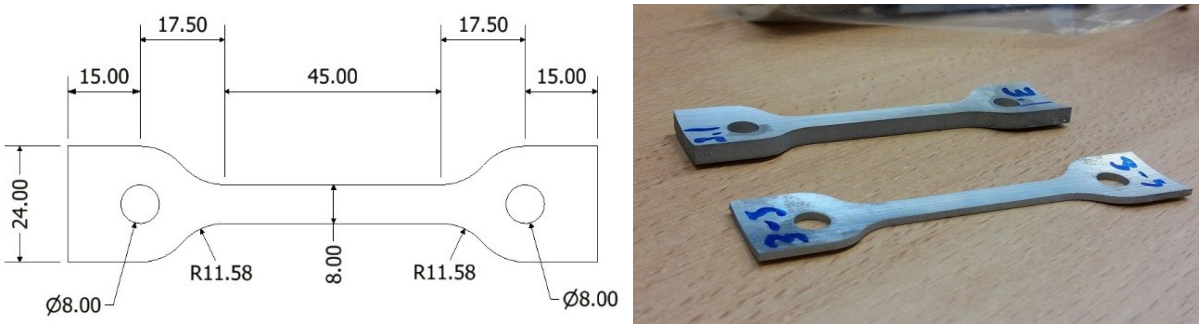

a) b)

Figure 5.4 – a) Projected drawing of the specimens and b) specimens with curvature.

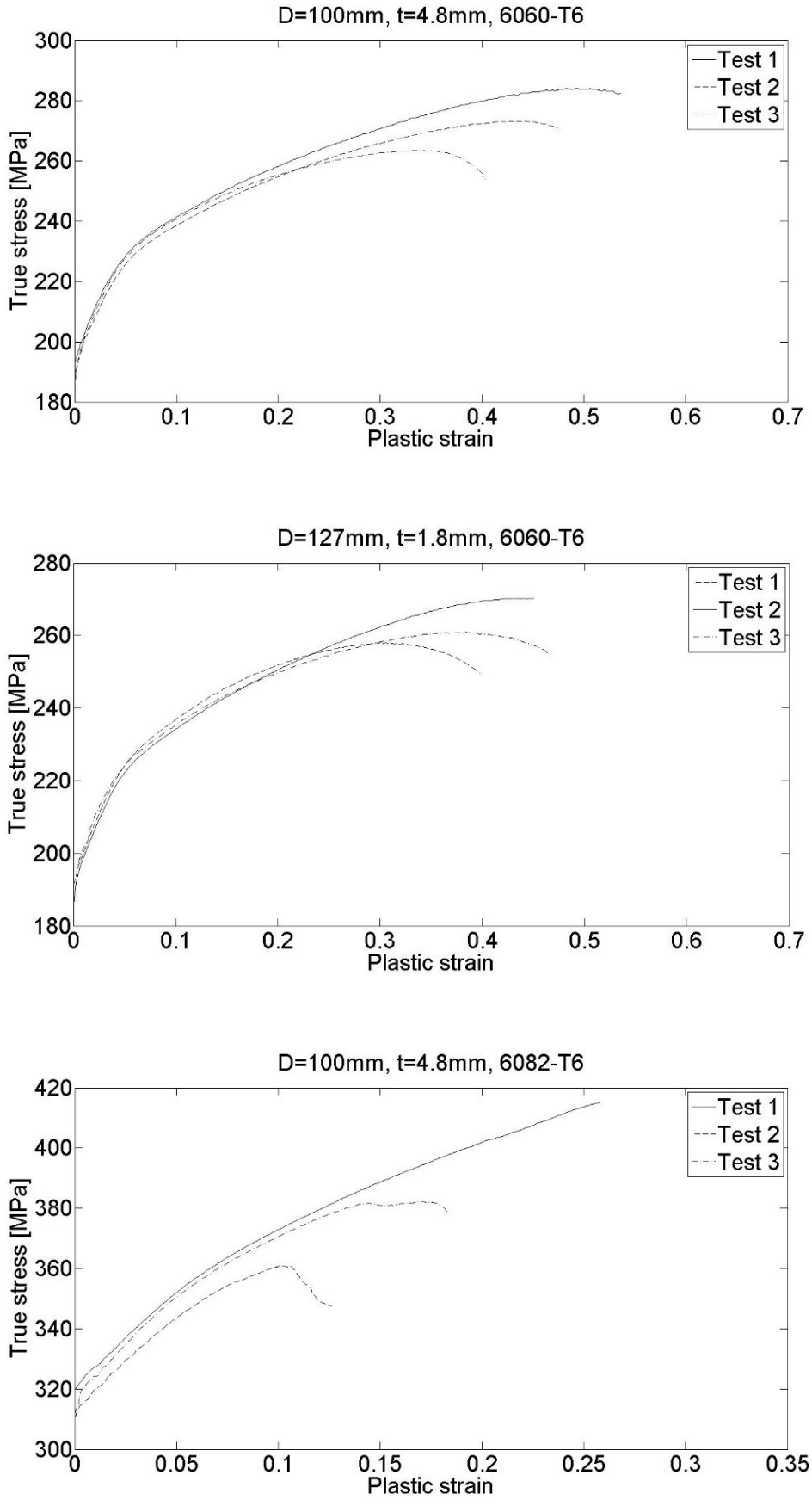

Figure 5.5 – True stress vs plastic strain from tensile tests.

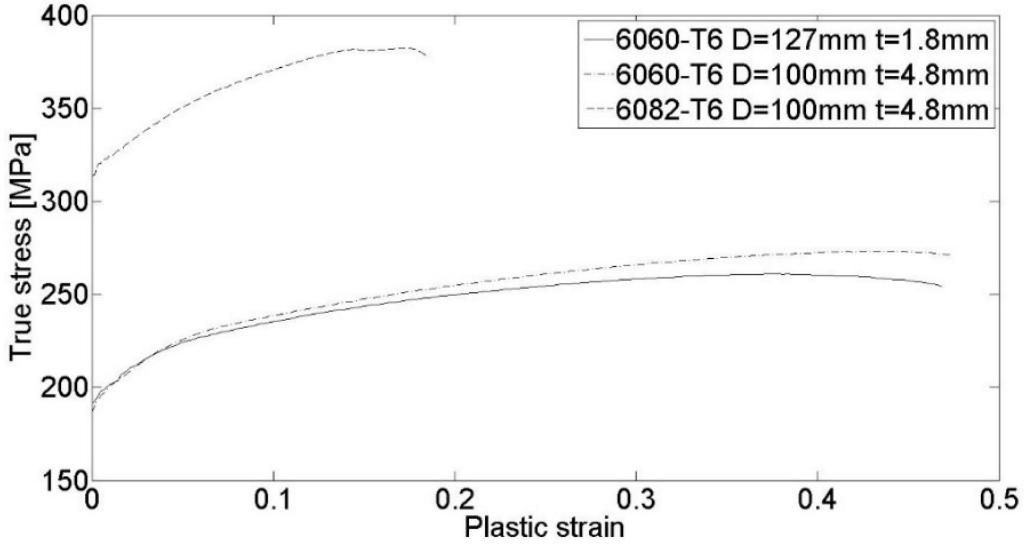

Figure 5.6 – Mean values from the three tests used in the numerical analysis.

As expected, more strength in a material decreases its ductile properties, and alloy 6082-T6 necks for much lower strain values than alloy 6060-T6.

The f_o parameters are taken from figure 5.6 when the plastic strain is equal to 0.002 and are listed in table 5.1 for the three cylinders. For the elastic part, a Young`s modulus equal to 70000 MPa has been used to calculate the stress corresponding to 0.2% permanent strain.

Table 5.1 - f_o values taken from 0.2% permanent strain.

Cylinder	f_o [MPa]
6060-T6, D=100 mm, t=4.8 mm	192.23
6060-T6, D=127 mm, t=1.8 mm	193.63
6082-T6, D=100 mm, t=4.8 mm	314.56

Figure 5.7 shows the five parameter extended Voce rule and Ramberg & Osgood constitutive law fitted by the least square method to the true stress vs plastic strain from the tensile tests.

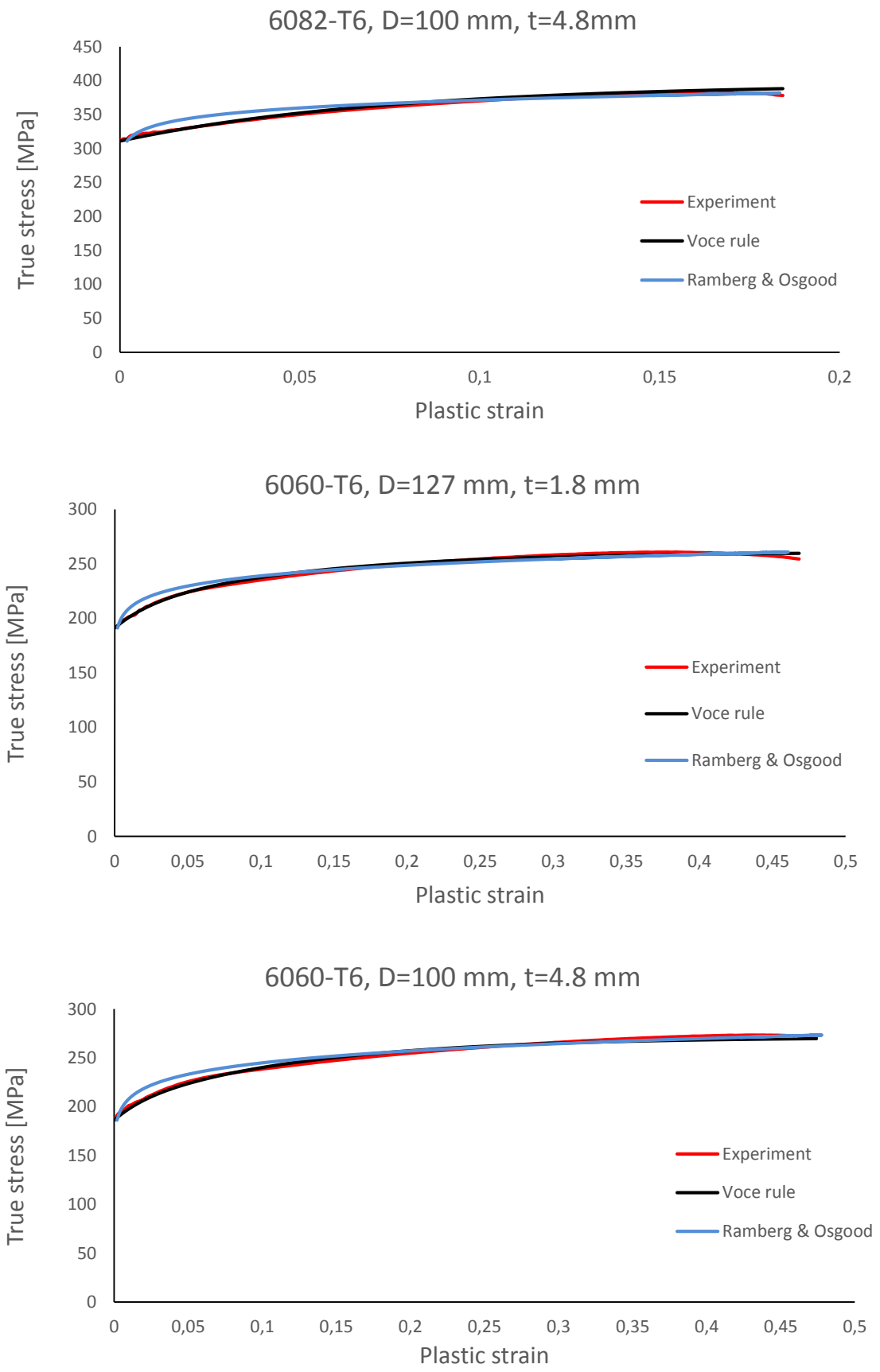

Figure 5.7 – Voce rule and Ramberg & Osgood fitted to the laboratory tensile test results.

Voce rule gives significant more accurate results, so this material formula will be used in the numerical study. Table 5.2 gives the hardening parameters from the curve fitting.

Table 5.2 – Hardening parameters for Voce rule and material parameter for Ramberg & Osgood.

Cylinder	Y_0 [MPa]	Q_1 [MPa]	C_1 [-]	Q_2 [MPa]	C_2 [-]	$\sigma_0 + \sum Q_i$ [MPa]	Ramberg & Osgood, n_{RO} [-]
6082-T6 D=100 mm, t=4.8 mm	311	28	9	57	15	396	22
6060-T6 D=127 mm, t=1.8 mm	191	18	40	51	8	260	17.5
6060-T6 D=100 mm, t=4.8 mm	186	16	50	69	8	271	14.3

The reason why two different tensile tests were performed for the same material was because it did not have the same geometry, and different stress-strain values were expected. Figure 5.6 shows that due to different geometry, the thicker specimen gave little higher stress values. Therefore, it can be concluded that there are no such thing as a perfect tensile test of a material. There will always be some edge effects and some effects from the cooling rate from the extrusion when making the profiles, and tensile tests therefore have to be performed for the same profiles that are analysed numerically.

The specimens had a little curvature because they were cut out from the corresponding cylinders and this may affect the results. First, the area is assumed rectangular when establishing the stress strain relation, so how wrong this is, is shown in table 5.3.

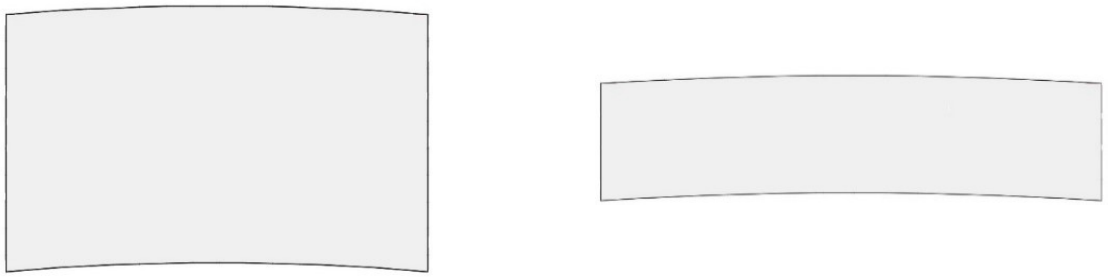

a) b)

Figure 5.8 – Cross section of tensile specimens. a) D=100 mm and b) D=127 mm.

Table 5.3 – Deviation calculations for curved vs rectangular cross sections.

Specimen from cylinder	$A_{rectangular}$ $[mm^2]$	A_{curved} $[mm^2]$	$\frac{A_{curved}}{A_{rectangular}}$
6060-T6 D=127 mm, t=1.84 mm	14.5360	14.5166	0.99866
6060-T6 D=100 mm, t=4.82 mm	38.0780	37.9898	0.99768
6082-T6 D=100 mm, t=4.81 mm	37.9990	37.9110	0.99768

With correct curvature the area is 0.134 %, 0.232% and 0.232% below the area used to establish the stress strain relation for D=127 mm (6060-T6), D=100 mm (6060-T6) and D=100 mm (6082-T6), respectively. Equation [2.14] shows that there is a linear relation between the initial area and the true stress, and therefore, based on the assumption that the specimens are rectangular, the true stress used in the numerical analysis will lay 0.134%, 0.232% and 0.232% below, respectively. This is negligible.

Second, the curvature may affect the tension test itself. Edge effects and complex shear forces may occur due to uniaxial tension of a transverse curvature, and the curvature may want to "straighten-up" during a tensile test. To ensure that this effect is negligible, both rectangular and curved specimens are analysed numerically and compared together, with the material parameters found from tensile tests of curved specimens since this is the only tests done in this study. The maximum force is compared for the numerical studies with rectangular and curved cross sections, but also with the test results from the tensile tests performed in lab to observe inequalities. Since the tensile tests performed in lab gives very inaccurate displacements, due to many parts in the rig, some corrections are done. As mentioned before, numerical analysis are based on strains taken from DIC, and are therefore very accurate. Figure 5.9 shows a simple 1 DOF system with two springs, representing the displacement of the specimen, and all the associated components, u_1 and u_2, respectively.

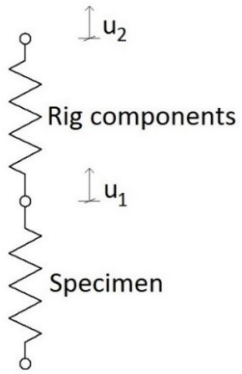

Figure 5.9 – 1 DOF system representing the displacement in the tensile test.

The force is the same in all components and by using Hook`s law, an equation for displacement of the specimen yields:

$$F = \sigma A_0 = E\varepsilon A_0 = EA_0 \frac{u_1}{L} \quad [5.2]$$

$$u_1 = \frac{FL}{EA_0} \quad [5.3]$$

The total displacement of the rig and specimen is logged by the testing machine and is given as

$$u_{tot} = u_1 + u_2 \quad [5.4]$$

If u_2 is plotted against the force, a curve can be fitted to the graph combining Voce rule and a linear term, as shown in figure 5.10, where red is the fitted curve.

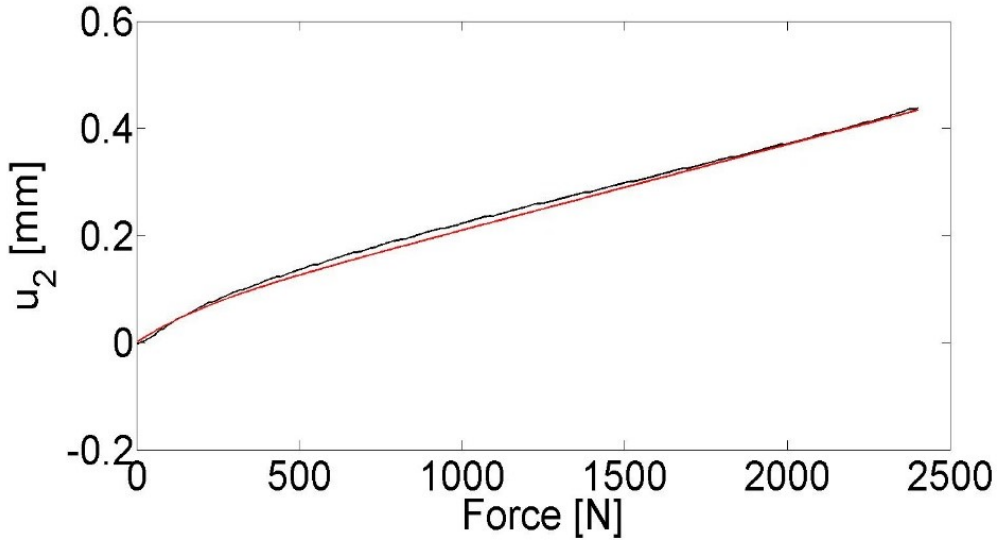

Figure 5.10 – Rig displacement versus load for alloy 6060-T6, D=127 mm, t=1.8 mm.

When the displacement of the machine, u_2 is known, this fitted curve is used to find the exact displacement in the specimen, and figure 5.11a, b and c shows the comparison between the tensile tests performed in lab with numerical analysis, both rectangular and curved cross sections. Matlab script for finding displacement for the specimens are given in Appendix F.

Figure 5.11a, b and c shows almost completely equal graphs for rectangular and curved cross sections, i.e. no curve effects. They are very equal to the ones performed in lab as well, except for alloy 6082-T6 were the elastic stiffness is a little higher for the one performed in lab. Somehow, rupture of the elements in the numerical analysis were not possible, so the deformation of the tests just kept on going long past the fracture point. Since this was of no interest here the problem was not solved.

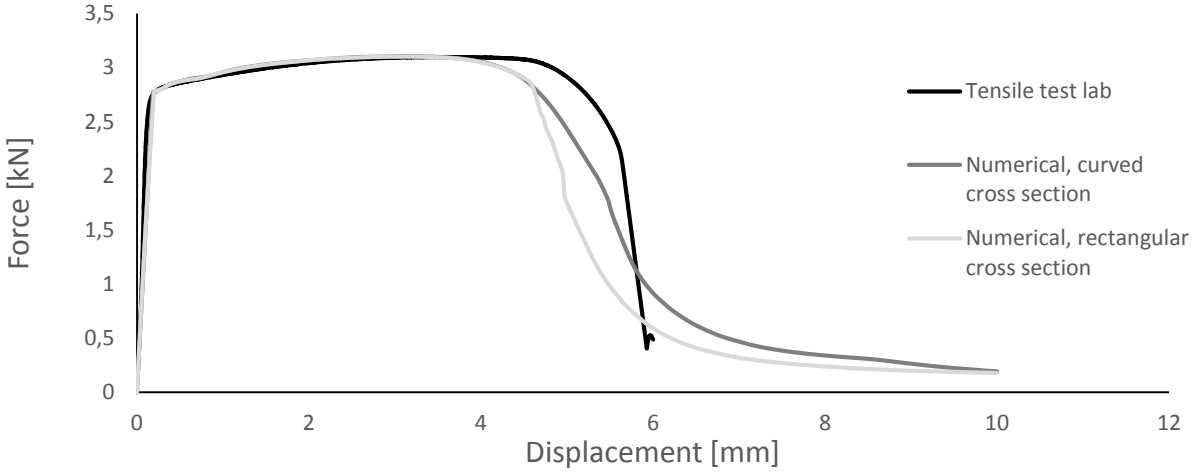

Figure 5.11a – Alloy 6060-T6, D=127 mm, t=1.84 mm.

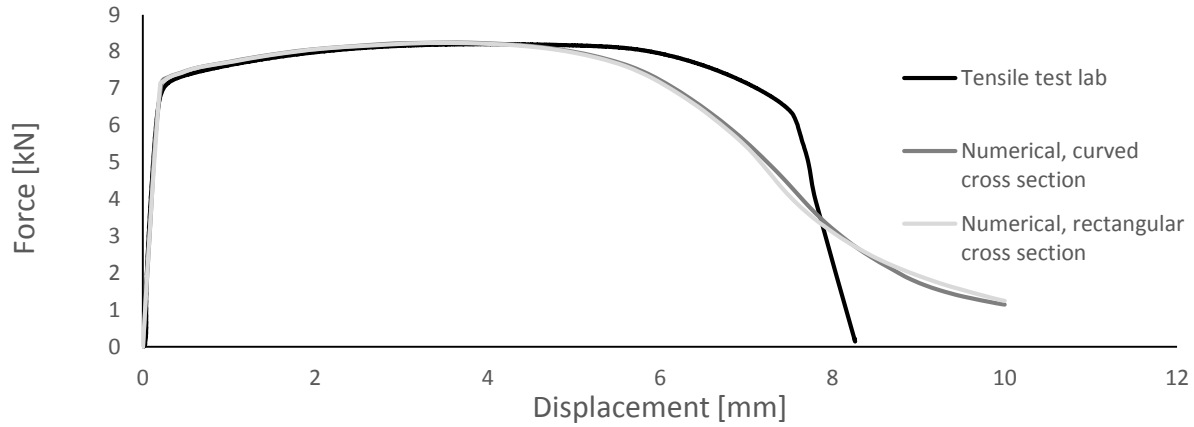

Figure 5.11b – Alloy 6060-T6, D=100 mm, t=4.82 mm.

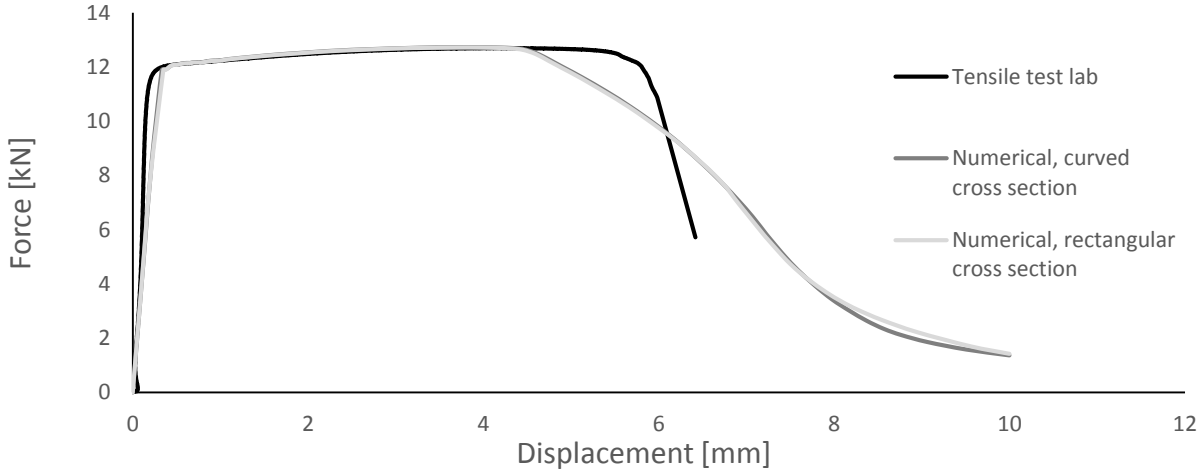

Figure 5.11c – Alloy 6082-T6, D=100 mm, t=4.81 mm.

5.3 Material Parameters for Weld, HAZ and Base Material

When cylinders are used in the industry, they are often welded together due to lack of possible connection designs and cheap solutions. Bolts are very rare used due to practical issues when tighting components together. Figure 5.12a shows a typical connection point between cylinders, and its clearly that there are no way to use bolts in this design. Another reason to weld in cylinders will be when lugs are needed, as shown in figure 5.12b.

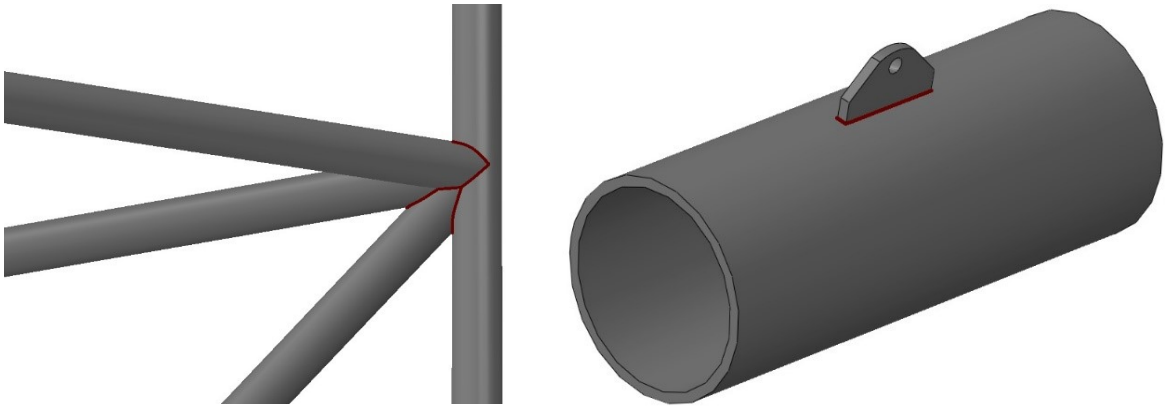

a) b)

Figure 5.12 – a) Welded connection joint of cylinders and b) welded lug onto a cylinder.

When aluminium is welded, the material parameters are weakened as mentioned in section 2.3, and the heat affected zone are spreading spherical out from the weld tip. This master thesis will only investigate how much welding reduces the buckling strength, and therefore no other components can be attached to the cylinders tested, i.e. no lugs or attached cylinders. Figure 5.13a and b shows the difference between attaching a component versus just a weld on the outside of a cylinder. Its known that the weld itself is not the weakest link, but the material in HAZ nearest the weld. Since it will give approximately the same size of the HAZ, these two methods will be very simular, and figure 5.13b is therefore a decent method to compare with, and will be performed both experimentally and numerically. A comment on this assumption is that the weld will work as a stiffener on the outside, with height equal to the throatsize. The only solution would be to cut the cylinders lengthwise and weld them together so the weld wouldn`t lay on the outside. Since the weld will not be placed at the whole length of the cylinder, there are no easy way to do this, and figure 5.13b will still be performed as mentioned.

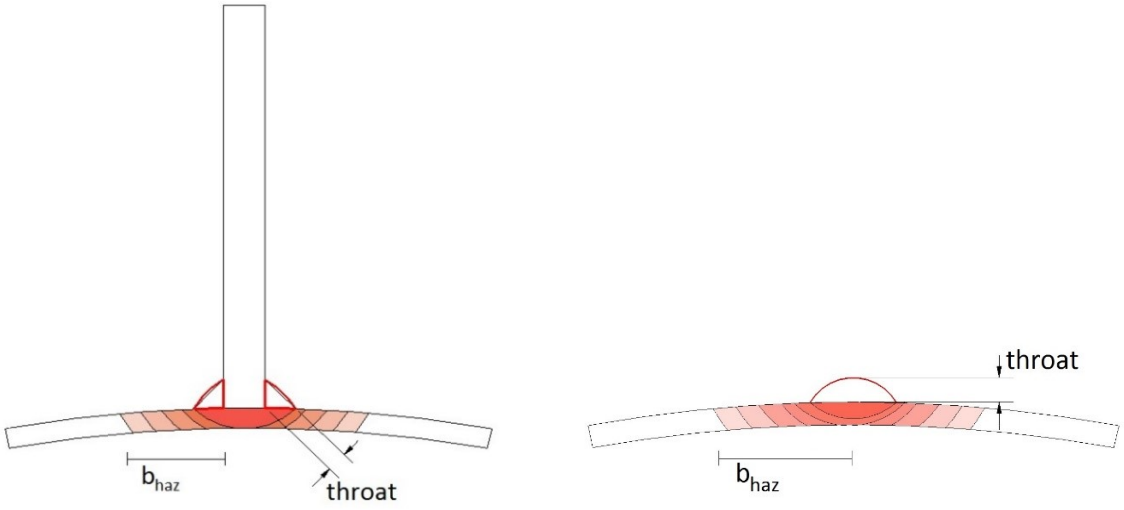

a) b)

Figure 5.13 – HAZ for a) associated component welded on a cylinder wall and b) fillet weld laid onto a cylinder wall.

The welds are performed by Sintef as a MIG-welding process where the filler alloy is melted together with the base alloy with the following parameters:

Table 5.4 – Welding parameters performed in this study.

Cylinder	Shielding gas	Filler alloy	Current [A]	Arc voltage [V]	Velocity [mm/s]
6060-T6 D=127 mm, t=1.8 mm	Argon	5183, 1.2 mm	70-72	19-20	12
6060-T6 D=100 mm, t=4.8 mm	Argon	5183, 1.2 mm	118-120	23-24	6
6082-T6 D=100 mm, t=4.8 mm	Argon	5183, 1.2 mm	118-120	23-24	6

Hardness tests will not be performed in this study, and therefore data from previous studies will be used. The Voce rule from section 2.2 is used to fit the true stress strain curve, and from Wang (2006) the true stress strain curve for the weld and HAZ performed as a MIG welding process for both butt and fillet welds are shown for aluminium alloy 6082-T6 in figure 5.15, where the base material from tensile test is plotted as well. These welds are made with a current of 236 amps, which is twice the current done in this study. Due to more heat,

the HAZ from Wang (2006) is larger than the HAZ in this study. Hardness tests conducted in HAZ in this study are required in order to investigate this accurately. The hardening parameters for Voce rule from Wang (2006) are given in appendix E. To establish the hardening parameters in the HAZ for alloy 6060-T6, Vickers hardness parameter will be used. Alisibramulisi (2010) gives a relation between the Vickers hardness and the yield and tensile strength for aluminium alloy 6060-T6

$$f_{0.2}[MPa] = 3.0 * HV - 48.1 \quad [5.5a]$$

$$f_u[MPa] = 2.6 * HV + 39.8 \quad [5.5b]$$

Figure 5.14 shows the Vickers hardness parameter in the HAZ region for a natural aged MIG weld in alloy 6060-T6 with the following welding parameters applied: Current: 145A, Voltage: 15.8V, and welding speed 16 mm/s, Alisibramulisi (2010). The current is almost twice the current applied on alloy 6060-T6, D=127 mm, t=1.8 mm, so to investigate this accurately, hardness test should be performed for the welds in this study. The investigation will go on using the given data from previous studies.

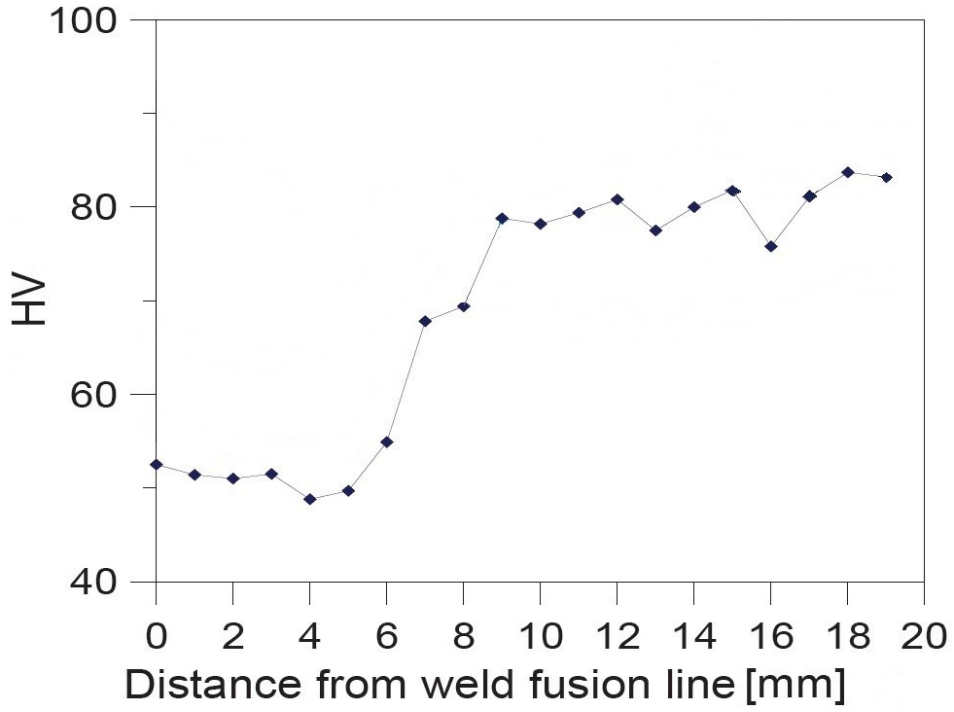

Figure 5.14 – Vickers hardness in HAZ for 6060-T6, natural aged. Alisibramulisi (2010).

For the heat treatable alloy 6060-T6 its possible to mitigate the effects of HAZ softening by means of artificial ageing applied after welding, as stated in EC9 (2007). Hardness tests conducted in the study by Alisibramulisi (2010) shows that for some ageing methods, the Vickers hardness is almost the same for HAZ and the base material. No artificial ageing methods are applied in this study.

A method to find the hardening parameters in the HAZ for alloy 6060-T6 is to multiply the hardening parameters in Voce rule with the relative tensile strength, ψ

$$\psi = \frac{f_{Vickers\ test}}{f_{Tensile\ test}} \quad [5.6]$$

The yield and ultimate tensile strength are taken from table 5.2. The yield stress is multiplied by $\psi_{0.2}$, $\sigma_0 + \sum Q_i$ is multiplied by ψ_u and the hardening parameters C_i is left unchanged.

Table 5.5 – Relative tensile strength for alloy 6060-T6, D=100 mm, t=4.8 mm.

Zone	HV [kg/mm^2]	$f_{0.2,Vickers}$ [MPa]	$f_{u,Vickers}$ [MPa]	$\psi_{0.2}$	ψ_u
Weld	52	108	175	0.58	0.65
2 mm away	51	105	172	0.56	0.64
4 mm	48	96	165	0.52	0.61
6 mm	51	105	172	0.56	0.64
8 mm	70	162	222	0.87	0.82
10 mm	76	180	237	0.97	0.88
Base material	78	186	271	1	1

Table 5.6 – Relative tensile strength for alloy 6060-T6, D=127 mm, t=1.8 mm.

Zone	HV [kg/mm^2]	$f_{0.2,Vickers}$ [MPa]	$f_{u,Vickers}$ [MPa]	$\psi_{0.2}$	ψ_u
Weld	52	108	175	0.58	0.65
2 mm away	51	105	172	0.56	0.64
4 mm	48	96	165	0.52	0.61
6 mm	51	105	172	0.56	0.64
8 mm	70	162	222	0.87	0.82
10 mm	76	180	237	0.97	0.88
Base material	80	191	260	1	1

The hardening parameters in the HAZ for Voce rule are given in Appendix E. It should be noted that there are many uncertainties related to the chosen procedure in parameter identification, so for exact results, hardness tests should be performed in further studies.

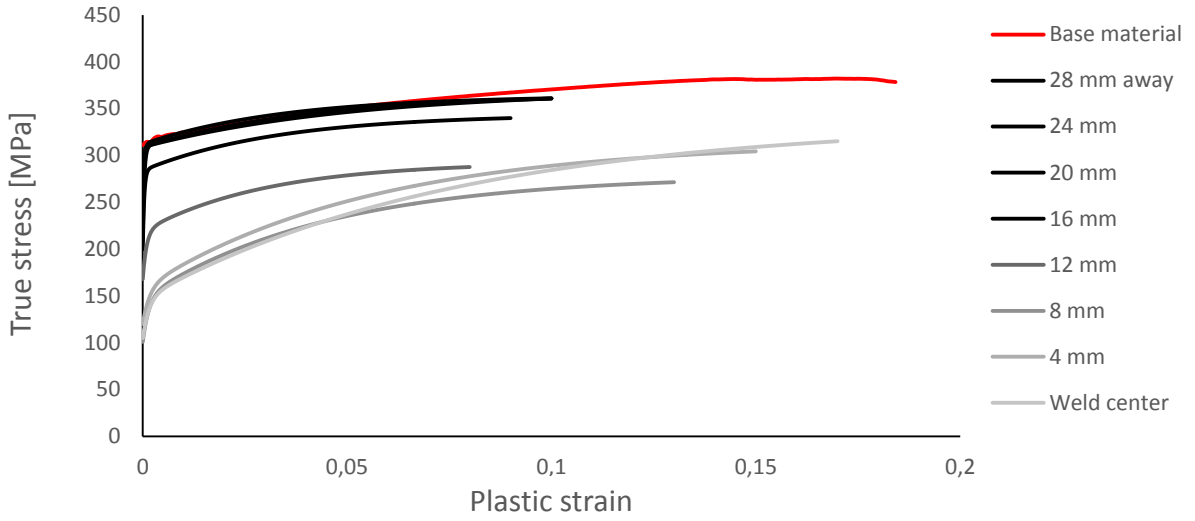

Figure 5.15 – Strength reduction in the HAZ for alloy 6082-T6, D=100 mm, t=4.8 mm.

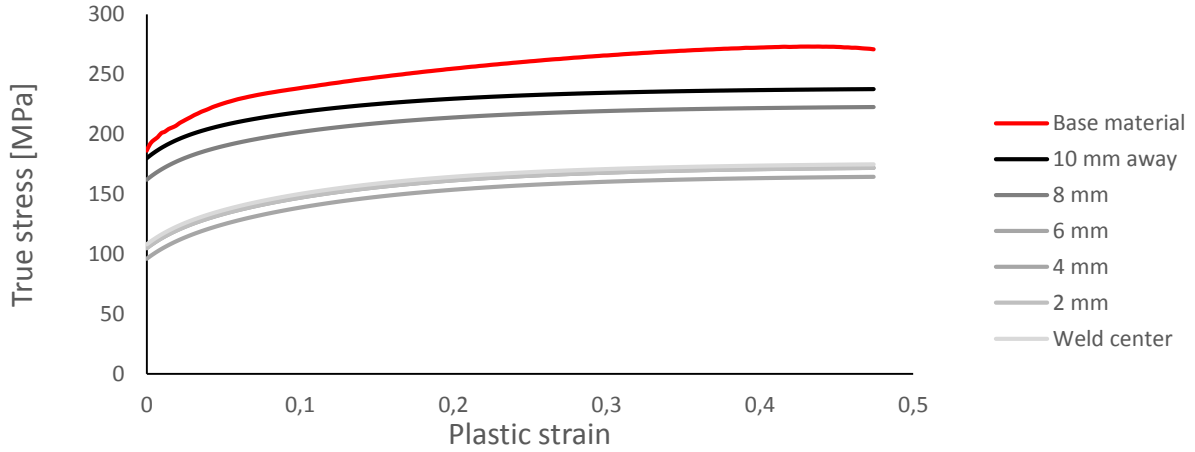

Figure 5.16 – Strength reduction in the HAZ for alloy 6060-T6, D=100 mm, t=4.8 mm.

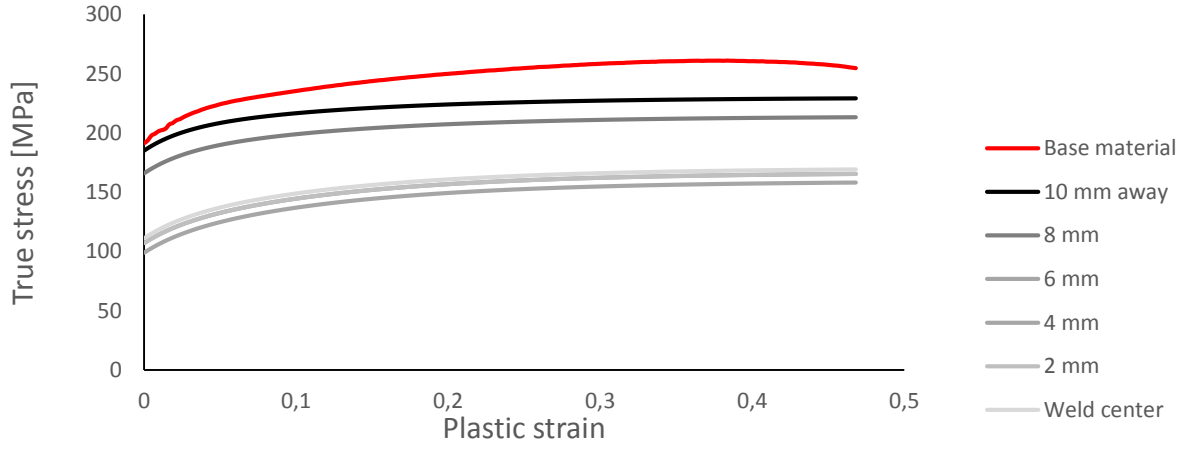

Figure 5.17 – Strength reduction in the HAZ for alloy 6060-T6, D=127 mm, t=1.8 mm.

The reduction factor, $\rho_{o,haz}$ for welding is found from equation [4.6], and is found in EC9 to be 0.43 and 0.48 for alloy 6060-T6 and 6082-T6, respectively. By use of the values found from Vickers hardness tests at weld center and the 0.2% permanent strain, the correct reduction factors yields:

Table 5.7 – Reduction factor, $\rho_{o,haz}$ due to welding for both EC9 and material tests.

	From material,- and Vickers hardness tests $\rho_{o,haz} = \frac{f_{o,haz}}{f_o}$	From EC9 $\rho_{o,haz} = \frac{f_{o,haz}}{f_o}$
6060-T6, D=100 mm, t=4.8 mm	$\frac{110.27}{192.23} = 0.57$	0.43
6060-T6, D=127 mm, t=1.8 mm	$\frac{112.99}{193.63} = 0.58$	0.43
6082-T6, D=100 mm, t=4.8 mm	$\frac{140.54}{314.56} = 0.45$	0.48

6 Numerical Analysis

6.1 Stub Tests without Welds

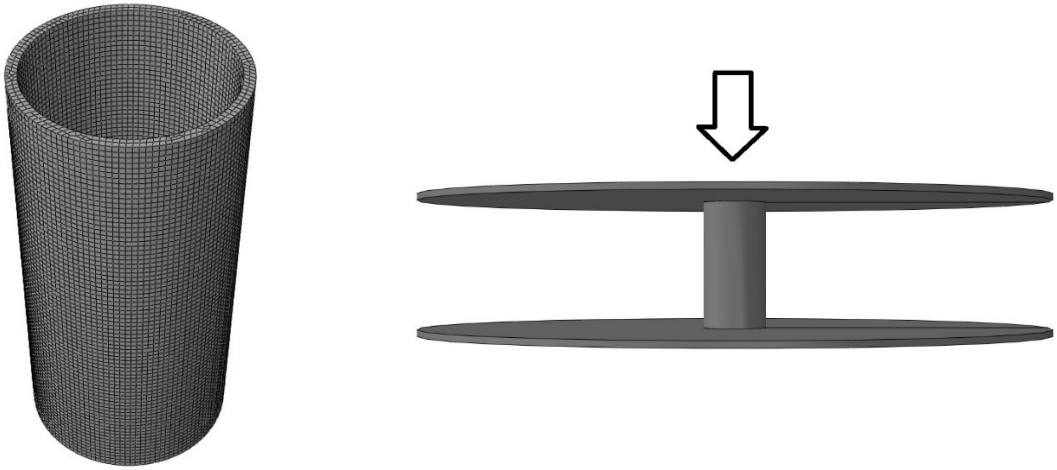

a) b)

Figure 6.1 – a) Alloy 6060-T6, D=100 mm, t=4.8 mm, L=2D with volume elements and meshsize ≈ 2.5 mm, and b) two analytical rigid plates compressing a deformable solid part.

Figure 6.1a) and b) shows the finite element design of the numerical analysis in Abaqus. Two analytical rigid plates compressing a deformable solid part by dynamic explicit analysis. The solid part has approximately one and two C3D8R linear volume elements over the thickness for cylinder D=127 mm and D=100 mm, respectively. To ensure local buckling, stub column tests are permformed both numerical and by laboratory experiments. Its decided to do some numerical analysis first to somehow know the required lengths needed to make the stub columns buckle locally, i.e. no movement of the longitudinal axis. Because the lengths are decided before the laboratory experiments, based on numerical analysis, the laboratory experiments will hopefully only be performed once. In experiments, stubs will just be put between two plates and compressed together. Thats because its cheap and easy to design in a FEA. But there is only one problem by this performance, and that is the boundary conditions. Will the effect of friction be a problem and trigger the local buckling or can it be analysed as frictionless? The friction between steel and aluminium is known, but it can be of interest to establish the different results. Figure 6.2 illustrates a stub column test when friction is zero. Then the column can move in radial direction without trigger the local buckling effect, so the question is will the degree of friction have any effects on the critical buckling load?

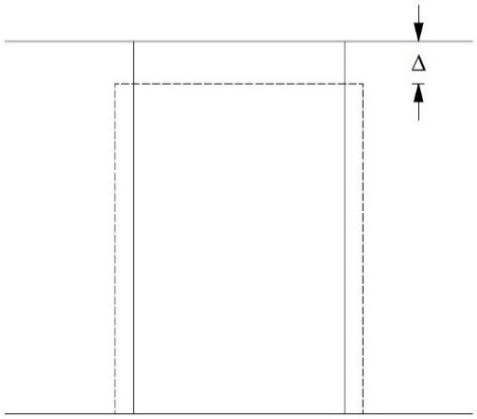

Figure 6.2 – Stub column test with zero friction.

Numerical analysis performed as dynamic explicit shows in figure 6.3 that the critical buckling load is constant for friction coefficients, μ_f in the range 0.1 to 2.0. Steel to aluminium has normally a friction coefficient equal to 0.6, and therefore friction is not a problem in this study. However, by running an analysis with $\mu_f = 0.01$, a slightly increase in critical buckling load is observed, most likely due to the free movement in the circumferential direction. Its assumed that the two other cylinders tested in this study are unaffected by friction coefficients as well.

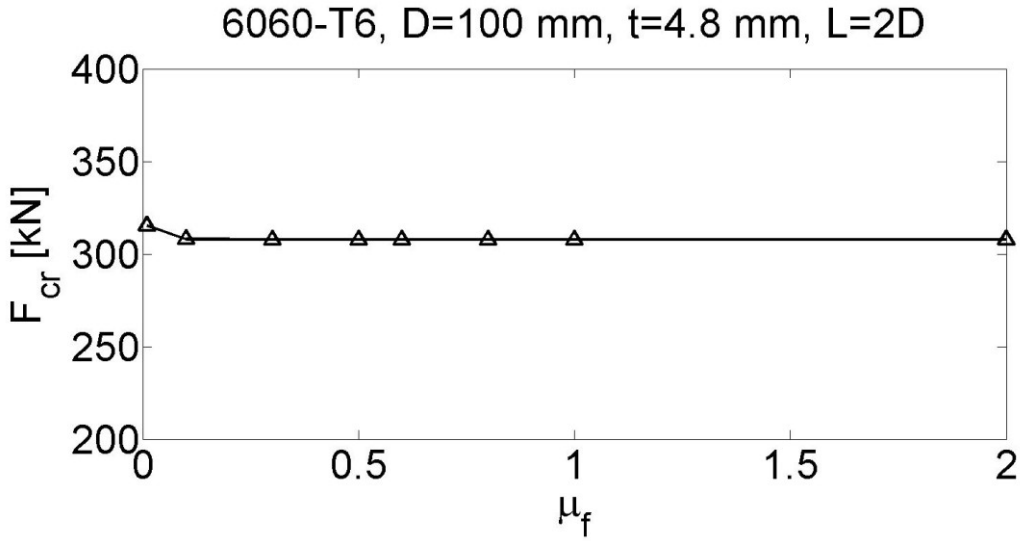

Figure 6.3 – Critical buckling load versus friction coefficients.

The lengths are decided from numerical analysis of aluminium alloy 6060-T6 when the diameter is perfect circular and values given from the factory as D=127 mm and t=1.8 mm. Dynamic explicit analysis are used and figure 6.4 shows that the critical buckling stress is the same for lengths every 50 mm in the domain ranging from L=50 mm to L=500 mm. Therefore, its decided that two different lengths will be tested in the laboratory for each of the

three combinations of stub columns. The lengths are two and four times the diameter. It should be noted that the critical buckling load have been filtered by a Butterworth filter embedded in the numerical analysis with a cutoff frequency as 100 kHz so that the high frequency oscillations can be omitted.

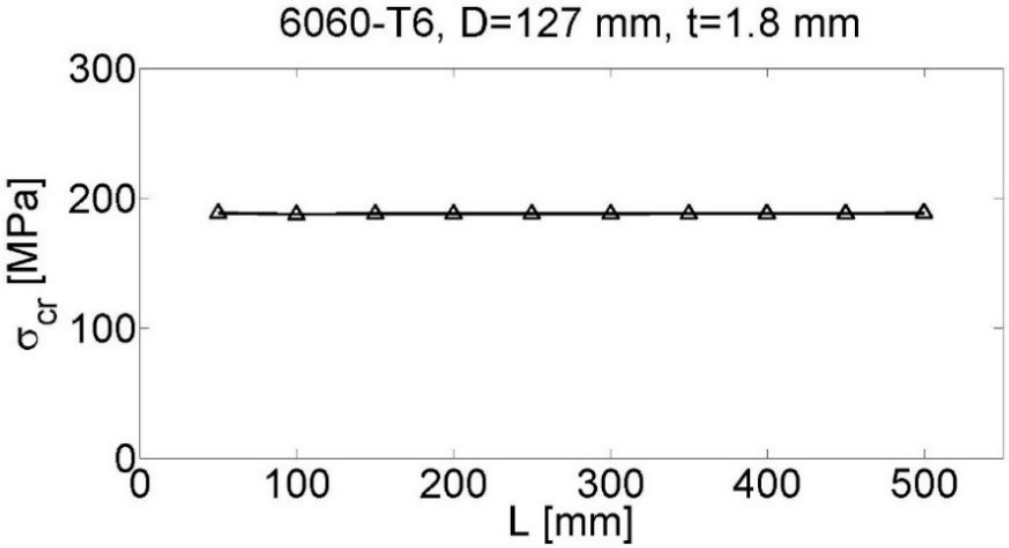

Figure 6.4 – Critical buckling stress for unwelded stub column.

For numerical analysis compared to the laboratory experiments, exact geometry, diameter and thickness are measured and the mean values used in the analysis are given in Appendix H.

6.2 Stub Tests with Welds

Stub tests are performed with two welds symmetrical on each side to investigate if the welds gives lower critical buckling load or different buckling mode than without welds. The numerical analysis are designed with changing sections around the welds when material parameters are taken from section 5.3. The welds itself are not in the numerical design because they are so small and any stiffener effects from the welds are therefore assumed negligable. When welding is performed, the heat is expanding like a sphere, but the half circle at the start and end of the weld is neglected in this numerical analysis. The lengths of the welds and their positions are measured in the lab with a classical caliper for each of the three tests and the mean lengths are used in the numerical analysis. Because of welding, some residual stresses will be applied in the middle of the cylinders, but these are not taken into account in this analysis, but should be further investigated for accurate results.

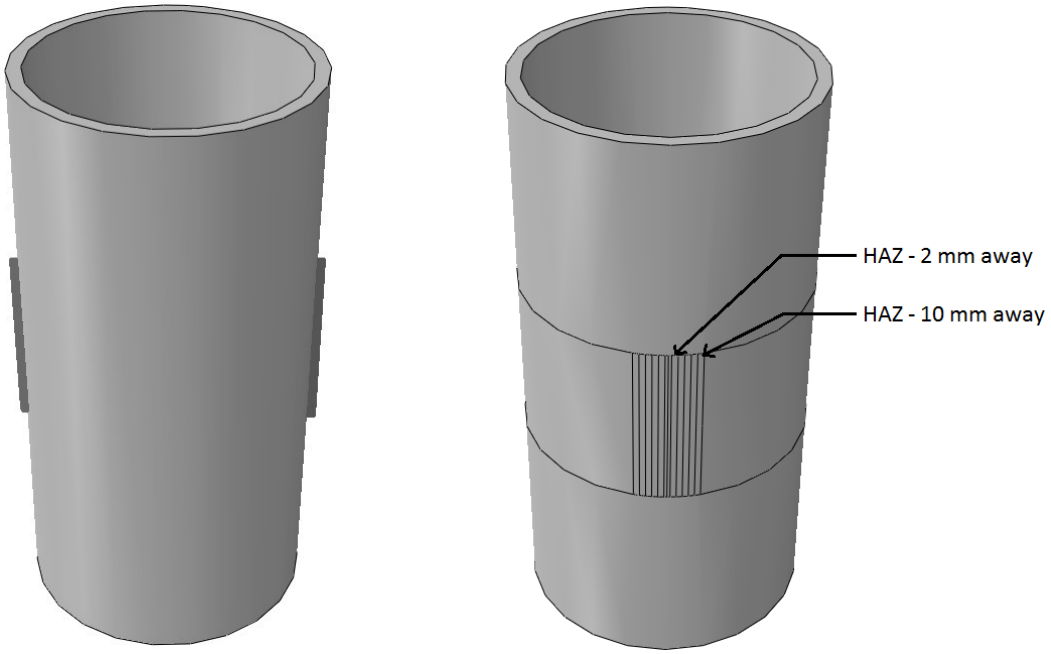

a) b)

Figure 6.5 – Numerical analysis of stub test with a) symmetrical welds and b) HAZ for alloy 6060-T6, D=100 mm, t=4.8 mm, L=2D.

Figure 6.6 – A weld on alloy 6060-T6, D=100 mm, t=4.8 mm. The length of the weld is D/2.

Exact geometry (posistions, length and width) for every welds are measured by a caliper and the mean values for the six different tests (two lengths and three cylinders) are used in the numerical analysis.

6.3 Long Cylinders. 1st Choice of Design

This design was first chosen to be used as a pin connection, but when it was investigated by FEA some problems occurred. Firstly, Abaqus would not allow making multiple rigid parts touch each other, so this became a connection problem where one of the sphere parts had to be a deformable part. This made the analysis a time-consuming problem. Second, the degree of friction between the spheres proved to be very sensitive when it came to critical buckling load. In total, this design was ment to be an easy pinned connection in all directions, but turned out to be a problem when it came to numerical analysis. It should also be noted that the rotation center for the pinned connection lays in the cylinder as described in figure 6.7b).

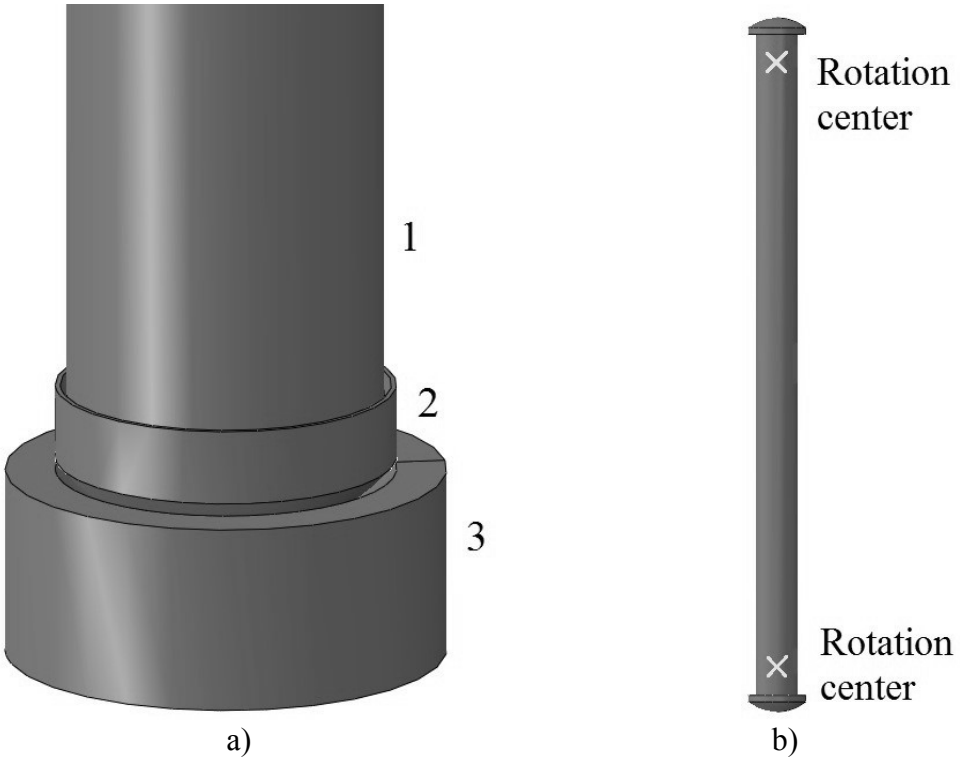

Figure 6.7 – a) Two half-spheres (part 2 and 3) making a pin-connection in all directions. b) Rotation center within the longitudinal axis of a column.

6.4 Long Cylinders. 2nd Choice of Design

Due to many uncertanties with the previous design, it was desided that a new and simplier design should be used. For simplicity, the buckling degrees of freedom (DOF) was limited to only one direction, making it easy to hinge the column in each end as shown in figure 6.8. By this design, the rotation center lays almost at the end of the column and the friction problem

disappear which makes it easy to design in a FEA where the column is the only part needed and the numerical analysis would expect to give approximately perfect results.

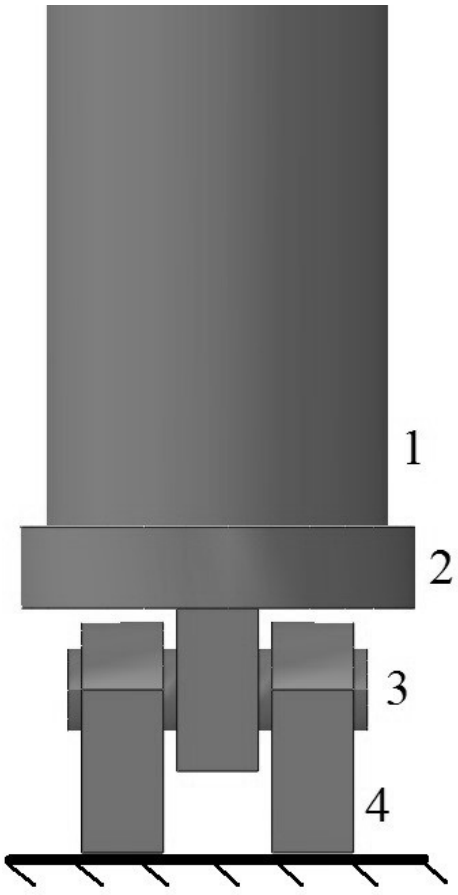

Figure 6.8 – Hinged connection at each end of a column with rollerbearings making the friction problem vanish.

In this master thesis, the rig is not build in the laboratory yet, so no laboratory experiments will be performed with this design. Some FEA however, are performed to validate the design when the rotation center is at the column ends. Visualizing results are given in figure 6.9 for alloy 6060-T6, D=127 mm, t=1.8 mm and L=2 m when a 4-node doubly curved S4R shell element has been used and dynamic explicit analysis is applied.

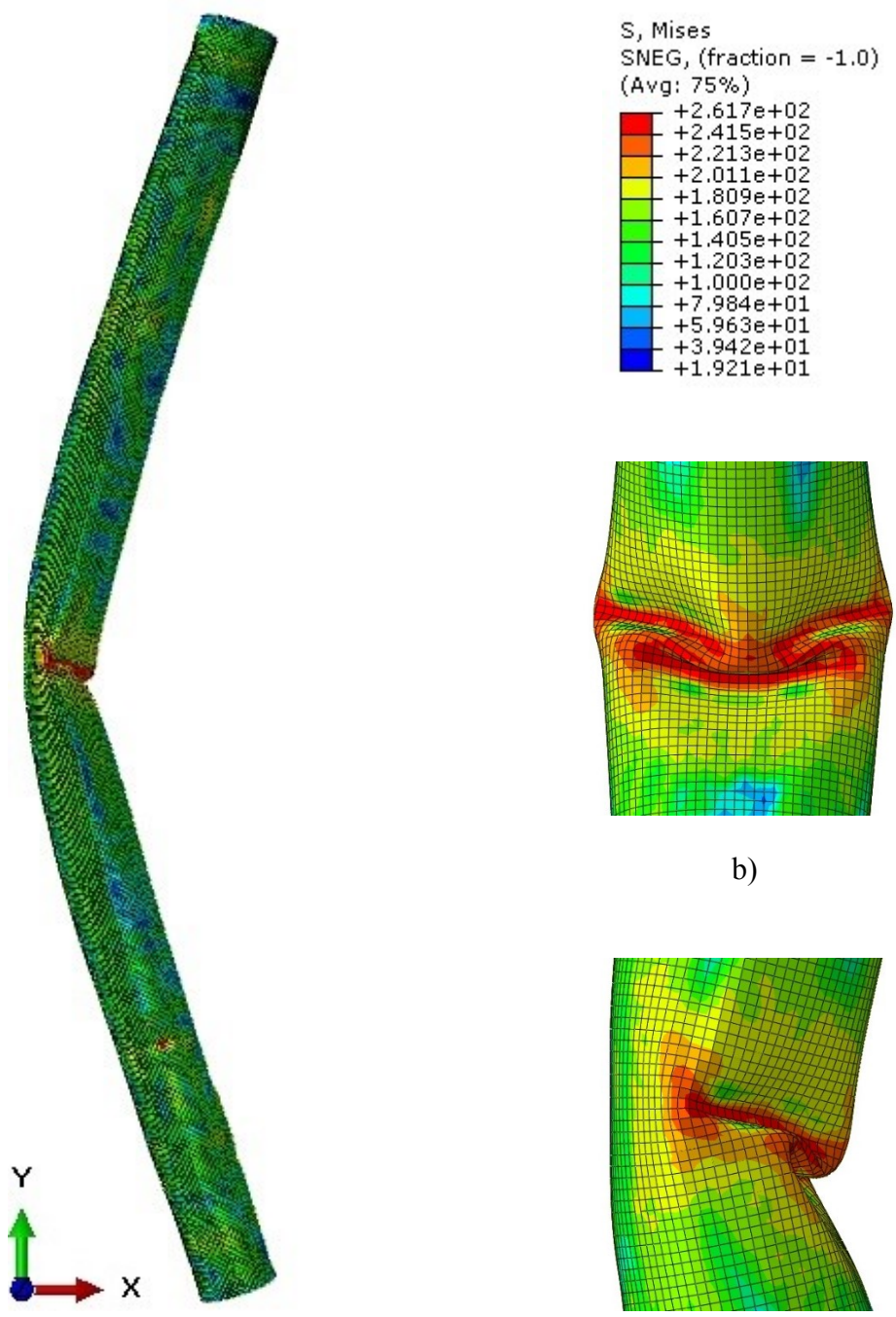

Figure 6.9 – Visualizing results for alloy 6060-T6, D=127 mm, t=1.8 mm, L=2 m when S4R shell elements are applied by a dynamic explicit analysis. a) represents the cylinder as pin-connected and b) and c) shows detailed buckling mode in the middle of the column, in y-z and y-x plane, respectively.

7 Laboratory Experiments

7.1 Unwelded Stub Column Tests

Two lengths for each of the three cylinder combinations are performed, and three tests for all cylinders, in total 18 stub tests are compressed between two rigid plates. Appendix D lists the combinations and all the tests. All stub tests were performed using Dartec 500 kN testing machine with displacement controll and a velocity of 0.1-0.5 mm/s. The displacement was measured using a laser, Micro-Epsilon optoNCDT. The rigid plates are made out of steel and are completely flat. The results from the stub tests are given in Appendix G.

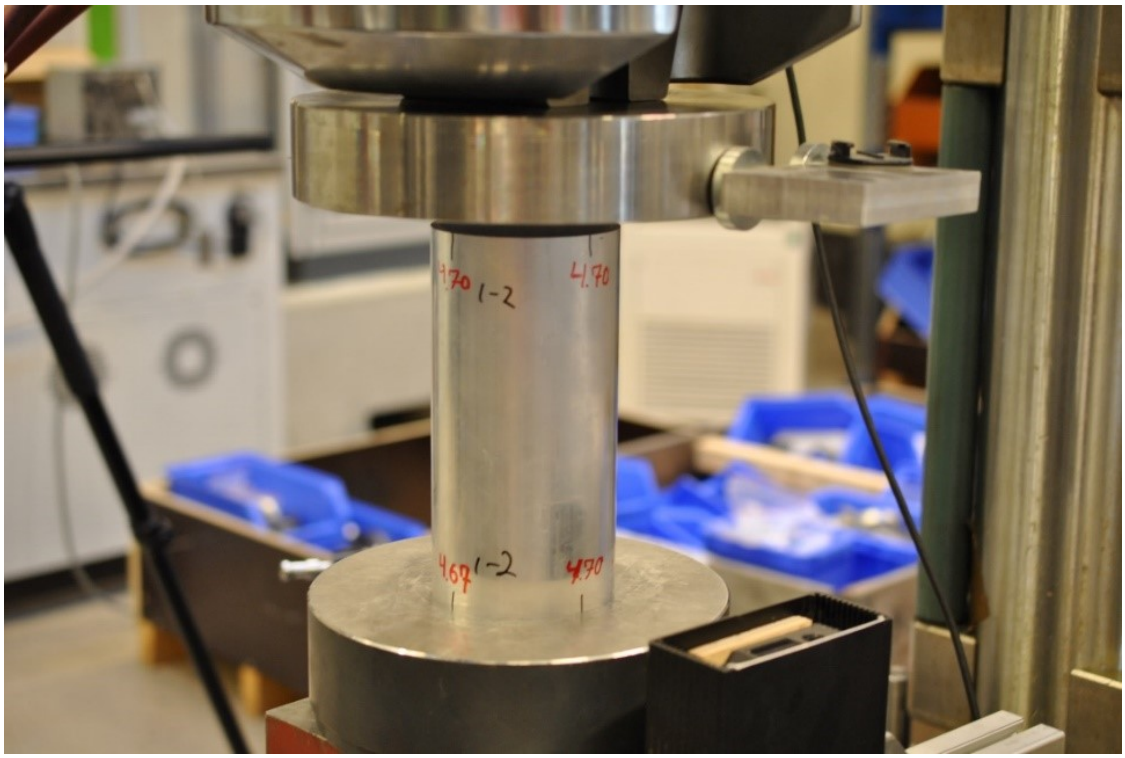

Figure 7.1 – Compression test in Dartec 500kN.

7.1.1 Results

Figure 7.2 – Results from compression tests of unwelded cross sections.

7.2 Welded Stub Column Tests

When welding is applied on a cylinder the geometry is expected to change due to heat contractions around the welds. Any thickness reductions in the cylinders are neglected because the uncertainty in the measuring device is propably larger than the thickness reduction, and most likely is the thickness only reduced around the welds where the material parameters are the dominating factors anyway. The diameter however, is expected to change. Either will the initial circular form become elliptic, force an elliptic form to be circular, or it will make an elliptic form even more elliptic. The welds are welded symmetrical on opposite sides, but not at the same positions relative to the measuring points in Appendix H. Figure 7.4 shows how the diameter changes for some cylinders before (black color) and after welding (red color). D1 and D2 is the diameter in the middle of each cylinder with 90 degrees between, see figure H.1. Its observed from figure 7.4 that when D1 decreases after welding, D2 increases, and opposite when D2 increases. Due to this observation, the welding process is neglected when it comes to geometry because the elliptic form only changes position and the form itself does not change. Due to welding, some residual stresses will be applied to the cylinders, but they are neglected in the numerical analysis. The cylinders tested are the same as in section 7.1 when it comes to material and geometry combinations. Appendix D lists the combinations and all the tests.

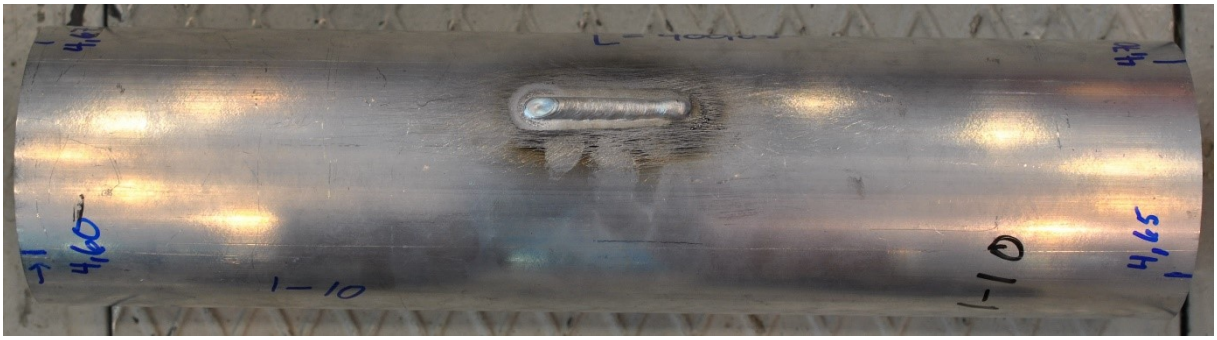

Figure 7.3 – Weld on surface for alloy 6082-T6, D=100 mm, t=4.8 mm. $L_w = D/2$.

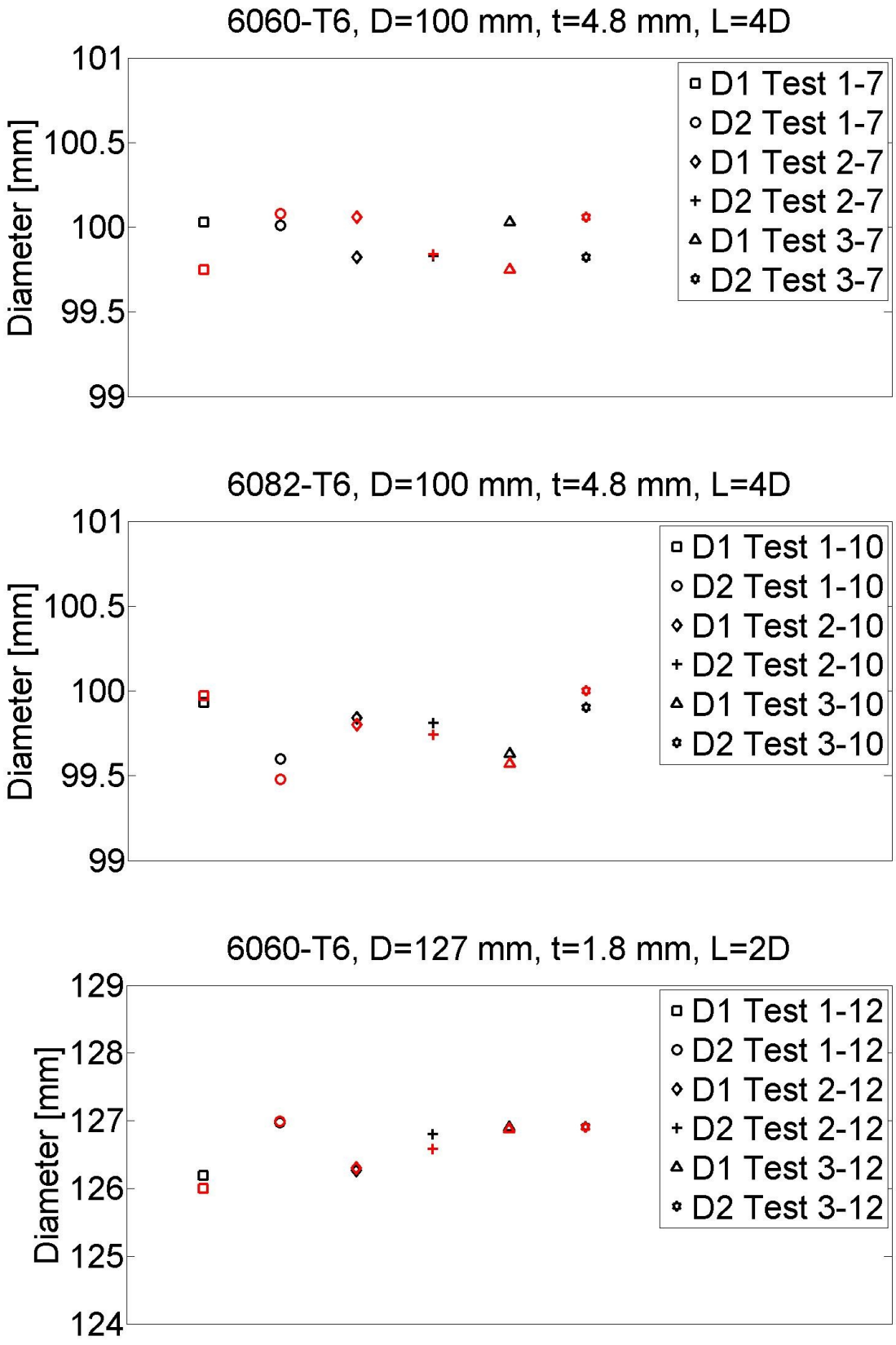

Figure 7.4 – Diameter before (black) and after (red) welding.

7.2.1 Results

Figure 7.5 – Results from compression tests of welded cross sections.

7.3 Buckling Test of Long Cylinders

7.3.1 Long cylinder. 2nd choice of design

For simplicity, pinned connection is used in this study. Pinned connection is easy to analyse and compare to analytical formulas. A problem with pinned connection is the degree of friction. First, a design with a half-sphere was investigated as shown in figure 6.7a. By performing some friction-sensitivity analysis with FEM as mentioned, the buckling load varied too much with varying friction coefficients between components 2 and 3. This became a problem as the friction on the half-sphere is not easy to determine. Besides, some lubricate should also be used and this would have made the friction a wild guess. Therefore, a another design is considered where the friction is not a problem as shown in figure 6.7b. Rollerbearings are used between the shaft and the two other components making this almost a frictionless design due to small steel spheres rolling inside the bearing, but also a very short distance from the rolling area into the center of the shaft, e.i. negligible torque on the shaft due to friction. Unfortunally, this design is only able to move in one direction, and since the global imperfection is unknown, but probably very small, a design to somehow controll its buckling direction is suggested. This design therefore becomes a bending-compression problem with a tiny force transverse in the middle of the column to ensure the buckling direction. The initial global imperfection is not known exactly, but the manufacturer has a tolerance limit they have to be within. So to make the columns buckle in the desirable direction, the force has to minimum be equal to the corresponding value from the imperfection limit from the manufacturer, i.e. the elastic deflection from a simply supported beam, taken into account that the imperfection in worst case scenario can be the opposite direction as the mid-force. This is better illustrated in figure 7.6.

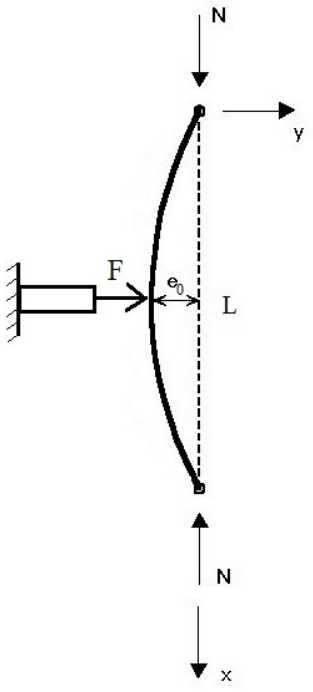

Figure 7.6 – Transversal force to ensure the buckling direction.

Figure 7.6 illustrates the worst case scenario when the global imperfection, e_0 is orientated in the opposite direction as the force applied. If the column was allowed to buckle in this direction it would destroy the component applying the force, F. This is also one of the reasons a bending-compression design is determined. Classical buckling theory, as shown in this master thesis, would buckle out in a sudden, out-of-controll behaviour if the initial imperfection is small or zero as shown in figure 8.1. So when full scale buckling tests on aluminium columns are performed in the laboratory it can be dangerous to be around when columns with small imperfection buckles. Therefore, a known force, or a corresponding deflection is applied in the middle with a good safety margin. By this, the bending effect will become more important and the sudden buckling effect will decrease. This is also taken into account in the numerical analysis, and some analytical derivations are done for bending-compression of columns. Further, some beams are put up in the rig for safety reasons so the columns will not shoot out.

When the rig in the laboratory will be designed, steel will be used as the favorable material in the components forming the pinned connections at the ends. When long aluminium columns are compressed, its assumed that its only the aluminium that yields, i.e. no deformations in the steel components. Therefore, the associated steel components, i.e. components 2 and 3 in figure 6.8, should absolutely not yield when the buckling load for the aluminium columns are reached. Figure 7.7 shows the load acting as a cantilever beam problem with length a on component 2. The little trace on the top of component 2 is to secure the column not to move during the experiments.

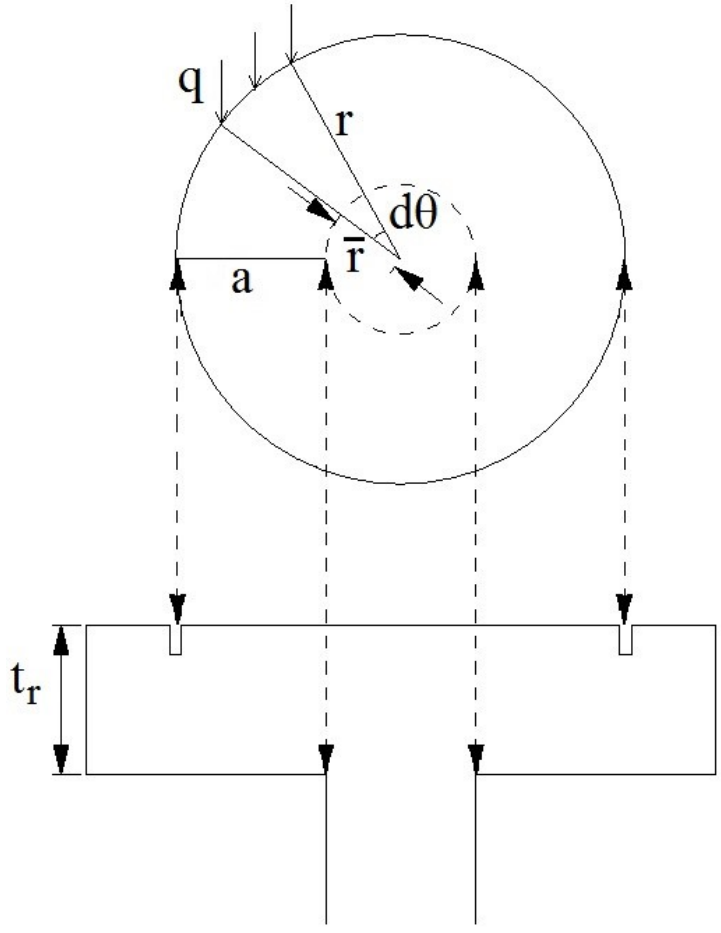

Figure 7.7 – Design of component 2 in the rig design for long columns.

The formula to determine the thickness, t_r and the length a for different cylinder geometries are given below, based on the geometry of figure 7.7. The maximum buckling load, N are found from buckling analysis with numerical tools. Then the rotation center lays at the center of each ends, and this is ok because its assumed that this design will be close to an ideal euler column. The maximum load will occur on the cylinder with D=100 mm and t=4.8 mm, material properties from aluminium alloy 6082-T6 and with short lengths, and the rig is therefore designed based on this buckling load. To be on the safe side that component 2 does not yield, σ will be set equal to half of its yield strength.

The moment acting in the attachment from the cantilever is the force from the cylinder wall times a

$$M = qd\theta r * a \qquad [7.1]$$

The elastic resisting moment is thus

$$\frac{1}{6}\bar{r}d\theta {t_r}^2 * \sigma \qquad [7.2]$$

Equilibrium gives

$$qd\theta ra = \frac{1}{6}\bar{r}d\theta {t_r}^2\sigma \qquad [7.3]$$

The force acting from the cylinder wall is $q = N/2\pi R$. Inserting this and solve for σ

$$\sigma = \frac{N}{\pi}3\frac{a}{\bar{r}{t_r}^2} \qquad [7.4]$$

From equation [7.4] component 2 in figure 6.8 can be designed to ensure no plastic deformation in the steel component and its further assumed in the numerical analysis that all these associated components can be made rigid, i.e. zero deformations. Since the steel components are made rigid in the numerical analysis and the rollerbearings ensure zero friction, its only interesting to establish the distance, d from the cylinder end to the rotation center, as shown in figure 7.8. Because then a simple design in the FEA can be used, i.e. one rigid part at each ends with a constrained referance point that the rigid part can rotate about at a distance d from the column ends. The design is restrained to rotate about two axes, so it can only rotate one way.

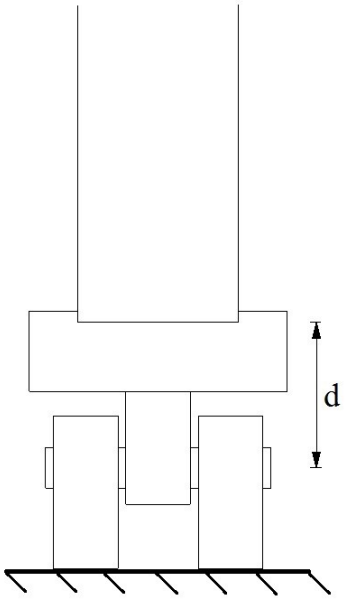

Figure 7.8 – Distance, d from column end to rotation center.

7.3.2 Measurement of long cylinders

When buckling tests shall be performed in the laboratory and compared with numerical analysis, its very important that the exact geometry of the column tested is known so that the numerical analysis is reliable. As shown in section 8, buckling is very sensitive for imperfection for long columns, but thickness variation should also be investigated. Therefore, manual measurement of thickness were performed by a ultrasound device on all three different cylinders with lengths of five meters. Four measurement data were logged at every points on the cylinders, and the average value was plotted as shown in figure 7.10. The thickness was measured on cylinders with lengths of five meters, and measurement points were taken every half meter. To get a suitable idea of how the thickness varies around the cylinders, four points were taken around the cross section as well. In total 480 measurements were performed.

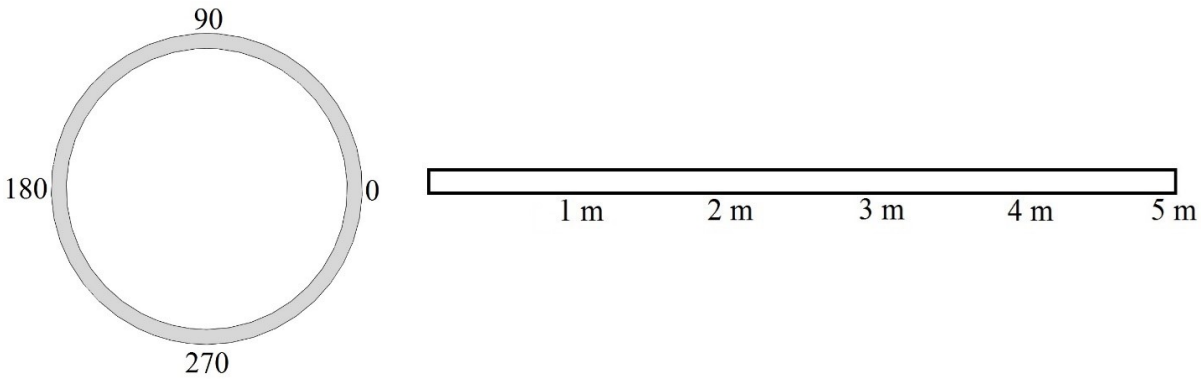

Figure 7.9 – Measurement points on the investigated cylinders.

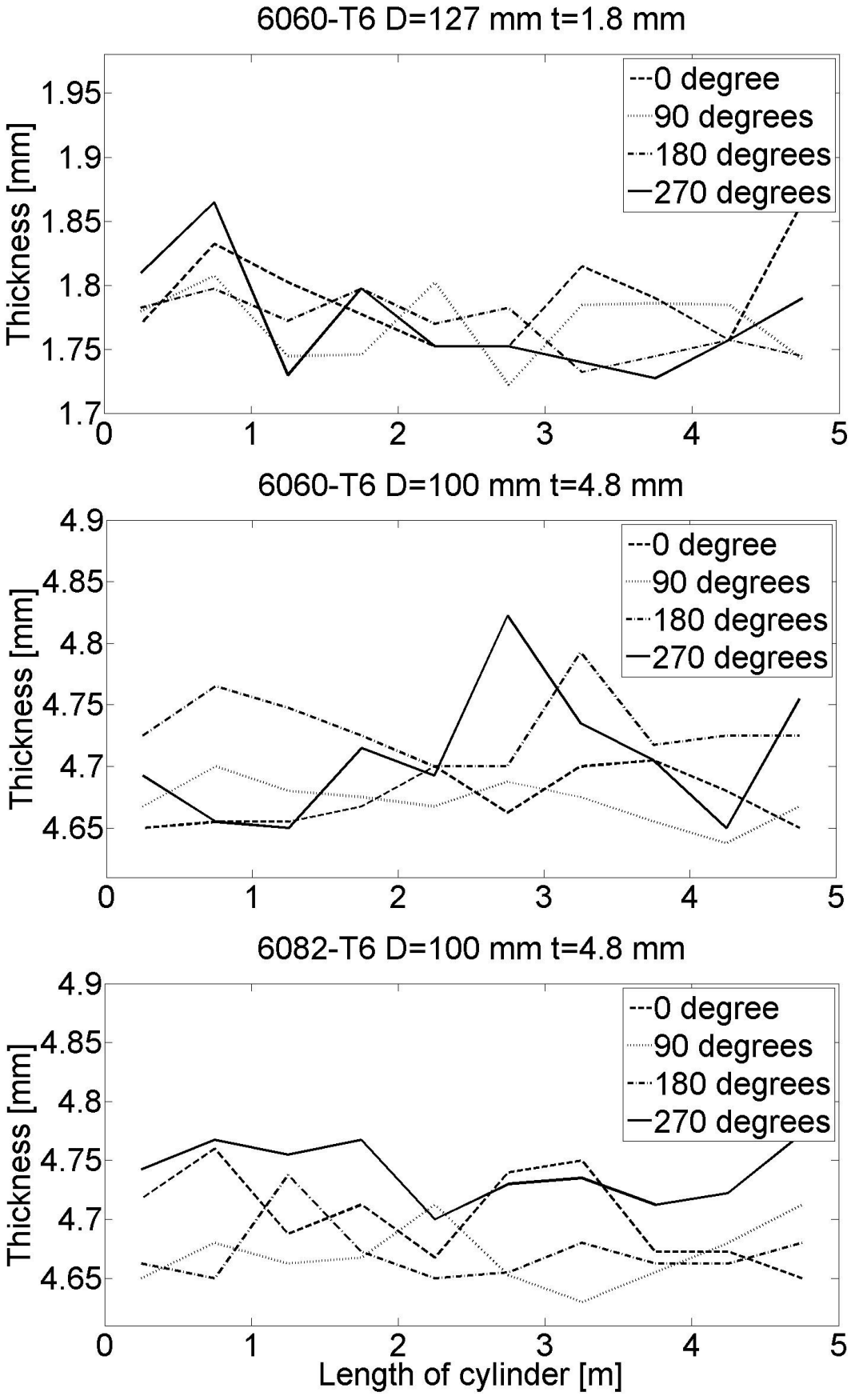

Figure 7.10 – Thickness variation for cylinders of five meters.

These measurements are taken from only three cylinders so it only shows that the thickness varies somewhat, and measurements have to be performed for every cylinders performed in a buckling test. As observed from figure 7.10 its not easy to determine the exact geometry when performing a numerical analysis. The thickness scatter is about 0.1 mm for all the cylinders, so analyses with the highest and lowest homogeneous thickness could be performed and the deviation could be considered, but since the cylinders are most likely non of these cases, a more interesting analysis could be investigated with different thickness distributions. Abaqus allows the thickness to follow an analytical expression, so a simple method is to make the thickness follow a sine curve with amplitude 0.05-0.1 mm in both the longitudinal and circumferential axis. Different amplitudes in the longitudinal and circumferential axis best fitted the measurement for each cylinders could be investigated, but maybe a more scientific method would be to distribute the thickness randomly with a given amplitude. This is suggested as further work when buckling test of long columns will be performed.

8 Imperfection

8.1 Analytical Formula

By plotting equation [3.45] for different initial imperfections for a given cylinder, the load capacity increases when the imperfection becomes smaller. The column can not go above equation [3.47], and by comparing the initial imperfection for $e_0 = 0.5$ mm and $e_0 = 3$ mm, for a column (D=127 mm, t=1.8 mm and $f_o = 140$ MPa) with length $L = 2.5$ m, the critical buckling load will decrease by 13.6%. This means that the critical buckling load is very sensitive for initial imperfections. Its therefore convenient to measure the exact imperfection of the columns.

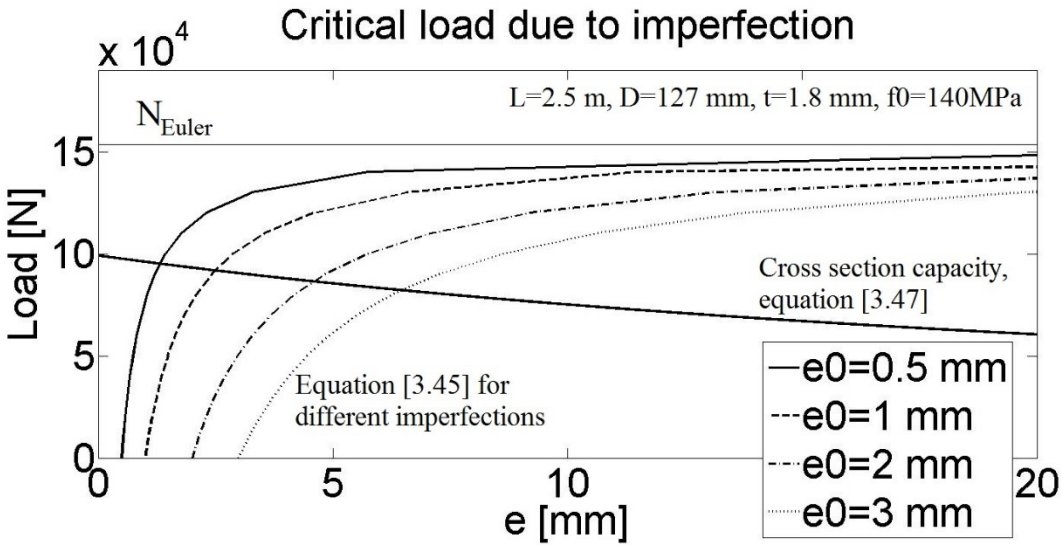

Figure 8.1 – Critical load due to imperfection and cross section capacity.

Equation [3.51] gives the intersection point for [3.45] and [3.47] and the relative load can be plotted against length of the same cylinder.

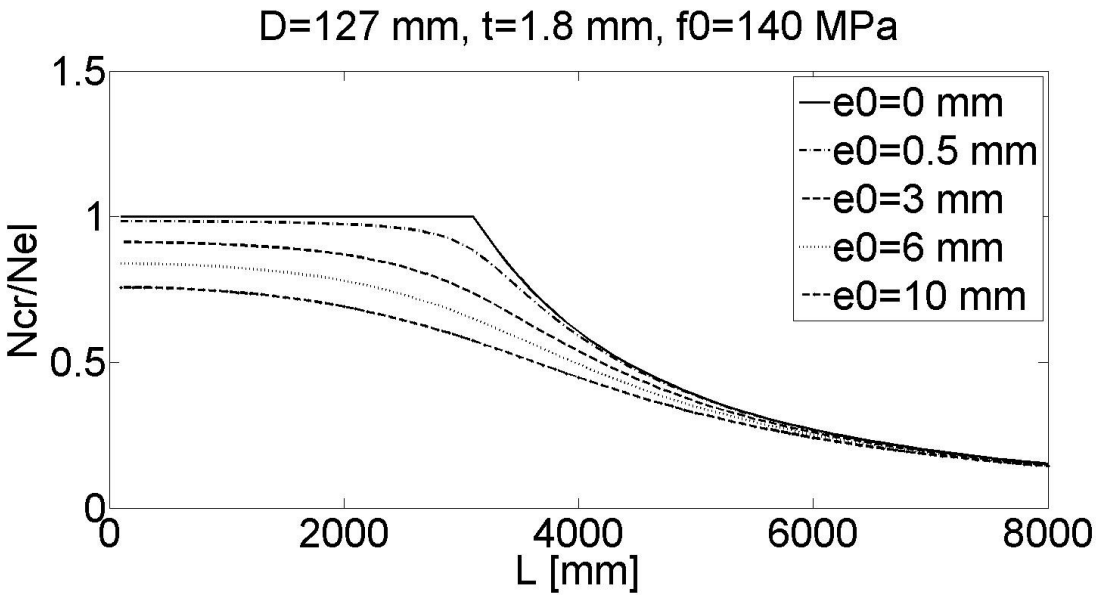

Figure 8.2 – Relative load for different initial imperfections following equation [3.51].

9 Results

9.1 Unwelded Stub Tests

The mean values from the three tests are used to find the experimental force versus displacement curve, and its compared with numerical results below. From section 7 and Appendix G its observed that the force displacement curve and the deformation modes are identical for lengths two and four times the diameter.

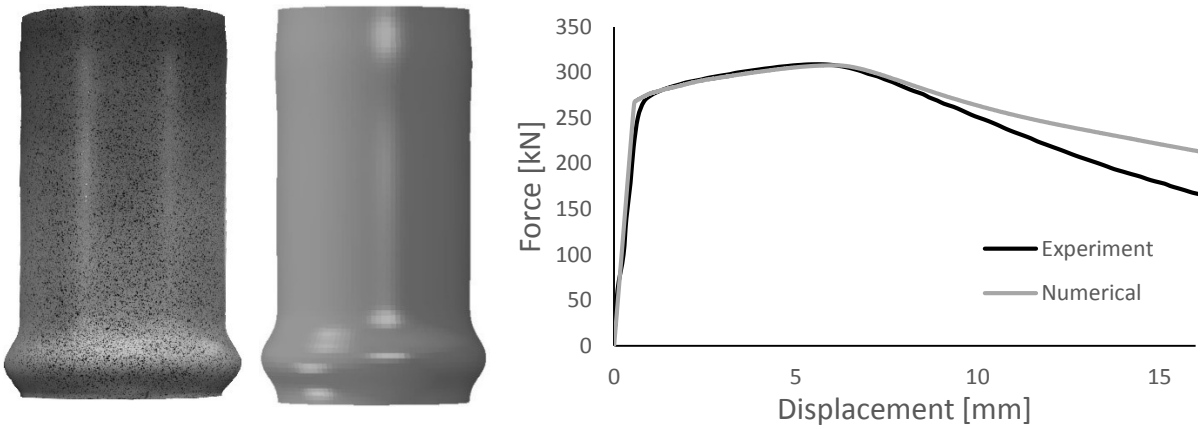

a) b) c)

Figure 9.1 – Buckling mode for a) experiment and b) numerical when displacement is 15 mm. c) Force displacement for both experiment and numerical for alloy 6060-T6, D=100 mm, t=4.8 mm, L=2D and meshsize ≈ 2.5 mm. Numerical result gives a critical buckling load 0.32% below result from the laboratory experiment.

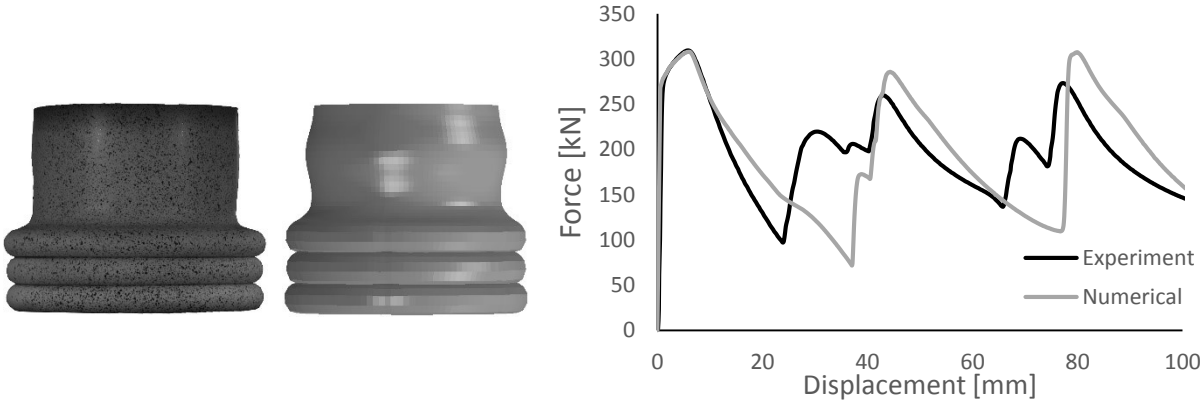

a) b) c)

Figure 9.2 – Buckling mode for a) experiment and b) numerical when displacement is 100 mm. c) Force displacement for both experiment and numerical for alloy 6060-T6, D=100 mm, t=4.8 mm, L=2D and meshsize ≈ 2.5 mm.

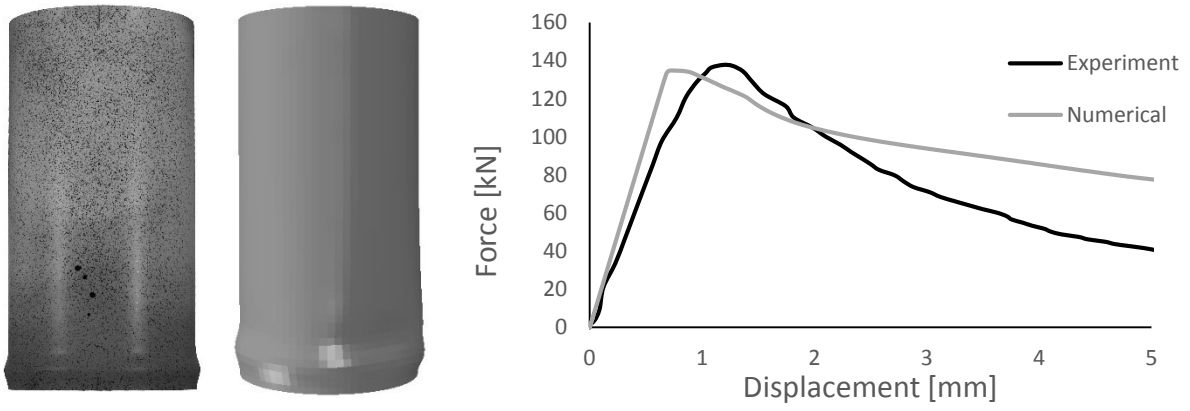

a) b) c)

Figure 9.3 – Buckling mode for a) experiment and b) numerical when displacement is 4 mm. c) Force displacement for both experiment and numerical for alloy 6060-T6, D=127 mm, t=1.8 mm, L=2D and meshsize ≈ 5 mm. Numerical result gives a critical buckling load 2.26% below result from the laboratory experiment.

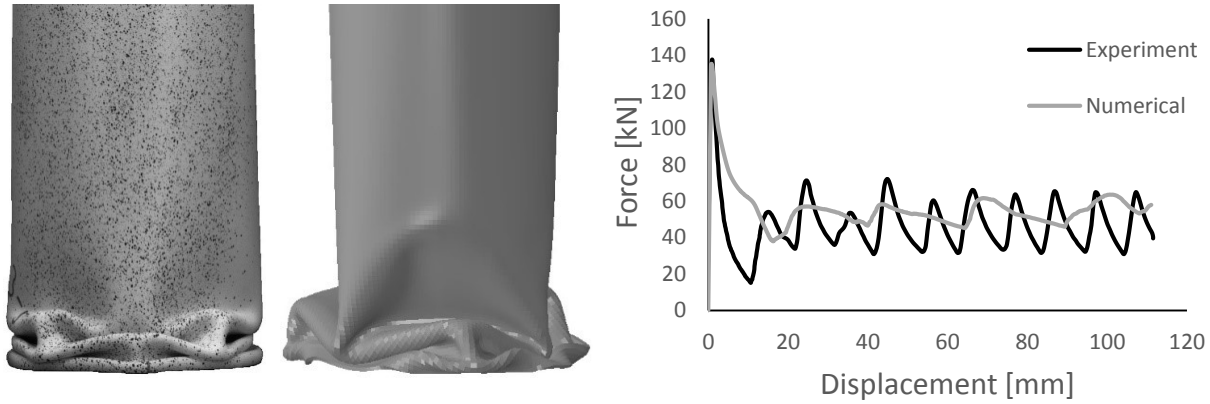

a) b) c)

Figure 9.4 – Buckling mode for a) experiment and b) numerical when displacement is 65 mm. c) Force displacement for both experiment and numerical for alloy 6060-T6, D=127 mm, t=1.8 mm, L=4D and meshsize ≈ 2.5 mm.

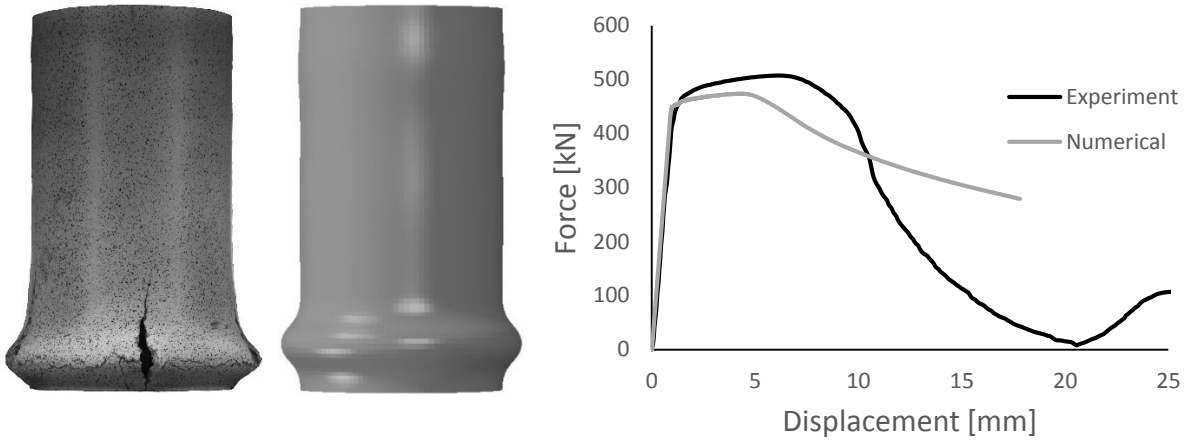

a) b) c)

Figure 9.5 – Buckling mode for a) experiment and b) numerical when displacement is 15 mm. c) Force displacement for both experiment and numerical for alloy 6082-T6, D=100 mm, t=4.8 mm, L=2D and meshsize ≈ 2.5 mm.

Due to cracks in aluminium alloy 6082-T6, the compression tests were stopped earlier than for alloy 6060-T6. Its observed from figure 9.5 that when alloy 6082-T6 cracks it has almost no force resistance. The numerical analysis does not take the cracks into consideration, and that may be a reason why the force displacement curve does not fit so well. The critical buckling force calculated from the numerical analysis lay 6.25% below critical buckling force from the laboratory experiment.

For the cylinders tested experimentally, the mean values for the three tests are used to calculate the critical buckling stress. Figure 9.6 shows only results for two lengths, 2 and 4 times the diameter, but its clearly that the critical buckling stress is the same for all lengths that buckles locally.

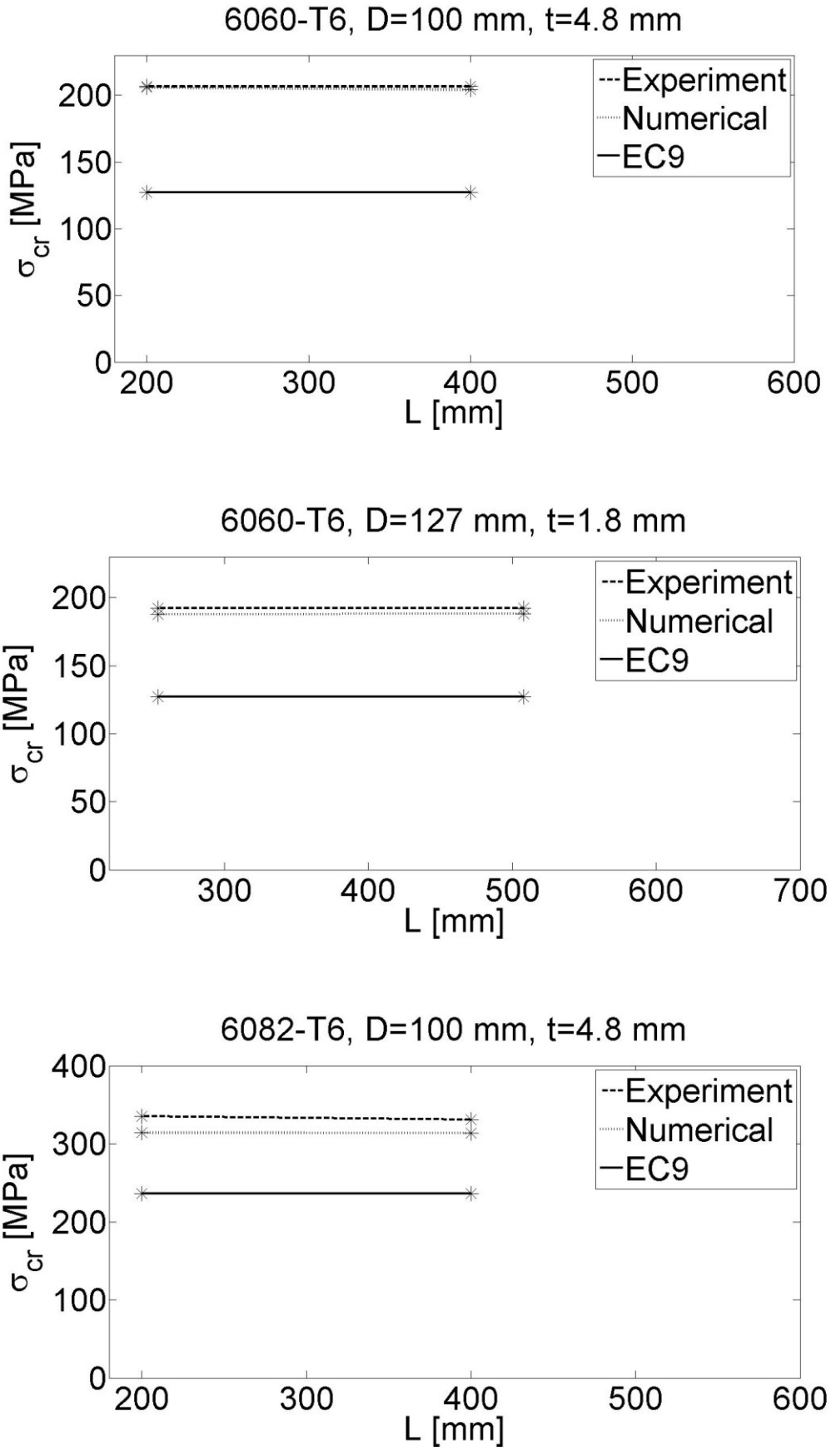

Figure 9.6 – Critical buckling stress for unwelded stub columns.

When EC9 calculations for length two times the diameter is compared with experimental results for unwelded cross sections, alloy 6060-T6, D=100 mm, t=4.8 mm is 38.4% below, alloy 6060-T6, D=127 mm, t=1.8 mm is 33.8% below and alloy 6082-T6, D=100 mm, t=4.8 mm is 29.5% below.

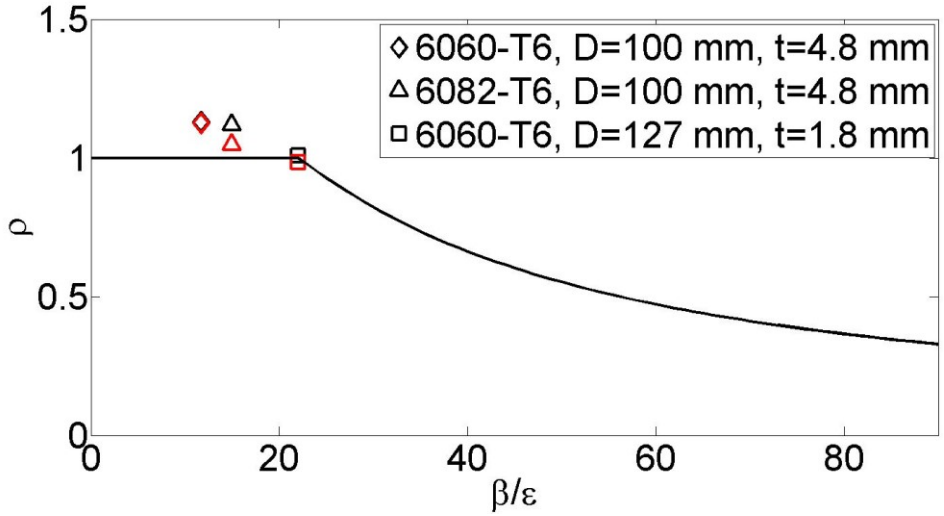

Figure 9.7 – Results from unwelded cross sections given as laboratory experiments (black points) and numerical results (red points) for L=2D. Calculations from EC9 represents the black line.

Figure 9.7 gives the relationship between ρ and β/ε for the three different tests performed in this study when the local buckling factor, ρ is given as σ_{cr}/f_o. The yield stress, f_o is taken as the corresponding 0.2% permanent strain found in EC9. When EC9 is used, the same local buckling factor is notated ρ_c and its used to factor down the thickness for cross section class 4 members. For unwelded cross sections, non of these cylinders are in class 4, but as shown in figure 9.7, alloy 6060-T6, D=127 mm and t=1.8 mm is very close. The β and ε factors are given in EC9 as $\beta = 3\sqrt{D/t}$ and $\varepsilon = \sqrt{250/f_o}$.

9.2 Welded Stub Tests

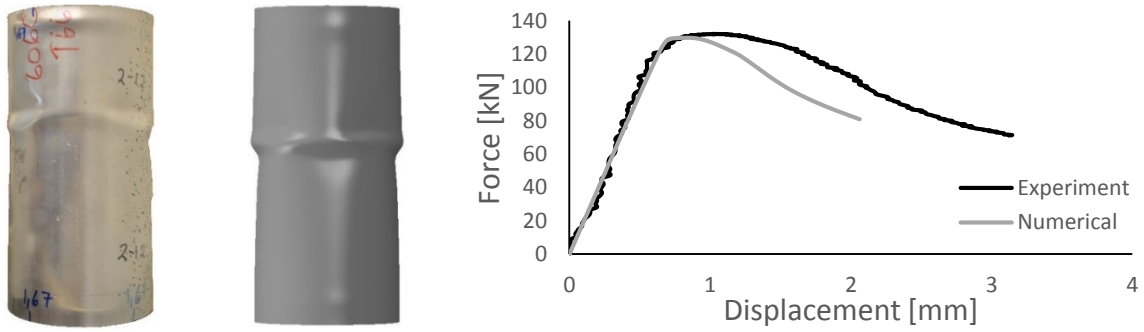

a) b) c)

Figure 9.8 – Buckling mode for a) experiment and b) numerical when displacement is 3 mm. c) Force displacement for both experiment and numerical for alloy 6060-T6, D=127 mm, t=1.8 mm, L=2D and meshsize ≈ 1 mm.

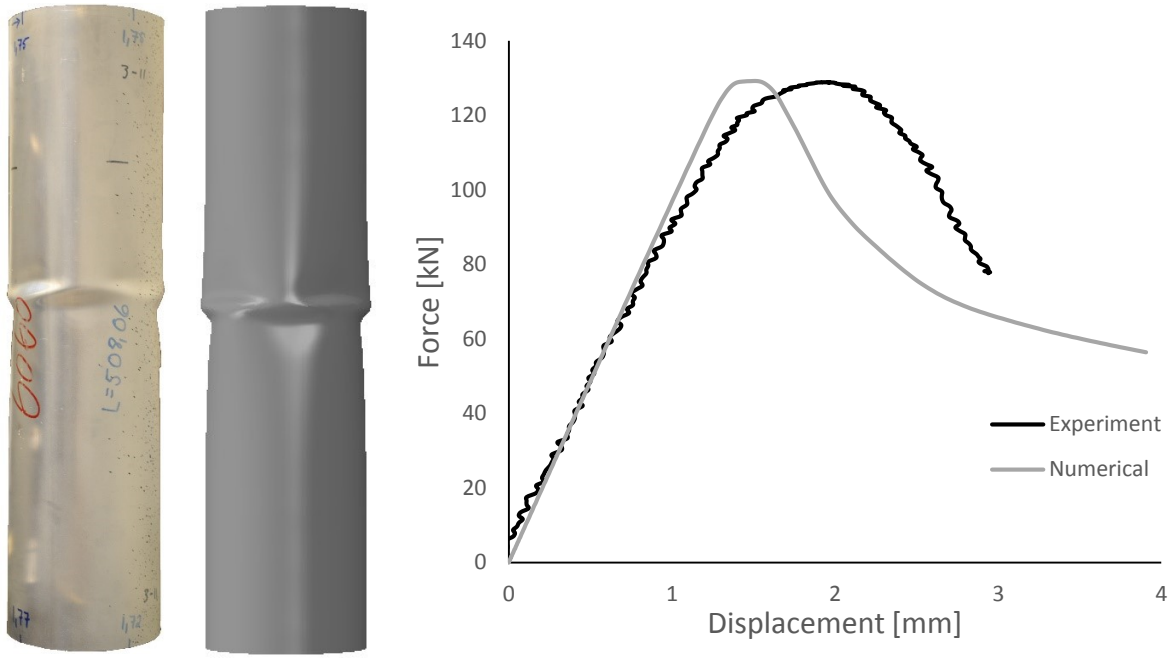

a) b) c)

Figure 9.9 – Buckling mode for a) experiment and b) numerical when displacement is 3 mm. c) Force displacement for both experiment and numerical for alloy 6060-T6, D=127 mm, t=1.8 mm, L=4D and meshsize ≈ 1 mm.

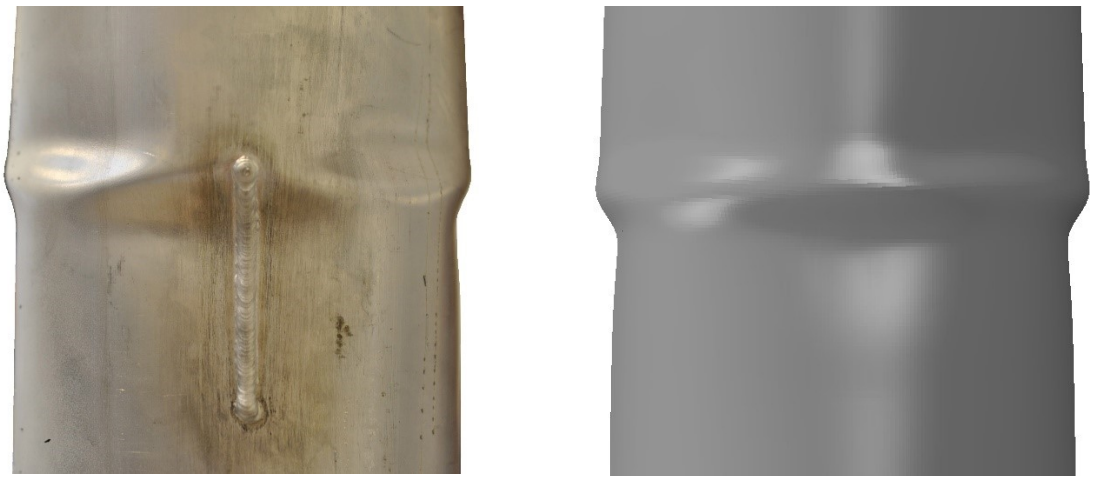

a) b)

Figure 9.10 - A section of the cylinder around the weld for both a) experiment and b) numerical, for alloy 6060-T6, D=127 mm, t=1.8 mm, L=4D and meshsize ≈ 1 mm.

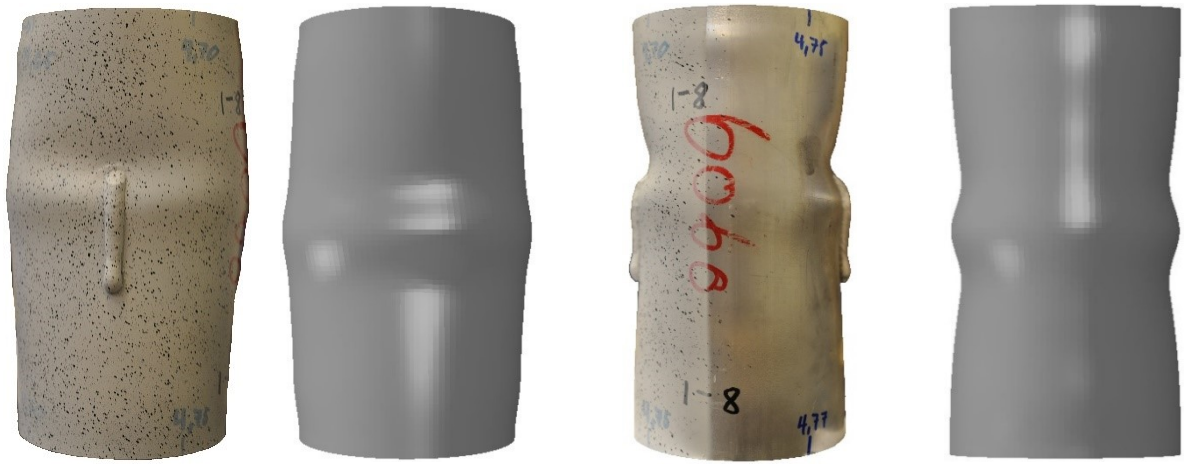

a) b) c) d)

Figure 9.11 – Buckling mode for a) & c) experiment and b) & d) numerical when displacement is 11 mm and the cylinders are oriented in the a) & b) y-z and c) & d) y-x plane for alloy 6060-T6, D=100 mm, t=4.8 mm and L=2D.

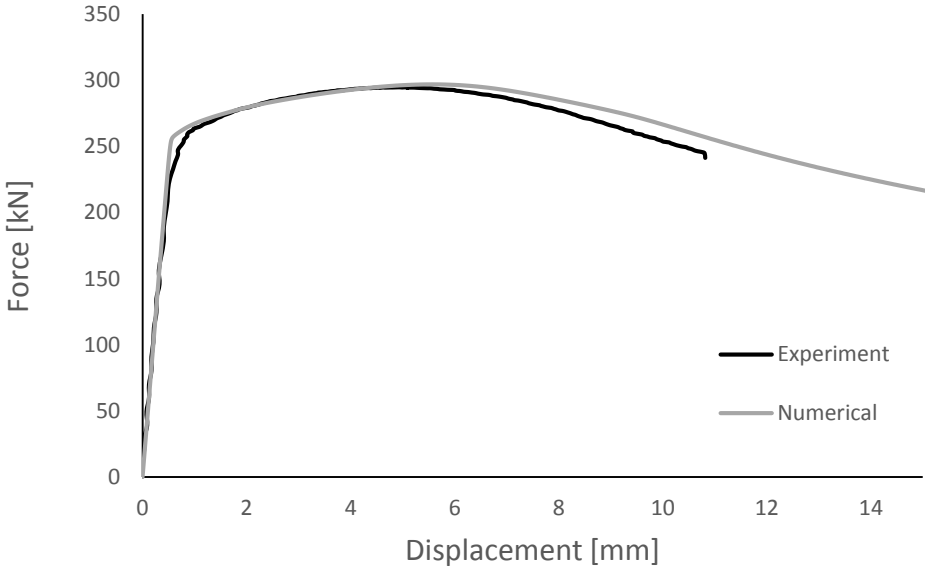

Figure 9.12 – Welded alloy 6060-T6, D=100 mm, t=4.8 mm and L=2D.

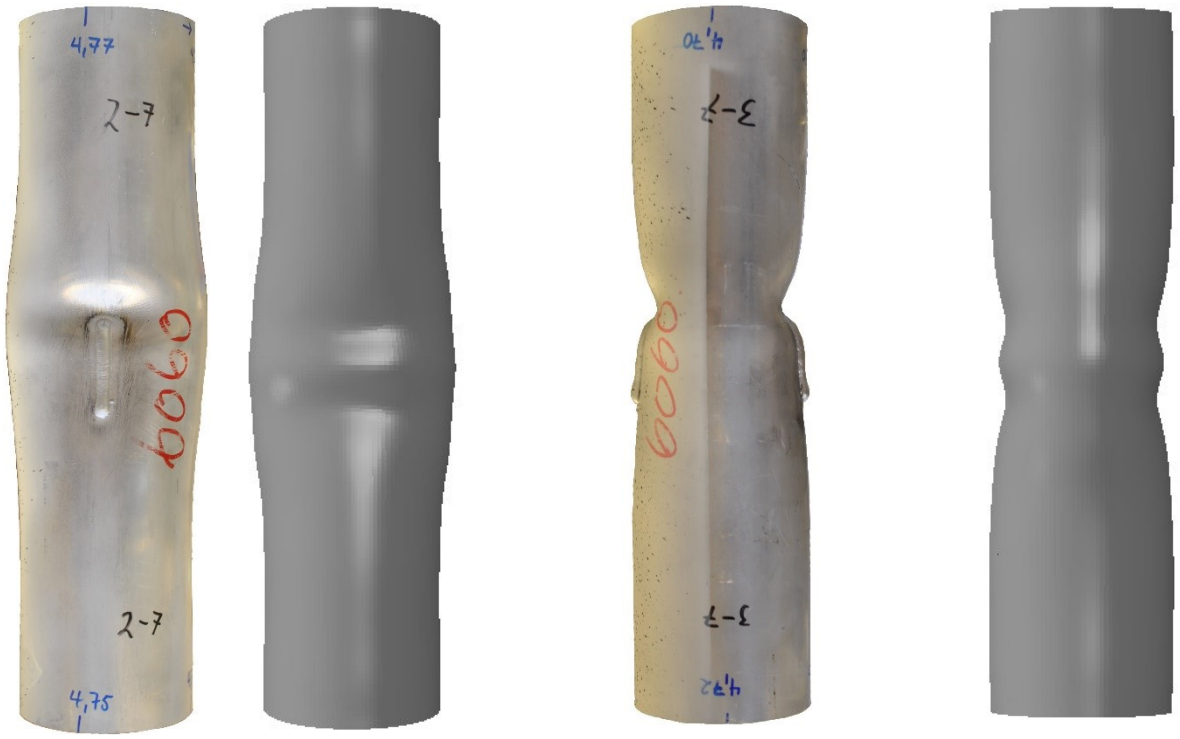

a) b) c) d)

Figure 9.13 – Buckling mode for a) & c) experiment and b) & d) numerical when displacement is 13 mm and the cylinders are oriented in the a) & b) y-z and c) & d) y-x plane for alloy 6060-T6, D=100 mm, t=4.8 mm, L=4D and meshsize ≈ 2.5 mm.

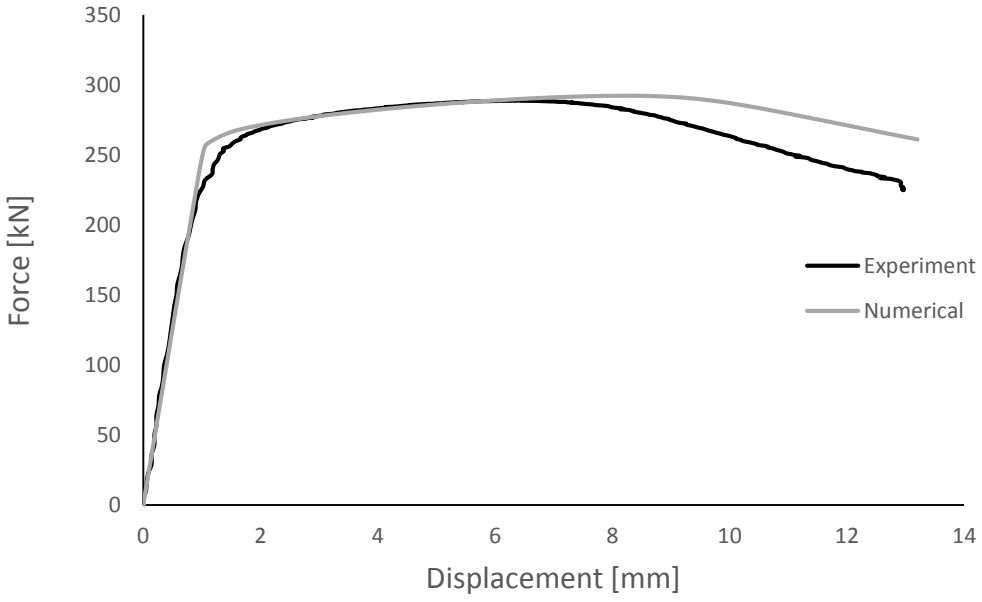

Figure 9.14 – Welded alloy 6060-T6, D=100 mm, t=4.8 mm and L=4D.

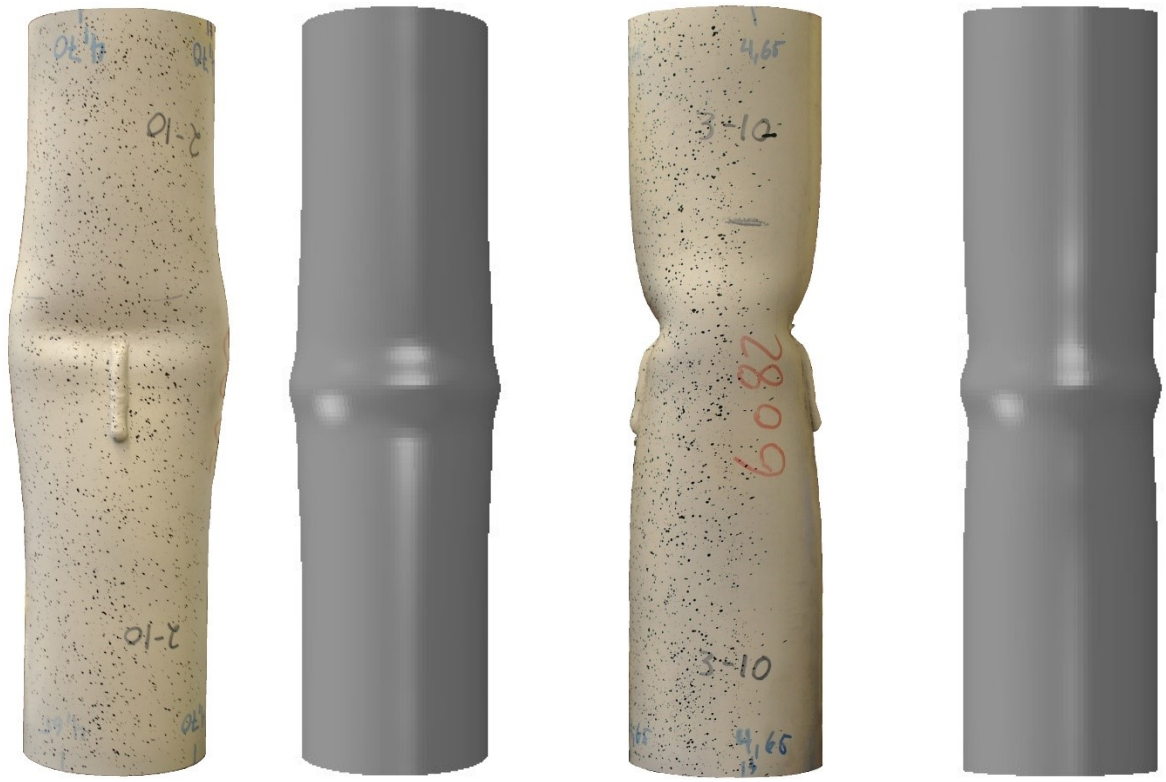

a) b) c) d)

Figure 9.15 – Buckling mode for a) & c) experiment and b) & d) numerical when displacement is 13 mm and the cylinders are oriented in the a) & b) y-z and c) & d) y-x plane for alloy 6082-T6, D=100 mm, t=4.8 mm, L=4D and meshsize ≈ 2.5 mm.

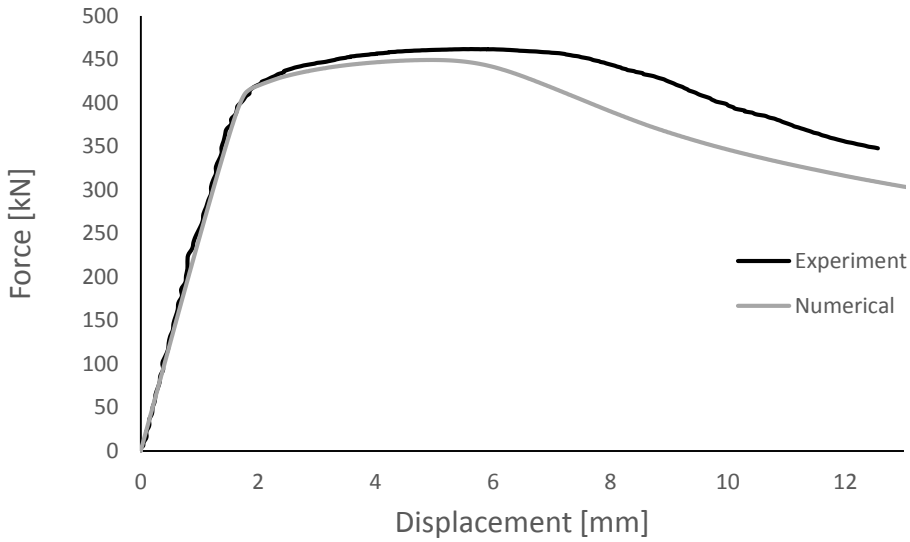

Figure 9.16 – Welded alloy 6082-T6, D=100 mm, t=4.8 mm and L=4D.

a) b) c)

Figure 9.17 – Buckling mode for a) experiment and b) & c) numerical when displacement is 7 mm and the cylinders are oriented in a) & b) y-z and c) y-x plane for alloy 6082-T6, D=100 mm, t=4.8 mm, L=2D and meshsize ≈ 1 mm.

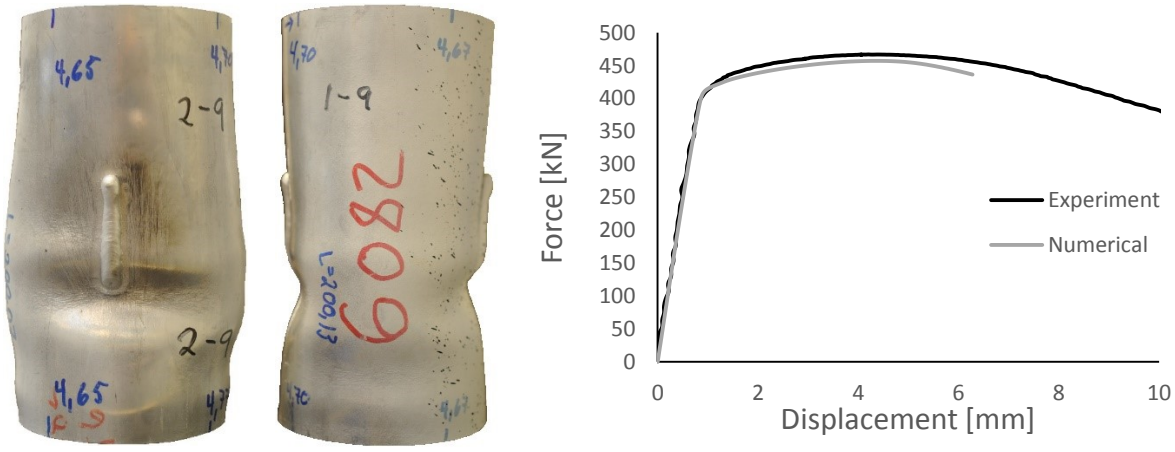

a) b) c)

Figure 9.18 – Buckling mode for a) & b) experiment when displacement is 10 mm and the cylinders are oriented in a) y-z and b) y-x plane. c) Force displacement for alloy 6082-T6, D=100 mm, t=4.8 mm and L=2D.

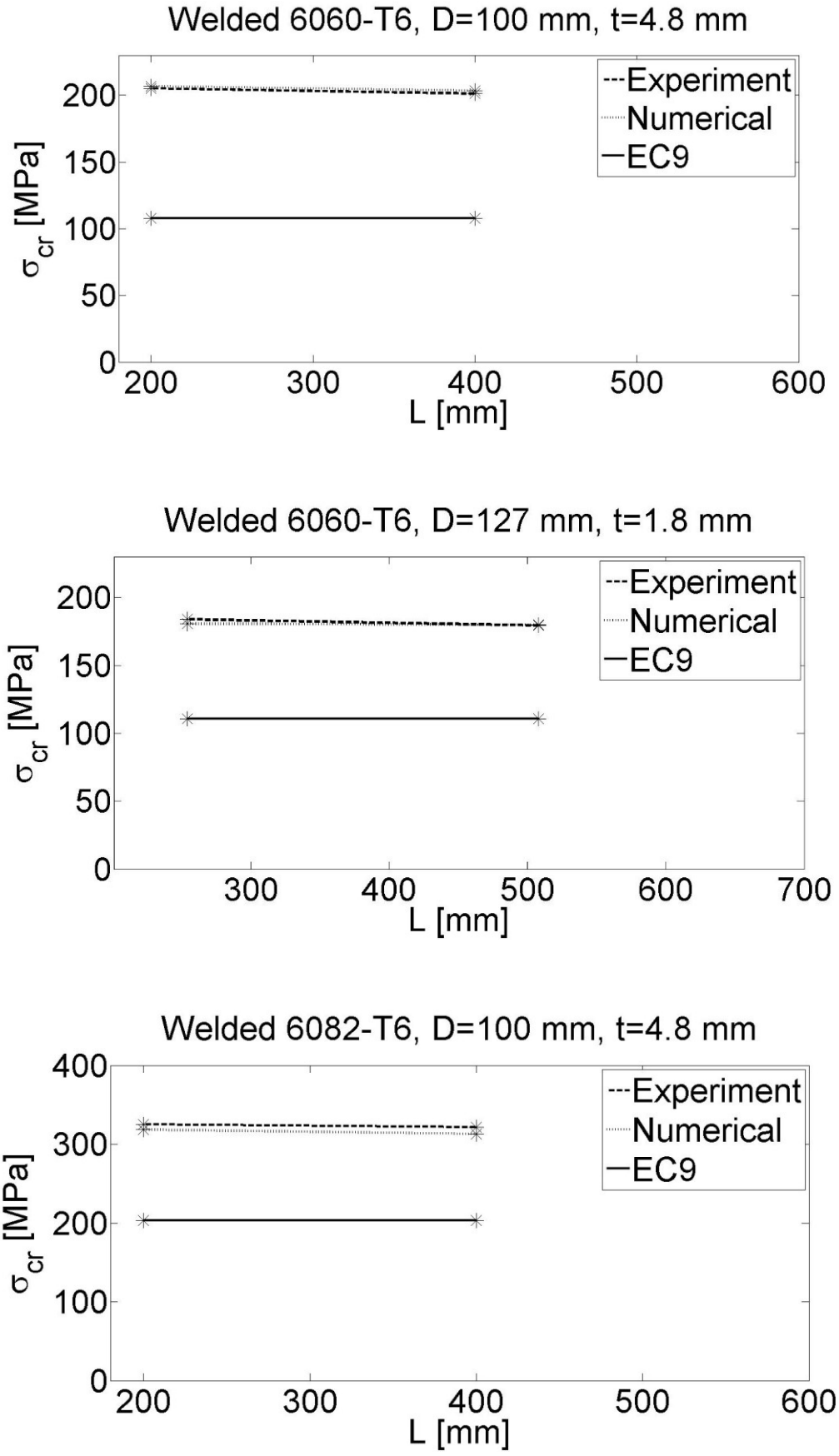

Figure 9.19 – Critical buckling stress for welded stub columns.

The calculations from EC9 are based on the effective area found in section 4 and the yield stress tabulated in EC9. When cylinder 6060-T6, D=127 mm, t=1.8 mm is subjected to welding, it becomes cross section class 4, otherwise all the cylinders are class 3 or lower.

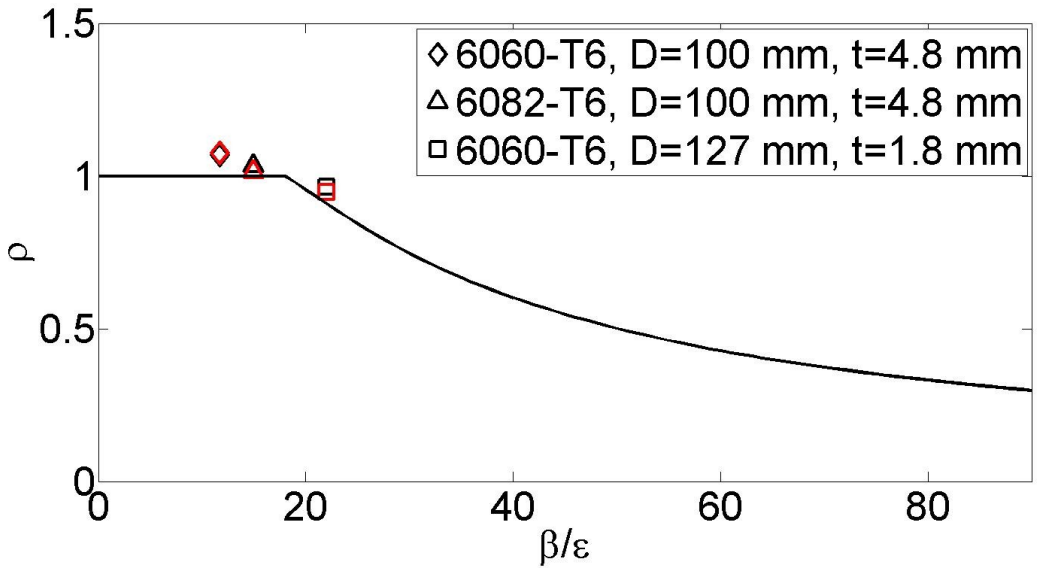

Figure 9.20 – Results from welded cross sections given as laboratory experiments (black points) and numerical results (red points) for L=2D. Calculations from EC9 represents the black line.

9.3 Comparison Welded and Unwelded Cross Sections

Critical buckling load for both laboratory experiments and numerical analysis for unwelded and welded cross sections of stub tests with length two and four times the diameter are given for the three cylinders in table 9.1.

Table 9.1 – Critical buckling load for unwelded and welded cross sections.

Cylinder	Unwelded [kN]		Welded [kN]	
	Exp.	Num.	Exp.	Num.
6060-T6, D=100 mm, t=4.8 mm, L=2D	311.40	310.41	294.63	296.90
6060-T6, D=100 mm, t=4.8 mm, L=4D	311.48	307.86	288.78	292.15
6060-T6, D=127 mm, t=1.8 mm, L=2D	138.15	134.86	132.05	129.74
6060-T6, D=127 mm, t=1.8 mm, L=4D	138.22	135.24	128.90	129.27
6082-T6, D=100 mm, t=4.8 mm, L=2D	505.57	473.62	466.92	457.25
6082-T6, D=100 mm, t=4.8 mm, L=4D	499.33	473.30	461.74	449.40

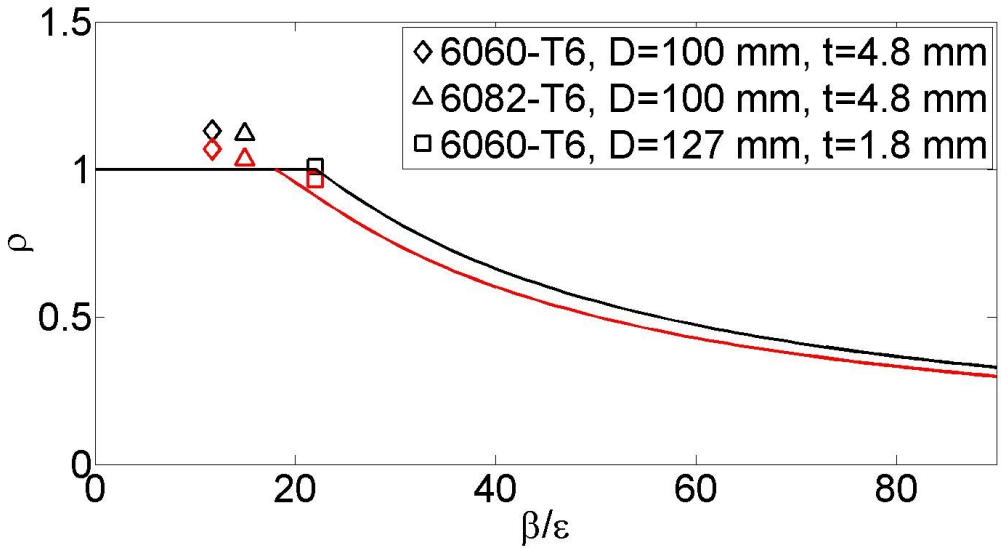

Figure 9.21 – Results from experiments of unwelded (black points) and welded (red points) cross sections for L=2D. Calculations from EC9 are given as black and red lines for unwelded and welded cross sections, respectively.

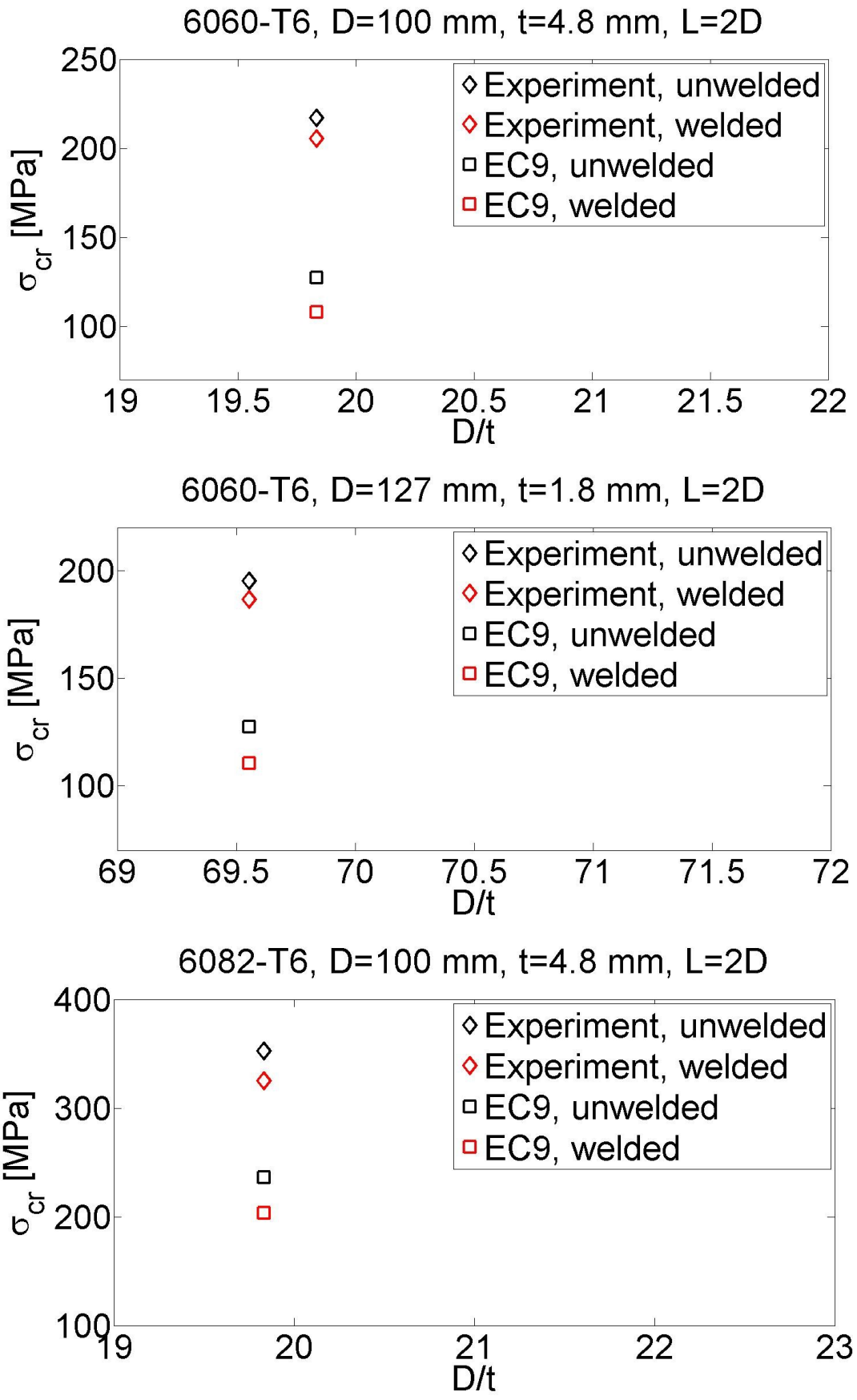

Figure 9.22 – Critical buckling stress when f_o is taken from EC9.

Figure 9.22 compares laboratory results with calculations from EC9 for both unwelded and welded cross sections when the yield stress is taken from EC9. If the yield stress, f_o is taken from the tensile test as the 0.2% permanent strain and used in calculations in EC9, figure 9.23 will give the deviation from the experiments. The 0.2% permanent strain in HAZ will be taken from the weld center and the reduction factor is given in table 5.7.

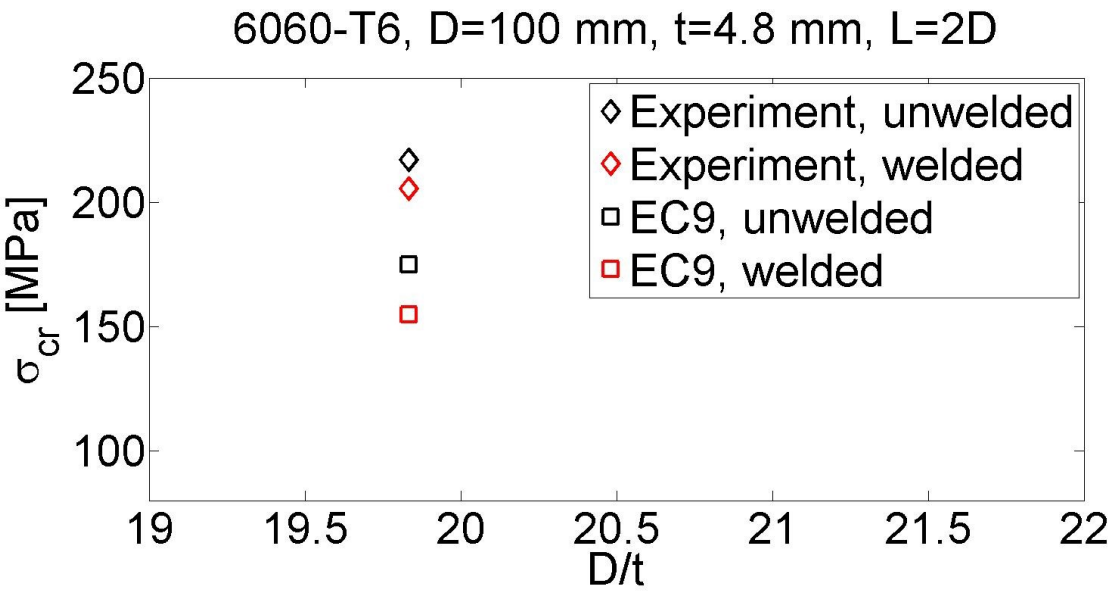

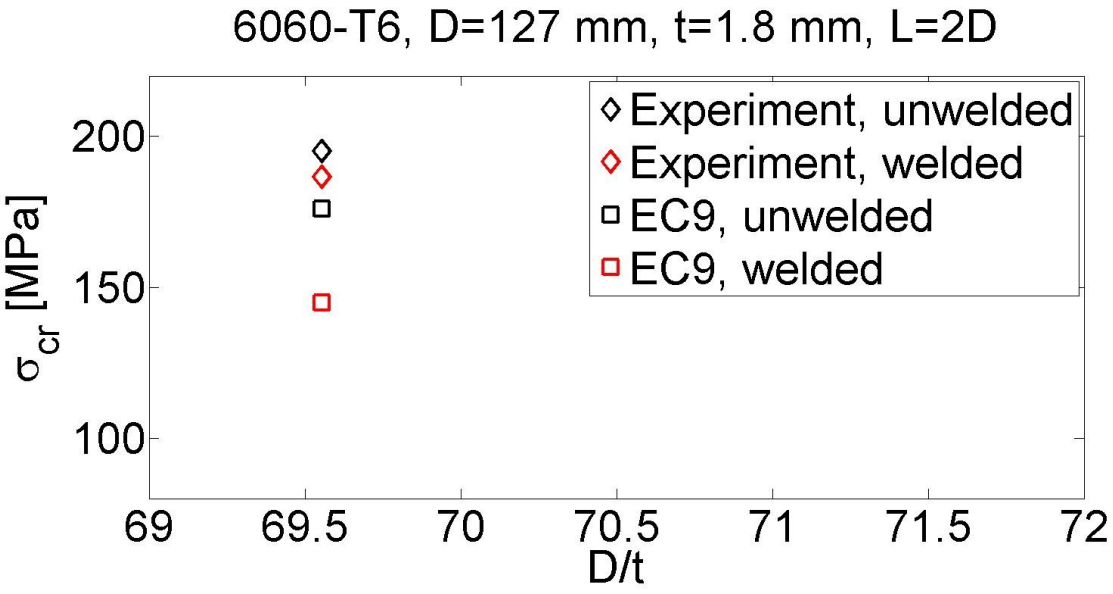

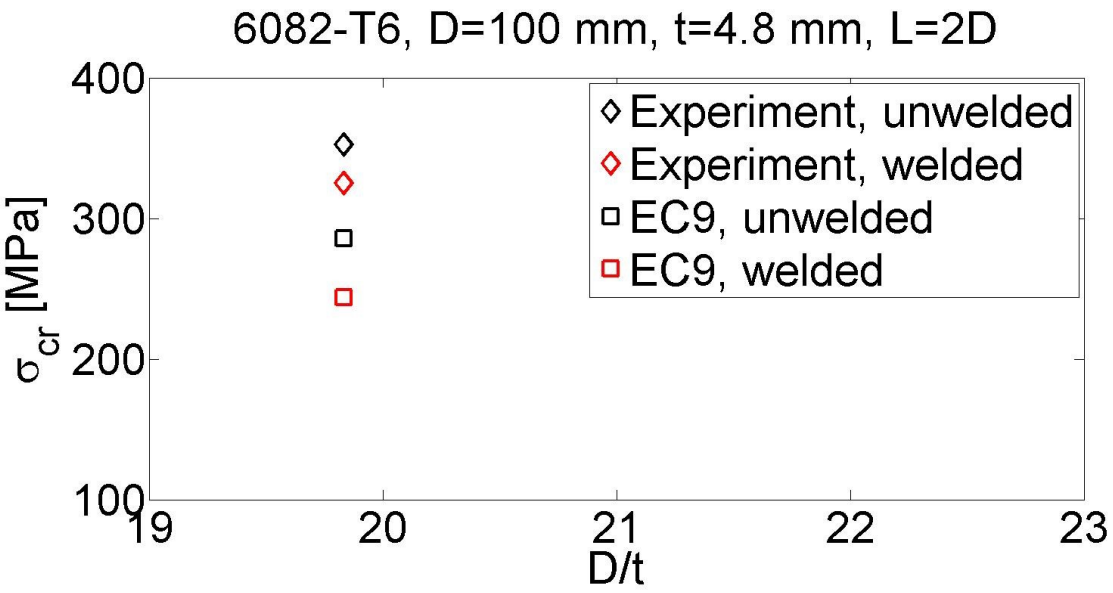

Figure 9.23 – Critical buckling stress when EC9 is calculated with f_o values from tensile tests in section 5.

Table 9.2 – EC9 calculations percentage below laboratory experiments for L=2D.

	f_o values from EC9 [%]		f_o values from tensile test [%]	
	Unwelded	Welded	Unwelded	Welded
6060-T6, D=100 mm, t=4.8 mm	38.4	47.4	19.4	24.6
6060-T6, D=127 mm, t=1.8 mm	33.8	39.8	9.8	22.3
6082-T6, D=100 mm, t=4.8 mm	29.5	37.4	18.8	25.0

9.4 Circumferential Wavenumber for Unwelded Cross Section

Equation [3.29] gives the relation between the longitudinal and circumferential wavenumber for unwelded thin walled cylinders compressed together. Figure 9.24 shows the relation for the thickest cylinder tested. All the 6082-T6 cylinders cracks at the same place as shown in figure 9.25, and therefore its clearly that the five cracks are triggered by $n = 5$ sinusoidal waves. Equation [3.29] shows that the circumferential wavenumber, n is dependent on the length, but results from testing of aluminium alloy 6082-T6 shows that n is independent of the two lengths tested. A reason for this might be that equation [3.29] is derived for thin walled cylinders, and this cylinder is very thick. Its worth nothing that n may change for

different lengths of thick cylinders too, but since it has to be an integer, it remains the same number. Anyhow, its clearly that equation [3.29] does not fit the laboratory results tested for the cylinders in this study. By the clear eye, its impossible to observe any longitudinal waves, except from the localisations at the ends, so this should be investigated further by for example DIC.

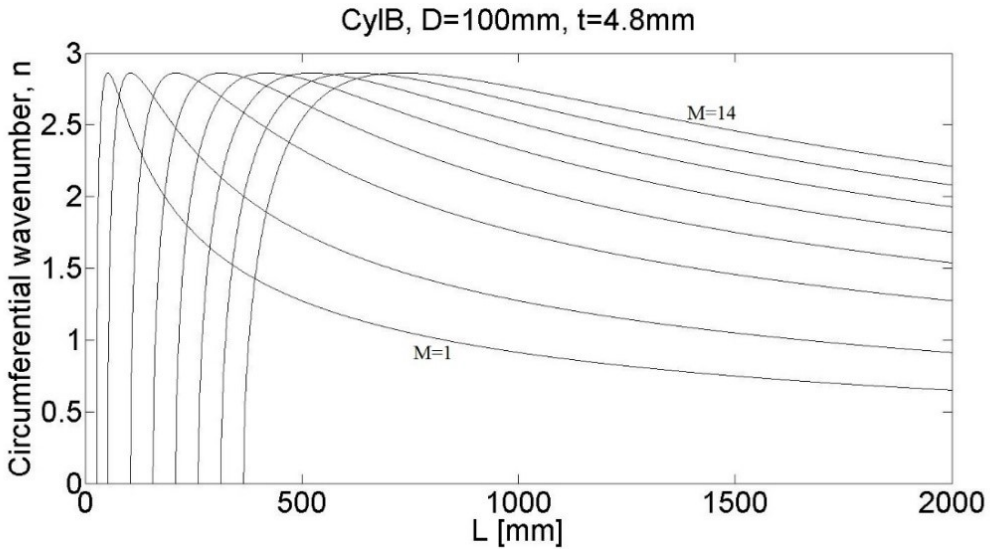

Figure 9.24 – Circumferential wavenumber, n vs length for different axial wavenumber, M_a.

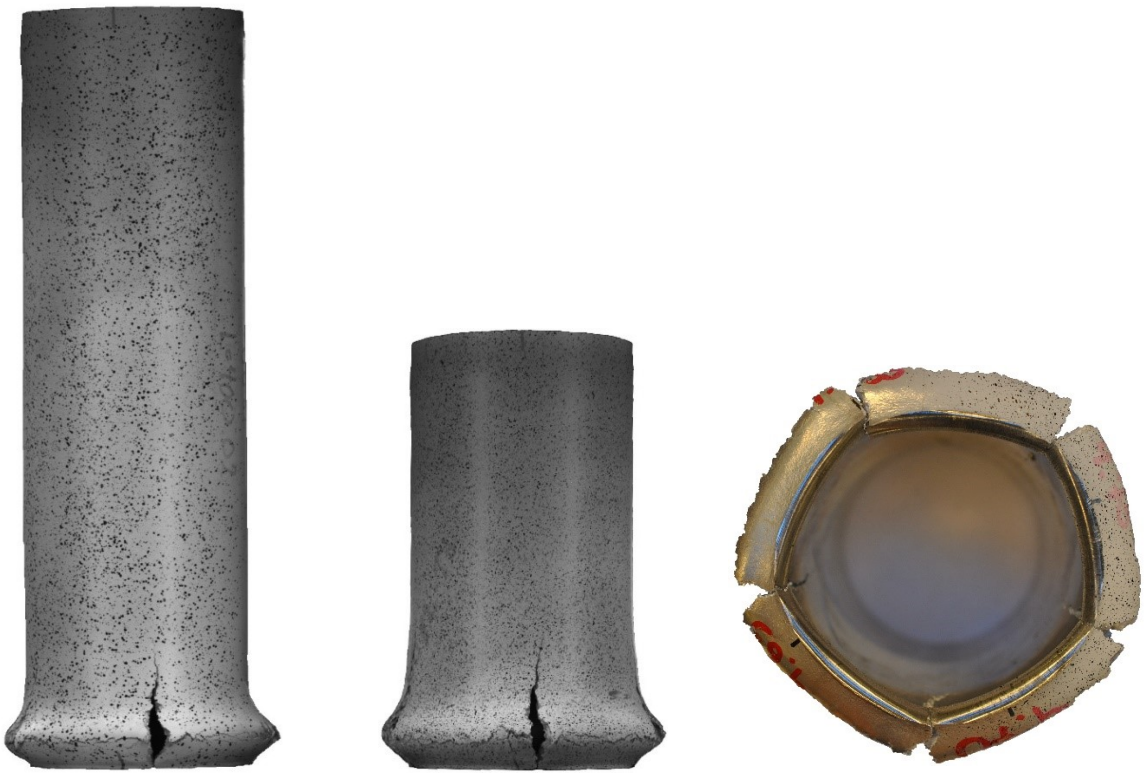

a) b) c)

Figure 9.25 – Laboratory results for unwelded alloy 6082-T6, D=100 mm, t=4.8 mm and a) L=4D and b) L=2D. c) Picture taken in the longitudinal axis.

a) b)

Figure 9.26 – Non-symmetrical/diamond form of a) laboratory results and b) numerical results of unwelded alloy 6060-T6, D=127 mm, t=1.8 mm and L=508 mm.

Its observed from figure 9.25 and 9.26 that for both unwelded cylinders 6060-T6, D=127 mm, t=1.8 mm, L=4D and 6082-T6, D=100 mm, t=4.8 mm the circumferential wavepattern corresponds to $n = 5$. For unwelded alloy 6060-T6, D=100 mm, t=4.8 mm, the deformation mode is symmetrical, i.e. $n = 0$.

9.5 Analytical Results for Unwelded Stubs

Equation [3.20] is plotted in figure 9.27-9.29 with tangent and secant modulus taken from tensile tests for the three cylinders. The elastic Poisson`s ratio is taken as 0.3. The intersection point with the curve found from tensile test is the critical buckling stress. Figure 9.30 compares the analytical results with laboratory experiments, numerical analysis and calculations from EC9 when f_o is taken from EC9 for a stub column when L=2D.

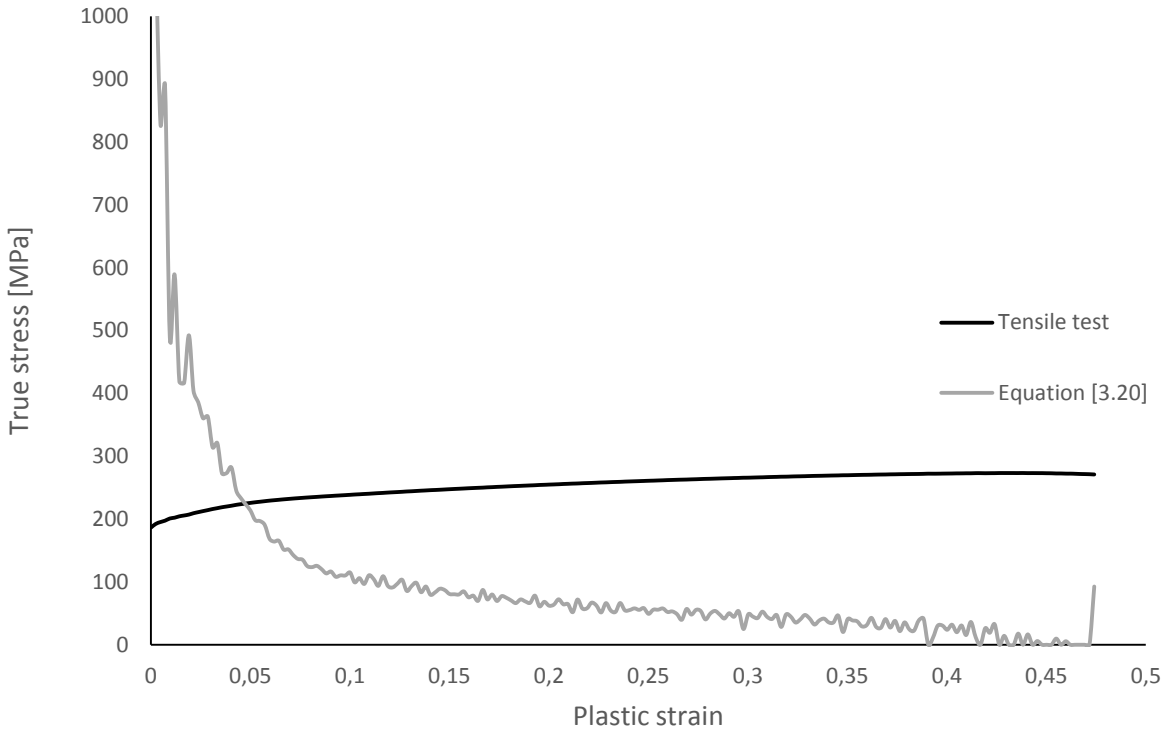

Figure 9.27 – Critical buckling stress from analytical equation for alloy 6060-T6, D=100 mm, t=4.8 mm.

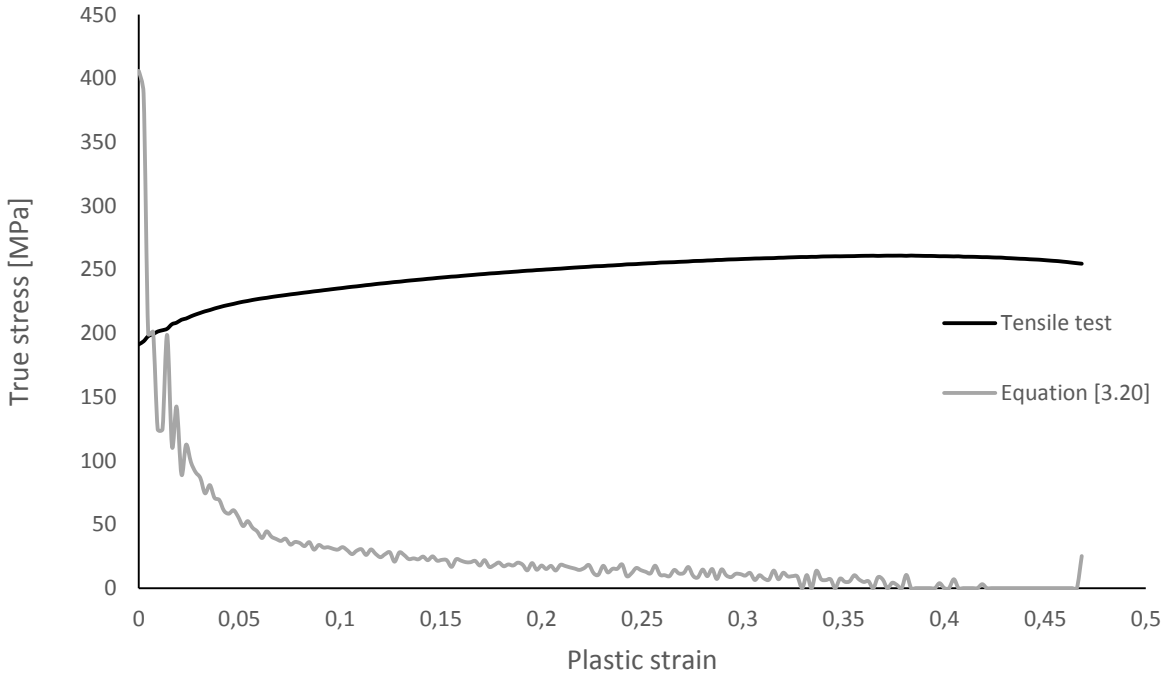

Figure 9.28 – Critical buckling stress from analytical equation for alloy 6060-T6, D=127 mm, t=1.8 mm.

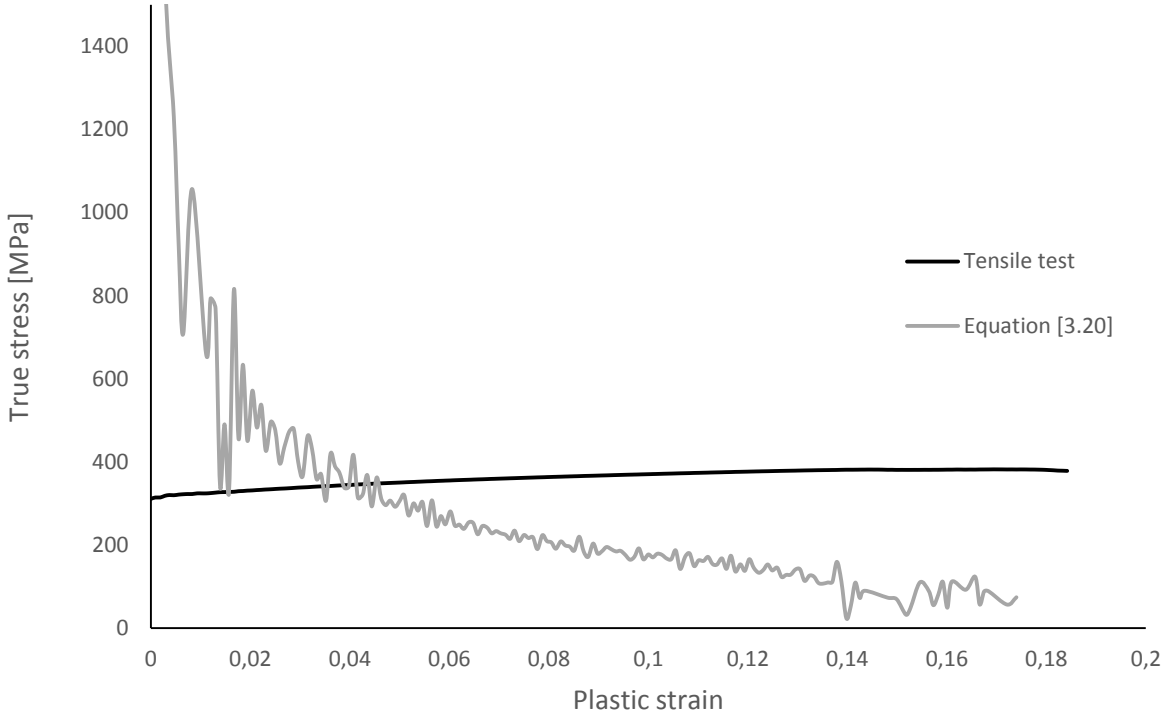

Figure 9.29 – Critical buckling stress from analytical equation for alloy 6082-T6, D=100 mm, t=4.8 mm.

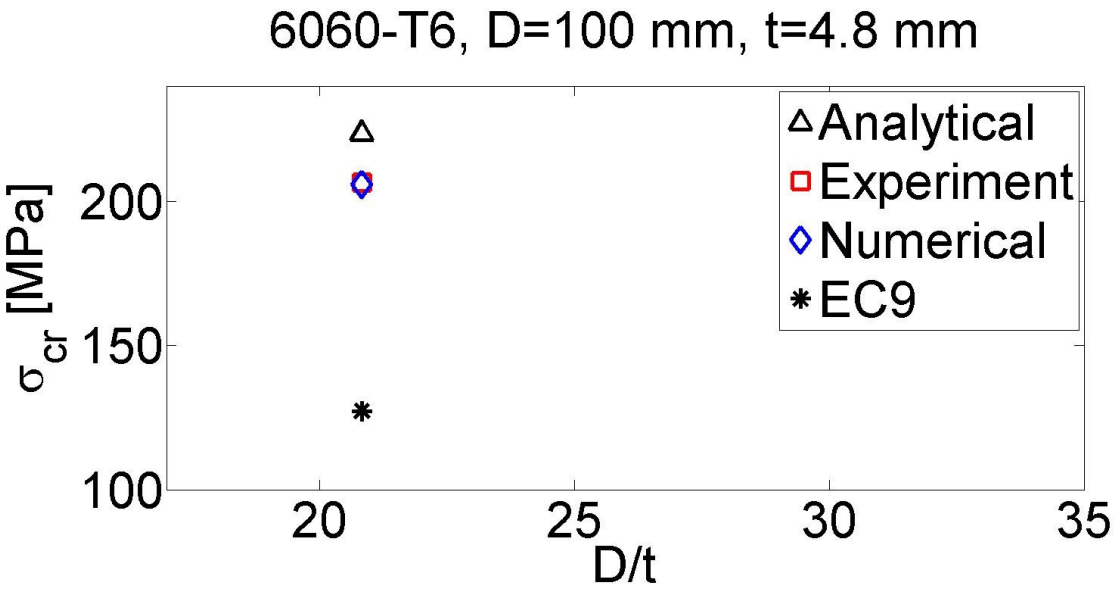

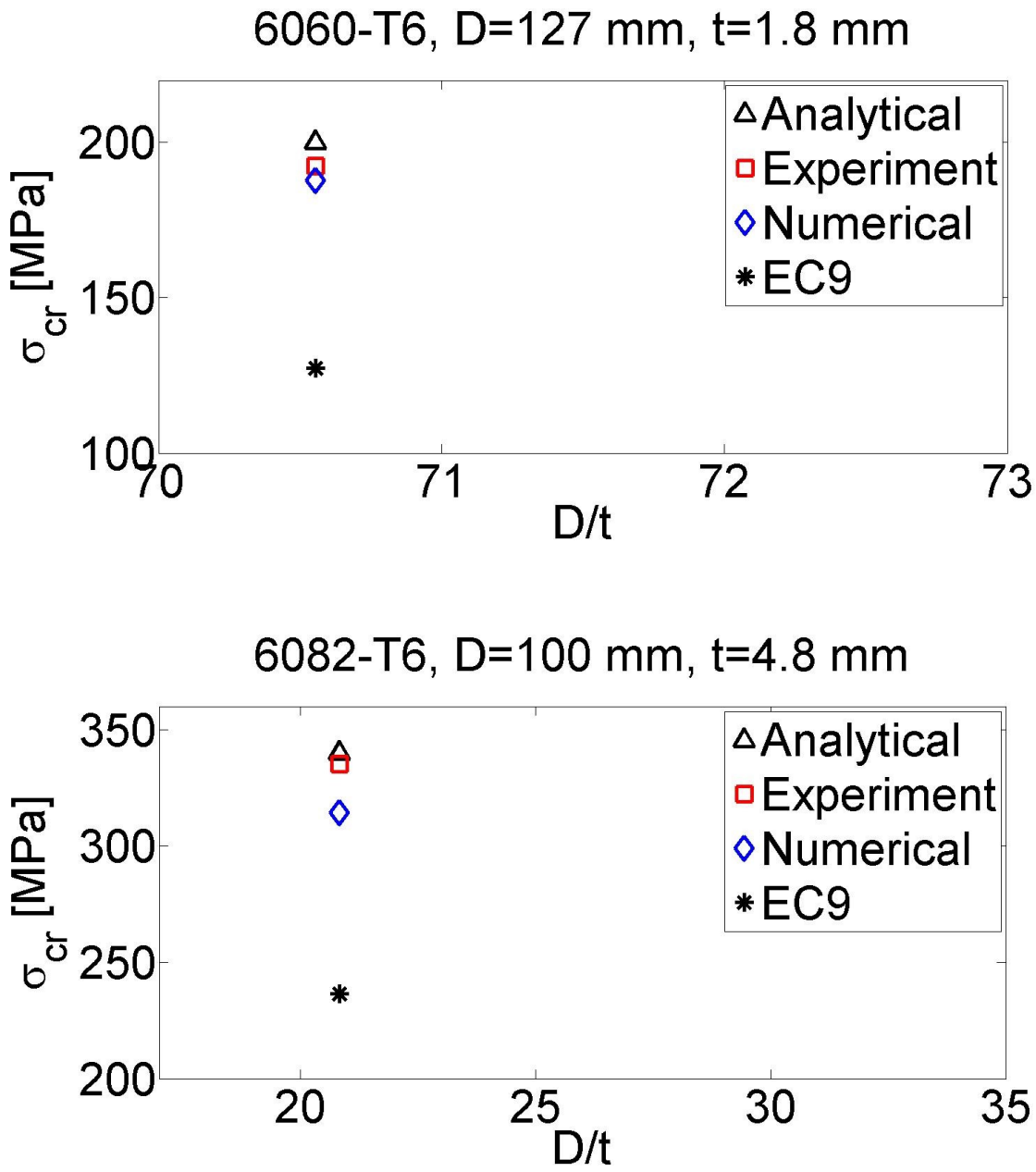

Figure 9.30 – Critical buckling stress for analytical equation, laboratory experiments, numerical analysis and calculations from EC9 when f_o is taken from EC9 for unwelded stubs, when L=2D.

9.6 Discussion

The numerical analysis for welded cross section of alloy 6060-T6, D=127 mm, t=1.8 mm gets a deformation mode identical to the laboratory result. The cylinder starts buckle in the middle, but it initiate at the end of the welds, for both numerical and laboratory results. Its also

observed for absolutely all cylinders tested that it initiate at that end where the thermal weld process ends. The welded cylinders with D=100 mm and t=4.8 mm, have a slightly different deformation modes for the numerical results than the laboratory. Its observed that the buckle initiates at the end of the welds, like for cylinder D=127 mm and t=1.8 mm, but the numerical analysis does not recreate this perfectly. Somehow, the analysis have a deformation mode symmetrically around the longitudinal center, unlike the laboratory results given in section 9.2.

10 Conclusions and Suggestions

10.1 Conclusions

The present study has investigated the structural behaviour of aluminium alloy 6060-T6 and 6082-T6 subjected to compression for both unwelded and welded cross sections experimentally, numerically, analytically and with calculations from EC9. Analytical formulas have been derived for long columns when the global buckling effect is dominating. The tensile test programme was completed without significant experimental problems and generally good repeatability was achieved for parallel specimens for alloy 6060-T6. For alloy 6082-T6, however large scatter occurred in the data most likely due to an extrusion weld. For this to be investigated more accurately, more tensile tests should be performed.

Based on experimental, numerical, analytical and EC9 results the following conclusions have been drawn:

1) For all three cylinders with different material and geometry combinations investigated in this study, calculations from EC9 is conservative for both unwelded and welded cross sections. For some cylinders the experiment results are almost twice the resistance calculated from EC9.

2) EC9 is even more conservative when welded cross sections are calculated.

3) Based on experimental results the critical buckling load is the same for cylinders that buckles locally. In this study, two lengths are compared, two and four times the diameter.

4) The analytical formulas for shell buckling fits the experiment results surprisingly well.

5) The numerical analysis fits very well to the experimental results. The force displacement curve fits very well, but also the buckling modes are achieved correctly for both unwelded and welded cross sections. Some deviations are discussed in section 9.6.

6) The analytical formulas for circumferential wavenumber derived for thin shells did not fit very well for the three cylinders investigated in this study. Results from very thin shells however, fitted great. This means that the cylinders in this study is not thin.

7) From numerical analysis, curvature in tensile test specimens did not have any effect.

8) Analytical formulas shows that increasing imperfection decreases the critical buckling load significantly for long columns. Therefore, its important to measure the imperfection before laboratory testing of long columns.

10.2 Suggestions for Further Work

Structural behaviour of aluminium subjected to compression is so far not widely investigated. More alloys should be tested to find the optimum material when it comes to strength and ductility. For aluminium alloy 6082-T6 more tensile tests should be performed to get a reliable stress strain relation. Since this study only tested short cylinders in the local buckling domain, laboratory experiments for long columns have to be performed and compared to EC9. To be able to do this, a suitable design is as mentioned suggested in section 6.4 and 7.3.

Compression tests should be performed to obtain any deviation in stress strain regarding the Bauschinger effect mentioned in section 2.2.

For welded cross sections, hardness tests, such as Vickers Hardness should be performed in the vicinity of a weld to get accurate material stress strain relation in the HAZ. Transversal welds could be of interest to investigate for both stub tests and long columns.

In the numerical analysis in this study, the half spheres on both ends in the HAZ is neglected, and so is the weld itself with the filler material. Therefore, this should be investigated more accurately to get reliable numerical results.

The critical buckling load for long columns are as shown in section 8 sensitive for imperfections. When laboratory experiments are performed, a study on the effect of imperfection could be of interest.

Numerical analysis of long columns should be performed with respect to different thickness distributions. As given in section 7.3 its observed that the thickness varies some for columns of five meters. The thickness could be distributed randomly with a given amplitude best fitted to the measurement in section 7.3.

References

Adams, R.A. (2003): Calculus – A complete course, fifth edition.

Alisibramulisi, A, Myhr, O.R., Lademo, O.G., Larsen, P.K. (2010): An Experimental Investigation of the Heat Affected Zone (HAZ) Properties of AA6060 and AA7046 Following Different Heat Treatment Schedules. The Japan Institute of Light Metals, pp. 994-999.

Altenpohl, D. (1982): Aluminium viewed from within. An introduction into the metallurgy of aluminum fabrication.

Andrew J. Deeks & Hong Hao (2005): Developments in Mechanics of Structures and Materials.

Batdorf, S.B. (1947): A simplified Method of Elastic-Stability Analysis for Thin Cylindrical Shells. 1 – Donnell`s equation. NACA TN 1341.

Eurocode 9 (2007): NS-EN 1999-1-1 Design of aluminium structures – Part 1-1: General structural rules, European Committee for Standardization (CEN).

George, G. and Becker, H. (1957): Part 3 – Buckling of curved plates and shells. NACA TN 3783.

Grong, Ø. (1997): Metallurgical Modelling of Welding, second edition.

Grong, Ø. and Myhr, O.R. (1993): Modelling of the strength distribution in the heat affected zone of 6082-T6 aluminium weldments, in Cerjak, H. and Easterling, K.E. (eds.): Mathematical Modelling of Weld Phenomena, The Institute of Materials, pp. 300-311.

Hopperstad, O.S., Langseth, M. and Hanssen, A.G. (2000): "Static and dynamic crushing of circular aluminium extrusions with aluminium foam filler". Int. J. Impact Eng. 24, 475-507.

Hopperstad, O.S., Langseth, M. and Hanssen, L. (1997): Ultimate Compressive Strength of Plate Elements in Aluminium: Correlation of Finite Element Analyses and Tests. Thin-Walled Structures Vol. 29, Nos. 1-4, pp. 31-46.

Hunt, G.W.; Lord, G.J.; Peletier, M.A.: Cylindrical shell buckling: A characterization of localization and periodicity. Discrete and Continuous Dynamical Systems - Series B, November 2003, Vol.3(4), pp. 505-518.

Koiter, W.T. (1945): The stability of elastic equilibrium.

Langseth, M. (2016): Buckling of circular cylindrical shells, elastic and plastic buckling.

Matusiak, M. (1999): Strength and ductility of welded structures in aluminium alloys.

NS-EN 1090-3:2008 – Part 3: Technical requirements for aluminium structures.

Ramberg, W. and Osgood, W.R. (1943): Description of stress-strain curves by three parameters, National advisory committee of aeronautics, Technical Note No. 902.

Tsien, H.S (1942): A theory for the buckling of thin shells. Journal of the aeronautical sciences, vol 9, pp. 373-384.

Wang, T. (2006) – Modelling of Welded Thin-Walled Aluminium Structures.

.

Appendix A – Derivation of Curvature

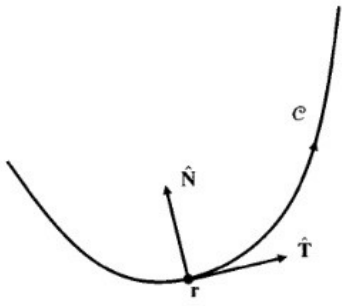

Figure A.1 – Parametric curve.

A curvature, C lays on the parametric curve **r**=**r(**t). At the point **r**=**r**(t), a velocity vector **v**(t)=d**r**/dt is tangent to this point. Its assumed that **v**(t)≠0 and by dividing **v**(t) by its length, a unit tangent vector $\widehat{\boldsymbol{T}}(t)$ is found at point **r**(t)

$$\widehat{\boldsymbol{T}}(t) = \frac{\boldsymbol{v}(t)}{v(t)} = \frac{\frac{d\boldsymbol{r}}{dx}}{\left|\frac{d\boldsymbol{r}}{dx}\right|} \qquad [A.1]$$

Its known that a curve parametrized in terms of arc length, **r**=**r**(s) is traced at unit speed v(s)=1, Adams (2003). Thus

$$\widehat{\boldsymbol{T}}(s) = \frac{d\boldsymbol{r}}{ds} \qquad [A.2]$$

The relation between curvature and the unit tangent vector will therefore be found from taken the length of $d\widehat{\boldsymbol{T}}/ds$ at the point **r**(t)

$$\kappa(s) = \left|\frac{d\widehat{\boldsymbol{T}}}{ds}\right| \qquad [A.3]$$

The radius of curvature thus becomes

$$R = \frac{1}{\kappa(s)} \qquad [A.4]$$

To obtain a unit normal vector, $\widehat{\boldsymbol{N}}$ in the same direction, $d\widehat{\boldsymbol{T}}/ds$ is only divided by its length κ(s), as done for the tangent vector assuming that κ(s)≠0

$$\widehat{\boldsymbol{N}}(s) = \frac{1}{\kappa(s)}\frac{d\widehat{\boldsymbol{T}}}{ds} = \frac{\frac{d\widehat{\boldsymbol{T}}}{ds}}{\left|\frac{d\widehat{\boldsymbol{T}}}{ds}\right|} \qquad [A.5]$$

The curve will now be expressed in terms of arc-length parameters, and these quantities are found in terms of a general parametrization **r**=**r**(t) where the velocity, **v**(t), the speed, v(t)=$|\boldsymbol{v}(t)|$ and the acceleration, **a**(t) are obtained from the point **r**(t)

$$\boldsymbol{v} = \frac{d\boldsymbol{r}}{dt} = \frac{d\boldsymbol{r}}{ds}\frac{ds}{dt} = v\widehat{\boldsymbol{T}} \qquad [A.6]$$

$$\boldsymbol{a} = \frac{d\boldsymbol{v}}{dt} = \frac{dv}{dt}\widehat{\boldsymbol{T}} + v\frac{d\widehat{\boldsymbol{T}}}{dt} = \frac{dv}{dt}\widehat{\boldsymbol{T}} + v\frac{d\widehat{\boldsymbol{T}}}{ds}\frac{ds}{dt} = \frac{dv}{dt}\widehat{\boldsymbol{T}} + v^2\kappa\widehat{\boldsymbol{N}} \qquad [A.7]$$

If the cross product of these two vectors are obtained, a usefull expression for κ can be found

$$\boldsymbol{v}\times\boldsymbol{a} = v\frac{dv}{dt}\widehat{\boldsymbol{T}}\times\widehat{\boldsymbol{T}} + v^3\kappa\widehat{\boldsymbol{T}}\times\widehat{\boldsymbol{N}} = v^3\kappa\frac{\boldsymbol{v}\times\boldsymbol{a}}{|\boldsymbol{v}\times\boldsymbol{a}|} \qquad [A.8]$$

$$\kappa = \frac{|\boldsymbol{v}\times\boldsymbol{a}|}{v^3} = \frac{|\boldsymbol{v}\times\boldsymbol{a}|}{|\boldsymbol{v}|^3} \qquad [A.9a]$$

$$\kappa = \frac{|\boldsymbol{v}\times\boldsymbol{a}|}{\sqrt{\boldsymbol{v}^2}^3} \qquad [A.9b]$$

A general plane curve with the equation y=f(x) is used to obtain a general expression for the curvature. The graph can be parametrized as **r**=x**i**+f(x)**j**, and the following quantities are

$$\boldsymbol{v} = \boldsymbol{i} + f'(x)\boldsymbol{j} \qquad [A.10]$$

$$\boldsymbol{a} = f''(x)\boldsymbol{j} \qquad [A.11]$$

$$\boldsymbol{v}\times\boldsymbol{a} = f''(x)\boldsymbol{k} \qquad [A.12]$$

Inserting equation [A.10] and [A.12] into [A.9b] yields

$$\kappa(x) = \frac{|f''(x)|}{\left(1+\left(f'(x)\right)^2\right)^{\frac{3}{2}}} \qquad [A.13]$$

Appendix B – Geometric Stiffness

$$[\boldsymbol{K}]_m = \sum_{i=1}^{n_{el}} [\boldsymbol{L}]_i{}^T [k_m]_i [\boldsymbol{L}]_i \quad [B.1]$$

$$[\boldsymbol{K}]_g = \sum_{i=1}^{n_{el}} [\boldsymbol{L}]_i{}^T \left[k_g\right]_i [\boldsymbol{L}]_i \quad [B.2]$$

$$[k_m] = \int_V [\boldsymbol{B}]^T [\boldsymbol{E}]\, [\boldsymbol{B}] dV \quad [B.3]$$

$$\left[k_g\right] = \int_V [\boldsymbol{G}]^T [\boldsymbol{S}]\, [\boldsymbol{G}] dV \quad [B.4]$$

where

$[\boldsymbol{B}] = [\boldsymbol{\partial}][\boldsymbol{N}]$

$[\boldsymbol{G}] = [\boldsymbol{\nabla}][\boldsymbol{N}]$

$$[\boldsymbol{S}] = \begin{bmatrix} \boldsymbol{\sigma} & 0 & 0 \\ 0 & \boldsymbol{\sigma} & 0 \\ 0 & 0 & \boldsymbol{\sigma} \end{bmatrix}, [\sigma] = \begin{bmatrix} \sigma_x & \tau_{xy} & \tau_{xz} \\ \tau_{yx} & \sigma_y & \tau_{yz} \\ \tau_{zx} & \tau_{zy} & \sigma_z \end{bmatrix}$$

$[\boldsymbol{S}]$ contains axial membrane stress and $[\boldsymbol{N}]$ is the shape functions.

Appendix C – Wavenumber, n from section 3

Table C.1 – D=127 mm, t=0.4 mm

Length [mm]	M_a	n Equation [3.29]	n Numerical
50	5	7.8	2
100	3	9.9	7
200	6	9.9	5
400	7	8.1	0

Table C.2 – D=127 mm, t=1.8 mm

Length [mm]	M_a	n Equation [3.29]	n Numerical
50	1	5.2	2
100	3	5.3	3
200	3	4.8	6
400	3	3.7	3

Table C.3 – D=127 mm, t=0.1 mm

Length [mm]	M_a	n Equation [3.29]	n Numerical
50	7	22.2	15
100	5	18.7	23
200	5	14.1	18
400	7	12.0	17

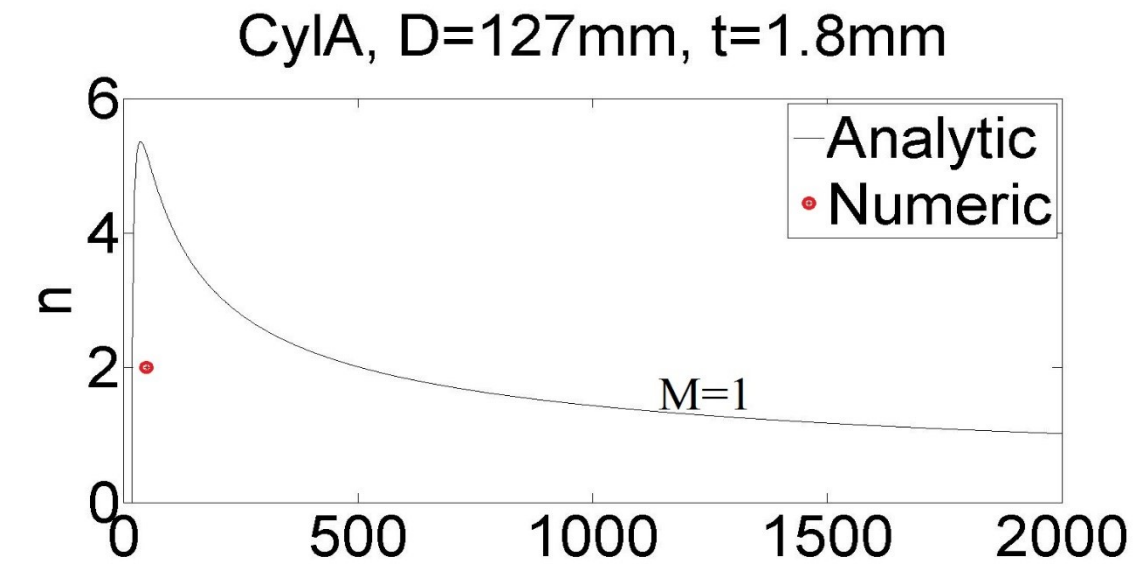
CylA, D=127mm, t=1.8mm
Analytic
Numeric
M=1
n
0
2
4
6
0
500
1000
1500
2000

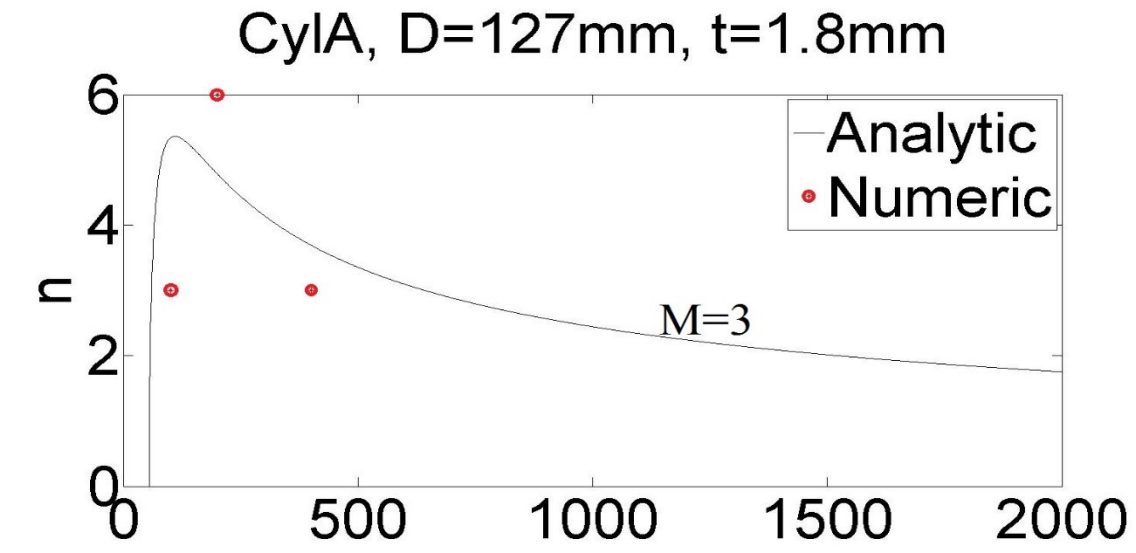
CylA, D=127mm, t=1.8mm
Analytic
Numeric
M=3
n
0
2
4
6
0
500
1000
1500
2000

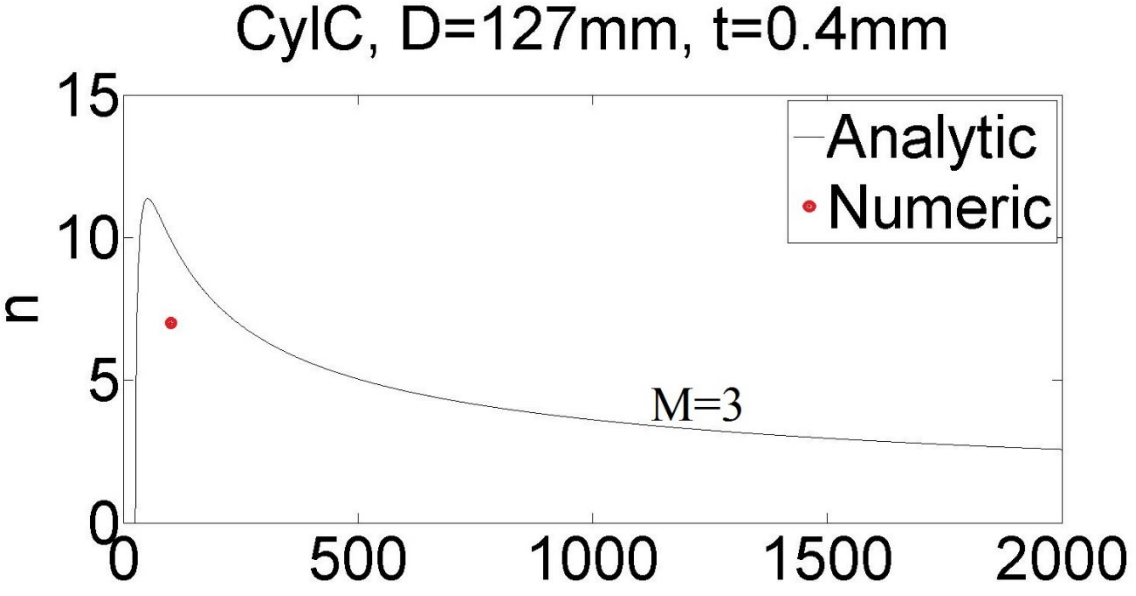
CylC, D=127mm, t=0.4mm
Analytic
Numeric
M=3
n
0
5
10
15
0
500
1000
1500
2000

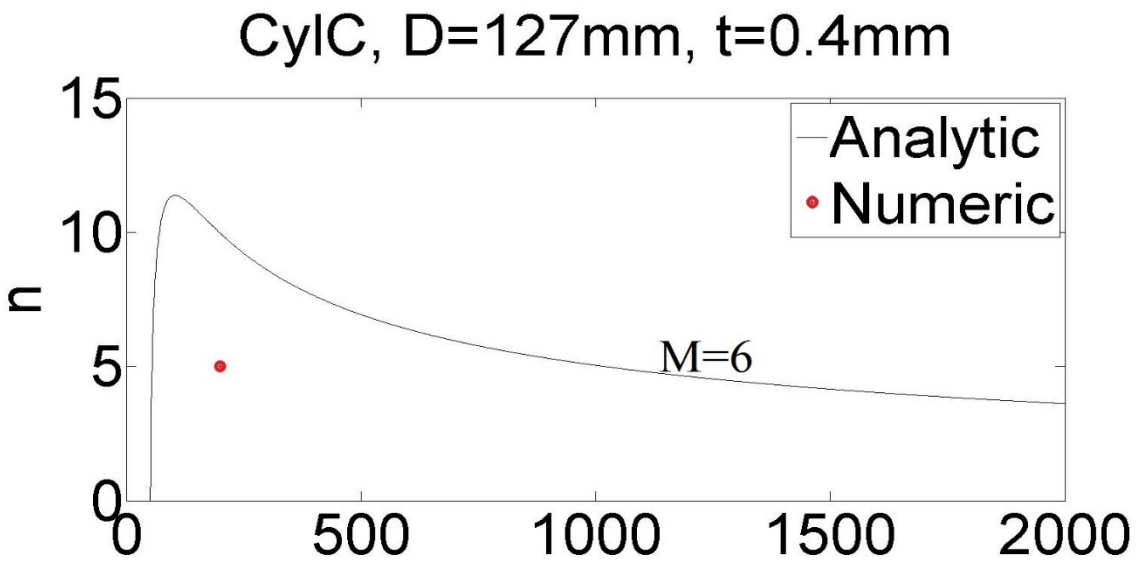
CylC, D=127mm, t=0.4mm
n
15
10
5
0
0
500
1000
1500
2000
Analytic
Numeric
M=6

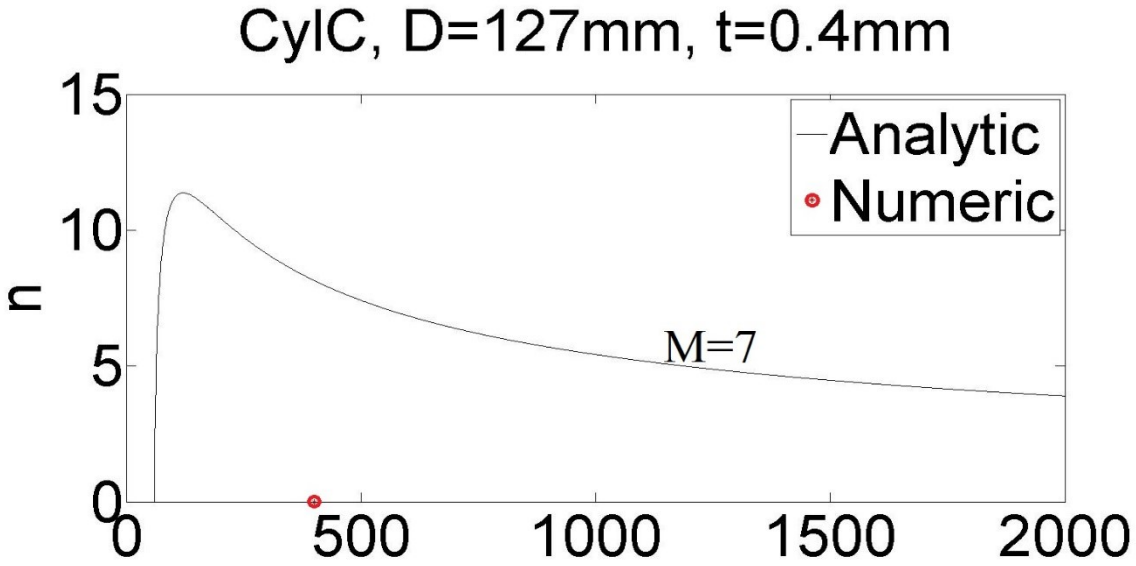
CylC, D=127mm, t=0.4mm
n
15
10
5
0
0
500
1000
1500
2000
Analytic
Numeric
M=7

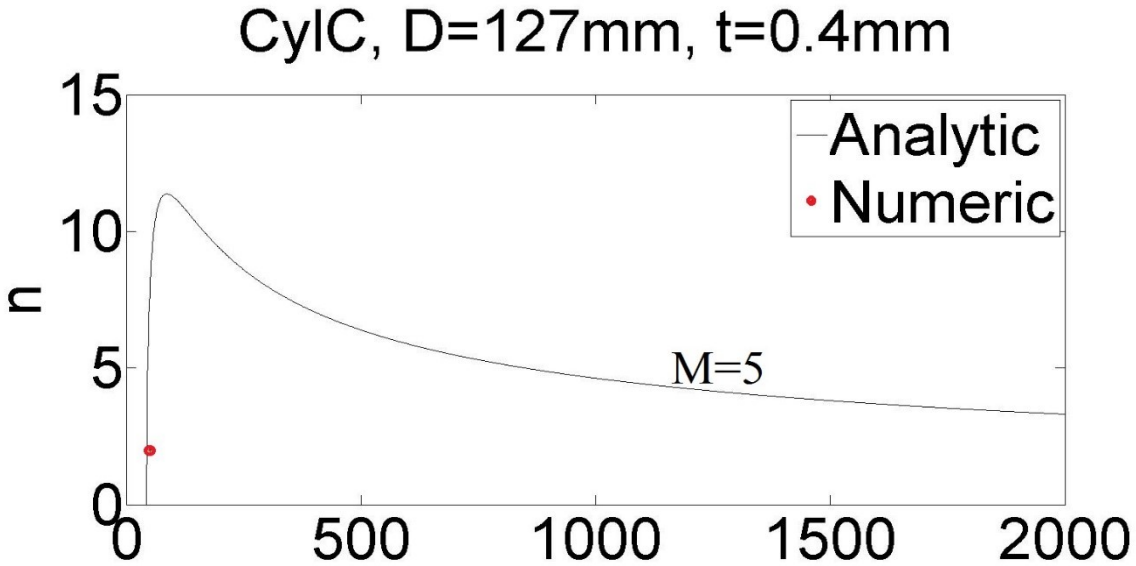
CylC, D=127mm, t=0.4mm
n
15
10
5
0
0
500
1000
1500
2000
Analytic
Numeric
M=5

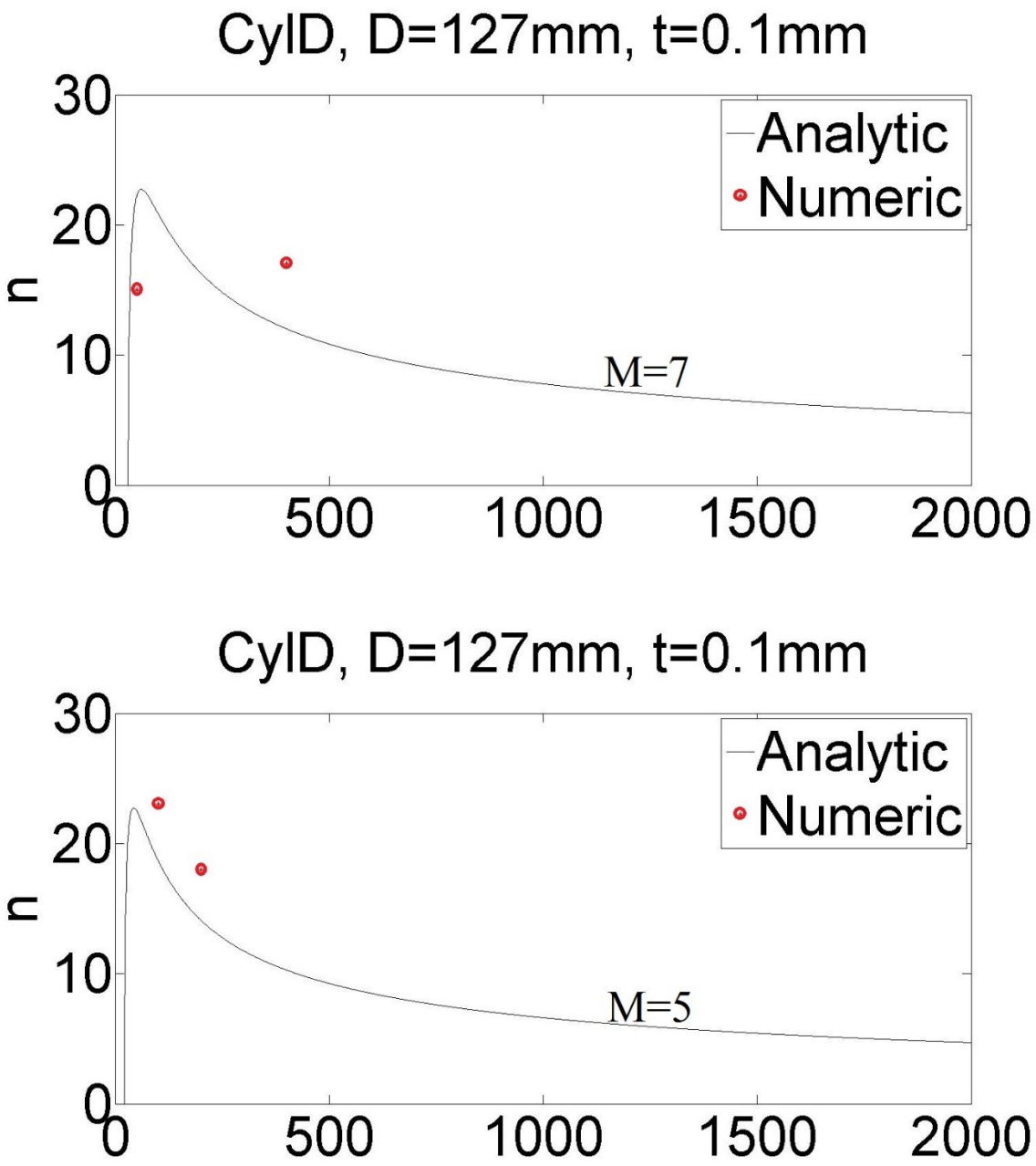

Figure C.1 – Circumferential wavepattern versus length [mm] for different cylinders and different longitudinal half waves.

Appendix D – Explanation for Stub Tests

Table D.1 – Unwelded stubs.

Test	Material	Diameter [mm]	Thickness [mm]	Length [mm]
1-1	6060-T6	100	4.8	400
2-1	6060-T6	100	4.8	400
3-1	6060-T6	100	4.8	400
1-2	6060-T6	100	4.8	200
2-2	6060-T6	100	4.8	200
3-2	6060-T6	100	4.8	200
1-3	6082-T6	100	4.8	200
2-3	6082-T6	100	4.8	200
3-3	6082-T6	100	4.8	200
1-4	6082-T6	100	4.8	400
2-4	6082-T6	100	4.8	400
3-4	6082-T6	100	4.8	400
1-5	6060-T6	127	1.8	508
2-5	6060-T6	127	1.8	508
3-5	6060-T6	127	1.8	508
1-6	6060-T6	127	1.8	254
2-6	6060-T6	127	1.8	254
3-6	6060-T6	127	1.8	254

Table D.2 – Welded stubs.

1-7	6060-T6	100	4.8	400
2-7	6060-T6	100	4.8	400
3-7	6060-T6	100	4.8	400
1-8	6060-T6	100	4.8	200
2-8	6060-T6	100	4.8	200
3-8	6060-T6	100	4.8	200
1-9	6082-T6	100	4.8	200
2-9	6082-T6	100	4.8	200
3-9	6082-T6	100	4.8	200
1-10	6082-T6	100	4.8	400
2-10	6082-T6	100	4.8	400
3-10	6082-T6	100	4.8	400
1-11	6060-T6	127	1.8	508
2-11	6060-T6	127	1.8	508
3-11	6060-T6	127	1.8	508
1-12	6060-T6	127	1.8	254
2-12	6060-T6	127	1.8	254
3-12	6060-T6	127	1.8	254

Appendix E – Hardening Parameters in HAZ used in Numerical Analysis

Tabel E.1 – Hardening parameters in HAZ for 6082-T6, D=100 mm, t=4.8 mm.

Zone	Y_0 [MPa]	Q_1 [MPa]	C_1 [-]	Q_2 [MPa]	C_2 [-]	$\sigma_0 + \sum Q_i$ [MPa]
Weld	105	42	656	189	13	336
4 mm away	120	38	616	157	18	314
8 mm away	101	47	669	131	22	280
12 mm away	168	51	1091	74	33	293
16 mm away	200	84	2811	60	30	343
20 mm away	221	88	6095	61	19	369
24 mm away	209	100	2780	57	24	365
28 mm away	240	72	3196	52	29	364
Base material	311	28	9	57	15	396

Tabel E.2 – Hardening parameters in HAZ for 6060-T6, D=100 mm, t=4.8 mm.

Zone	Y_0 [MPa]	Q_1 [MPa]	C_1 [-]	Q_2 [MPa]	C_2 [-]	$\sigma_0 + \sum Q_i$ [MPa]
Weld	108	10	50	58	8	175
2 mm away	105	10	50	58	8	172
4 mm away	96	10	50	60	8	165
6 mm away	105	10	50	58	8	172
8 mm away	162	13	50	49	8	222
10 mm away	180	14	50	45	8	237
Base material	186	16	50	69	8	271

Tabel E.3 – Hardening parameters in HAZ for 6060-T6, D=127 mm, t=1.8 mm.

Zone	Y_0 [MPa]	Q_1 [MPa]	C_1 [-]	Q_2 [MPa]	C_2 [-]	$\sigma_0 + \sum Q_i$ [MPa]
Weld	111	12	40	47	8	169
2 mm away	107	11	40	49	8	166
4 mm away	99	11	40	49	8	158
6 mm away	107	11	40	49	8	166
8 mm away	166	15	40	33	8	213
10 mm away	185	16	40	29	8	229
Base material	191	18	40	51	8	260

Appendix F – Correction for Displacement in Tensile Tests

```
dirF='D:\Skule\5.klasse\Masteroppgåve\Strekktest vår
2016\2016-03-03-Marius\'
testName='3-2'
ForceFile=dlmread([dirF testName '.txt'],'\t',1,0);

A0=7.9*4.81

lData=1:500;
Le=45
E=70000
u1=Le*1000*ForceFile(lData,2)/(A0*E)
u2=ForceFile(lData,3)-u1;
plot(1000*ForceFile(lData,2),u2)
f=@(a,b,c,d,e,x)a*(1-exp(-x*b))+c*(1-exp(-x*d))+e*x
x=1000*ForceFile(lData,2);
hold on
plot(x,f(0.23,2e-3,10e-5,1.8e-3,0.84e-4,x),'k')
%%
lData=1:length(ForceFile(:,3));
u1tot=ForceFile(lData,3)-f(0.23,2e-3,10e-5,1.8e-3,0.84e-
4,1000*ForceFile(lData,2))
plot(u1tot,1000*ForceFile(lData,2))
```

Appendix G – Laboratory Results from Stub Tests

G.1 Unwelded Cylinders

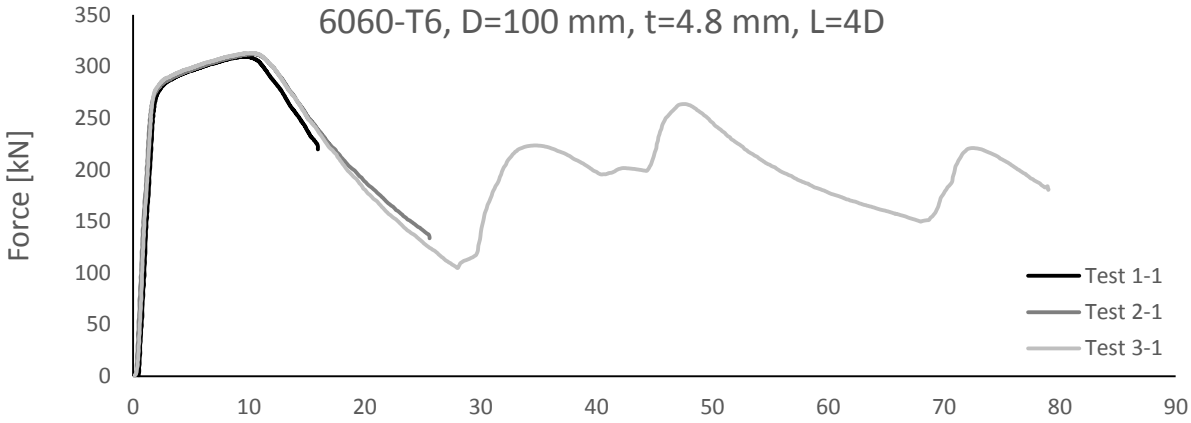

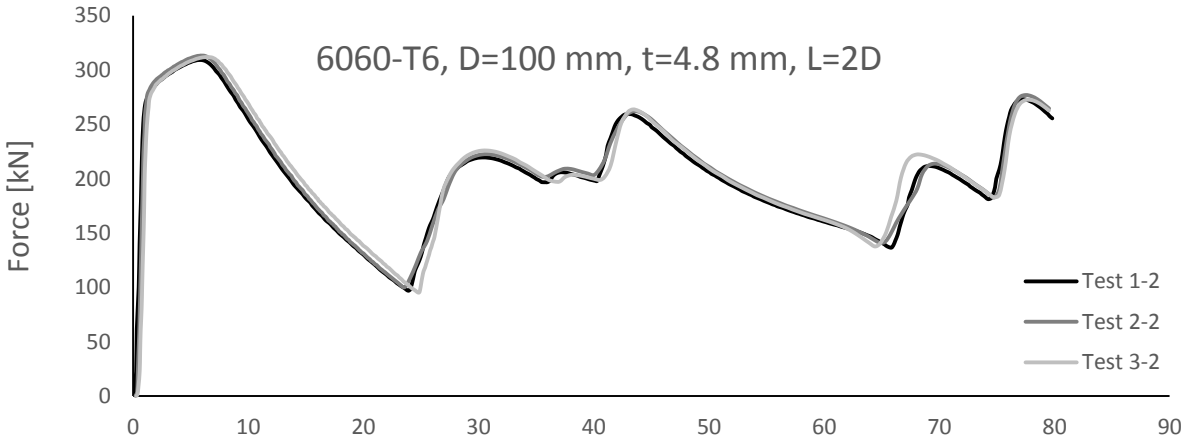

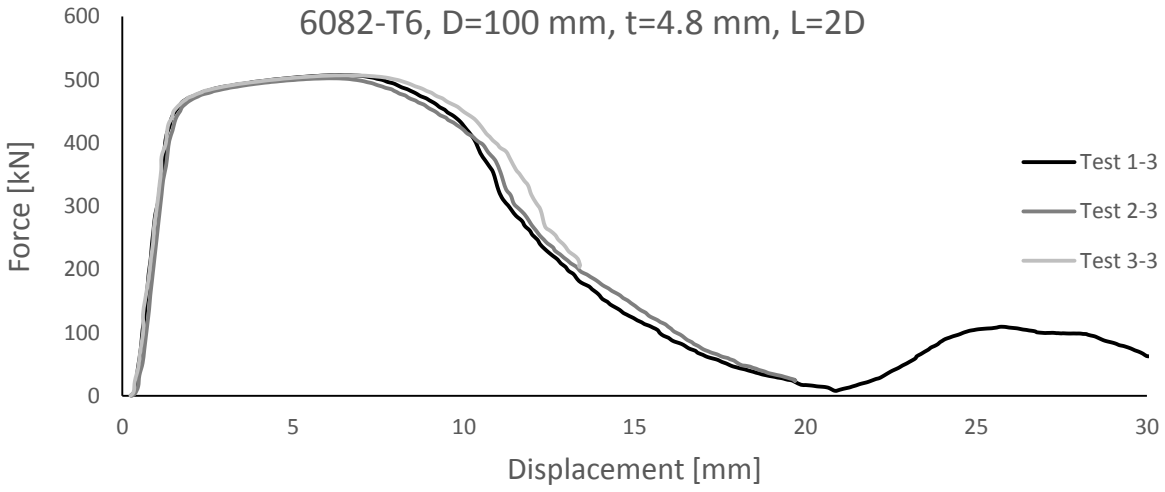

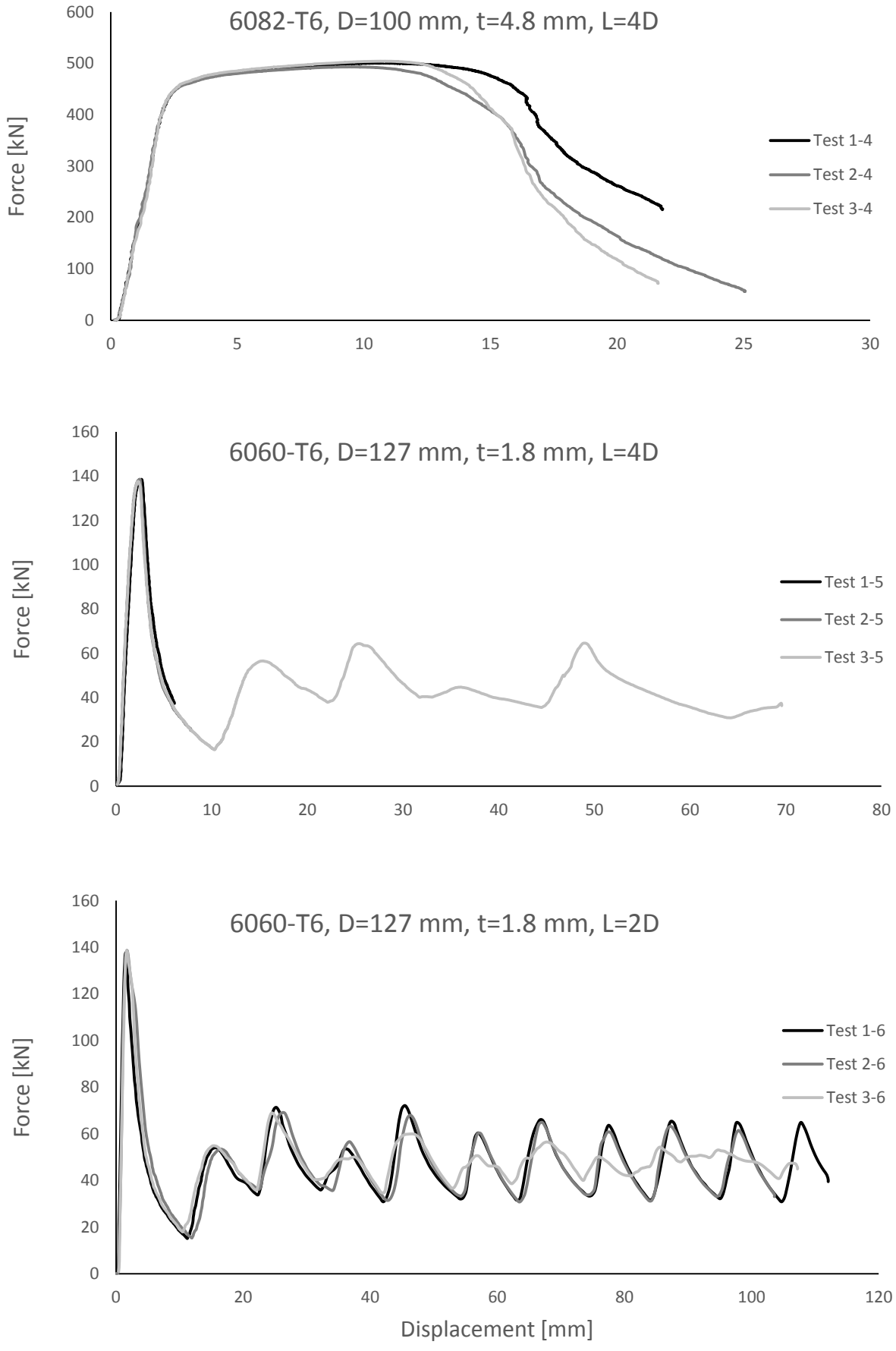

Figure G.1 – Laboratory results from stub tests for unwelded cylinders.

G.2 Welded Cylinders:

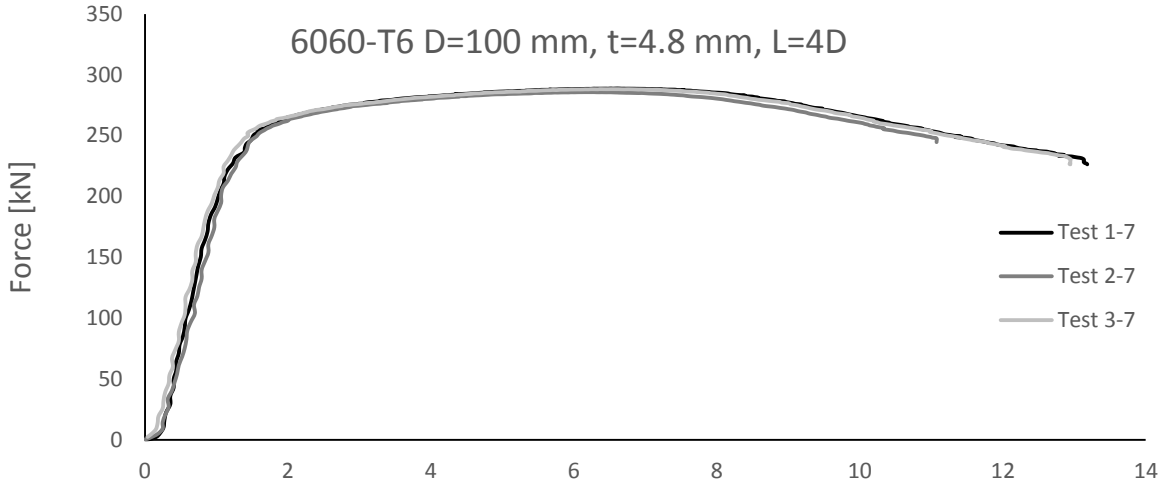

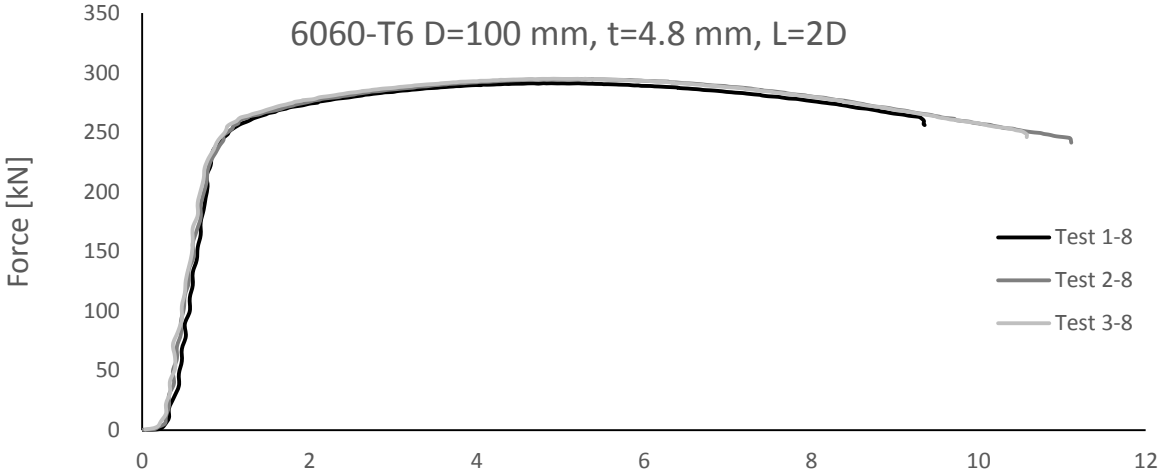

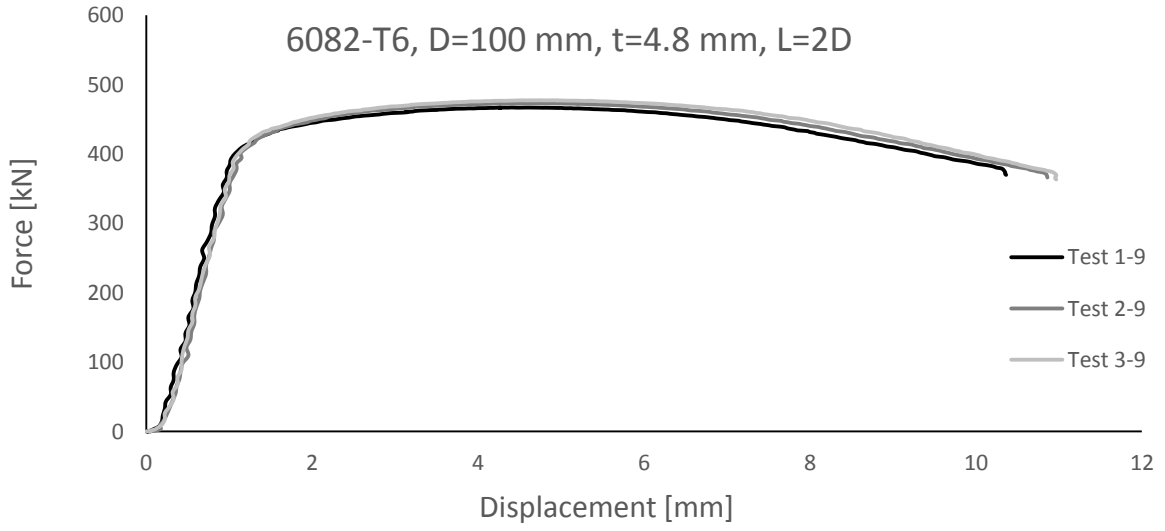

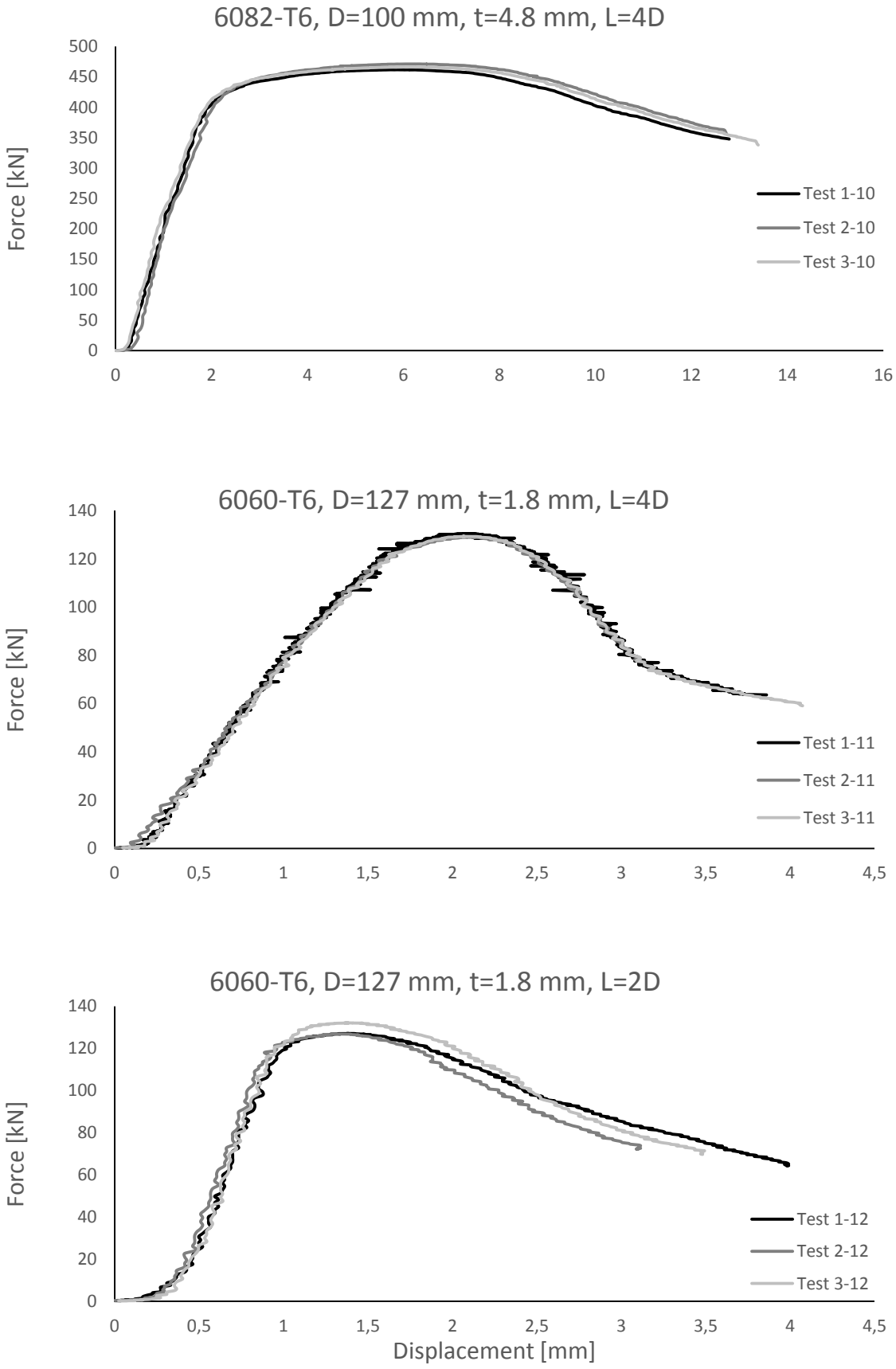

Figure G.2 – Laboratory results from stub tests for welded cylinders.

Appendix H – Measure of Stubs

H.1 Unwelded Cylinders

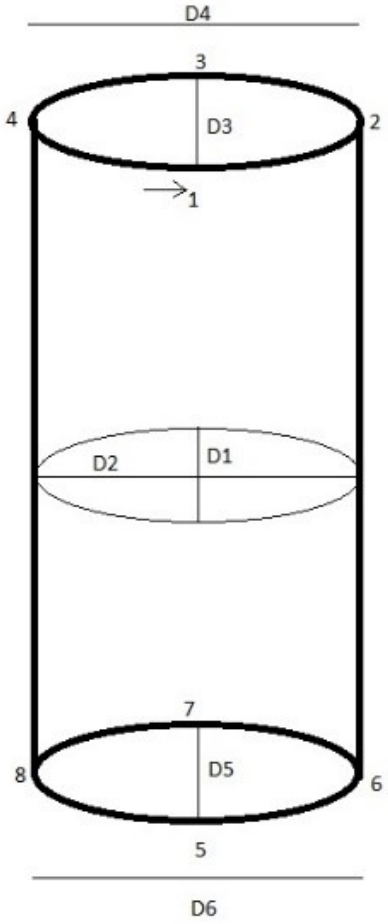

Figure H.1 – Measuring point.

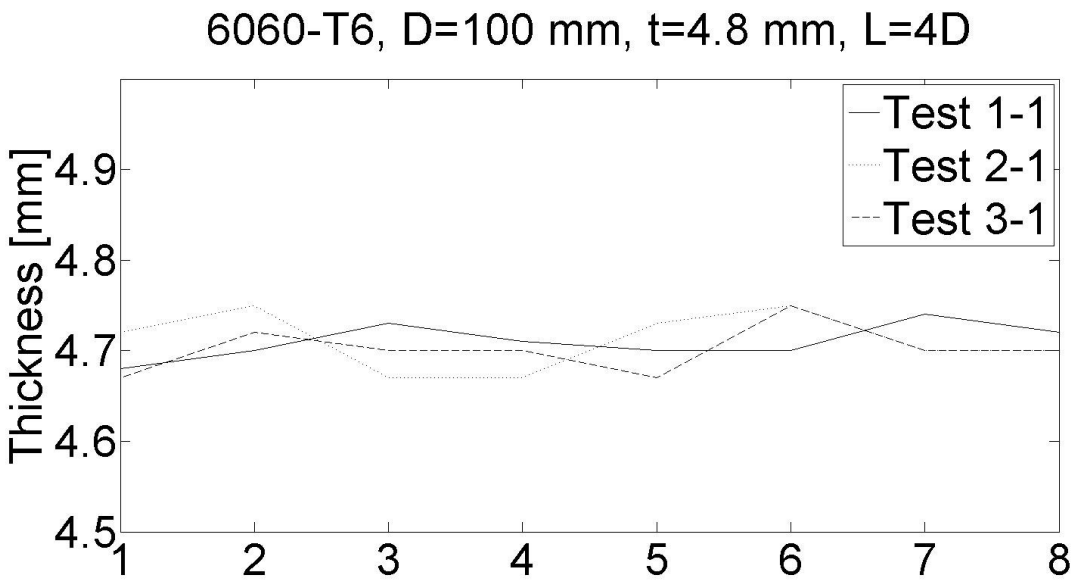
6060-T6, D=100 mm, t=4.8 mm, L=4D
Test 1-1
Test 2-1
Test 3-1
Thickness [mm]
4.5
4.6
4.7
4.8
4.9
1
2
3
4
5
6
7
8

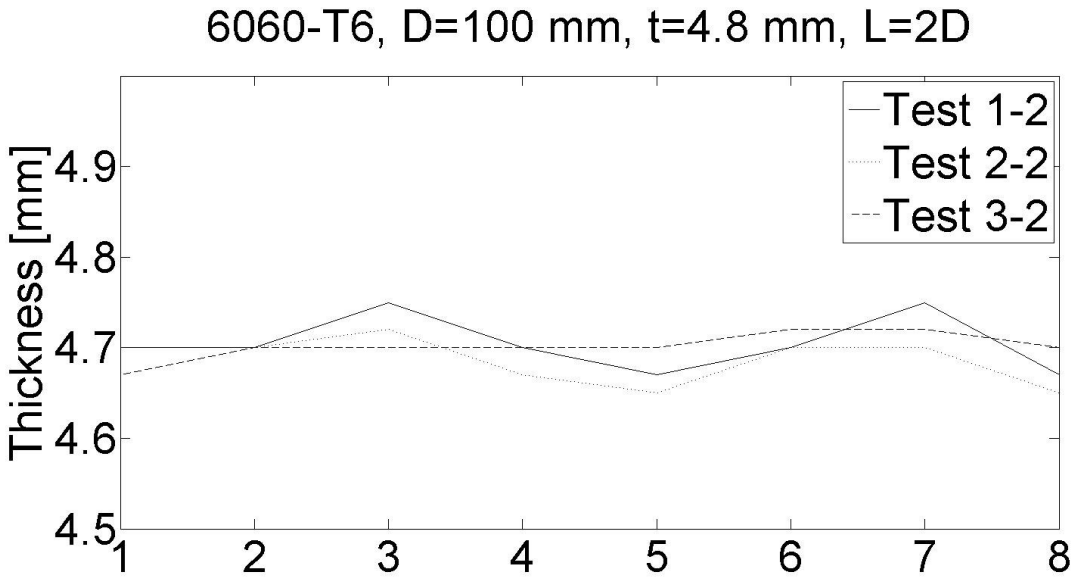
6060-T6, D=100 mm, t=4.8 mm, L=2D
Test 1-2
Test 2-2
Test 3-2
Thickness [mm]
4.5
4.6
4.7
4.8
4.9
1
2
3
4
5
6
7
8

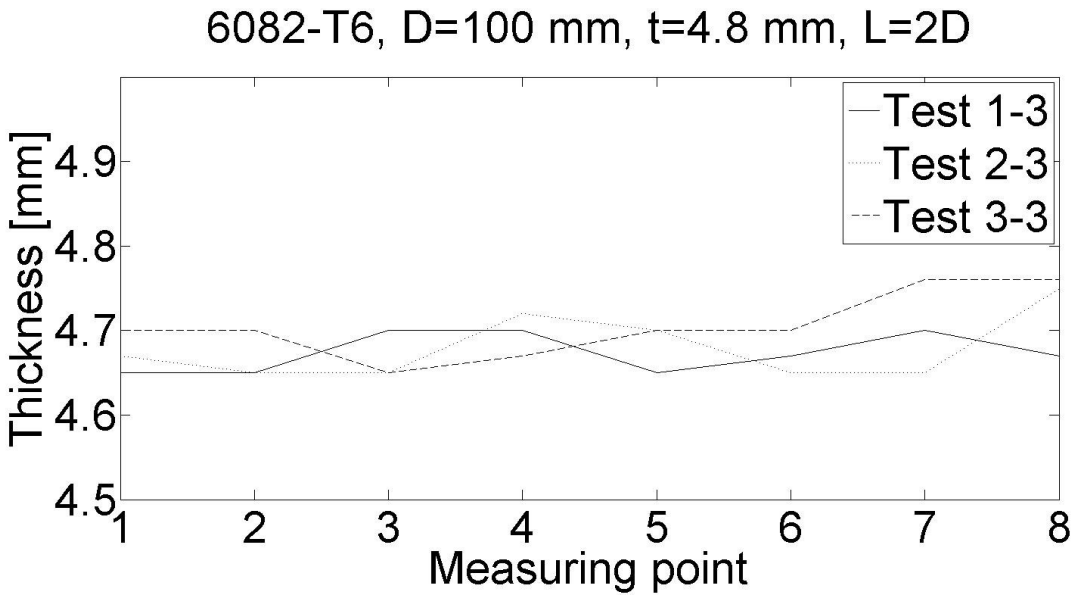
6082-T6, D=100 mm, t=4.8 mm, L=2D
Test 1-3
Test 2-3
Test 3-3
Thickness [mm]
4.5
4.6
4.7
4.8
4.9
1
2
3
4
5
6
7
8
Measuring point

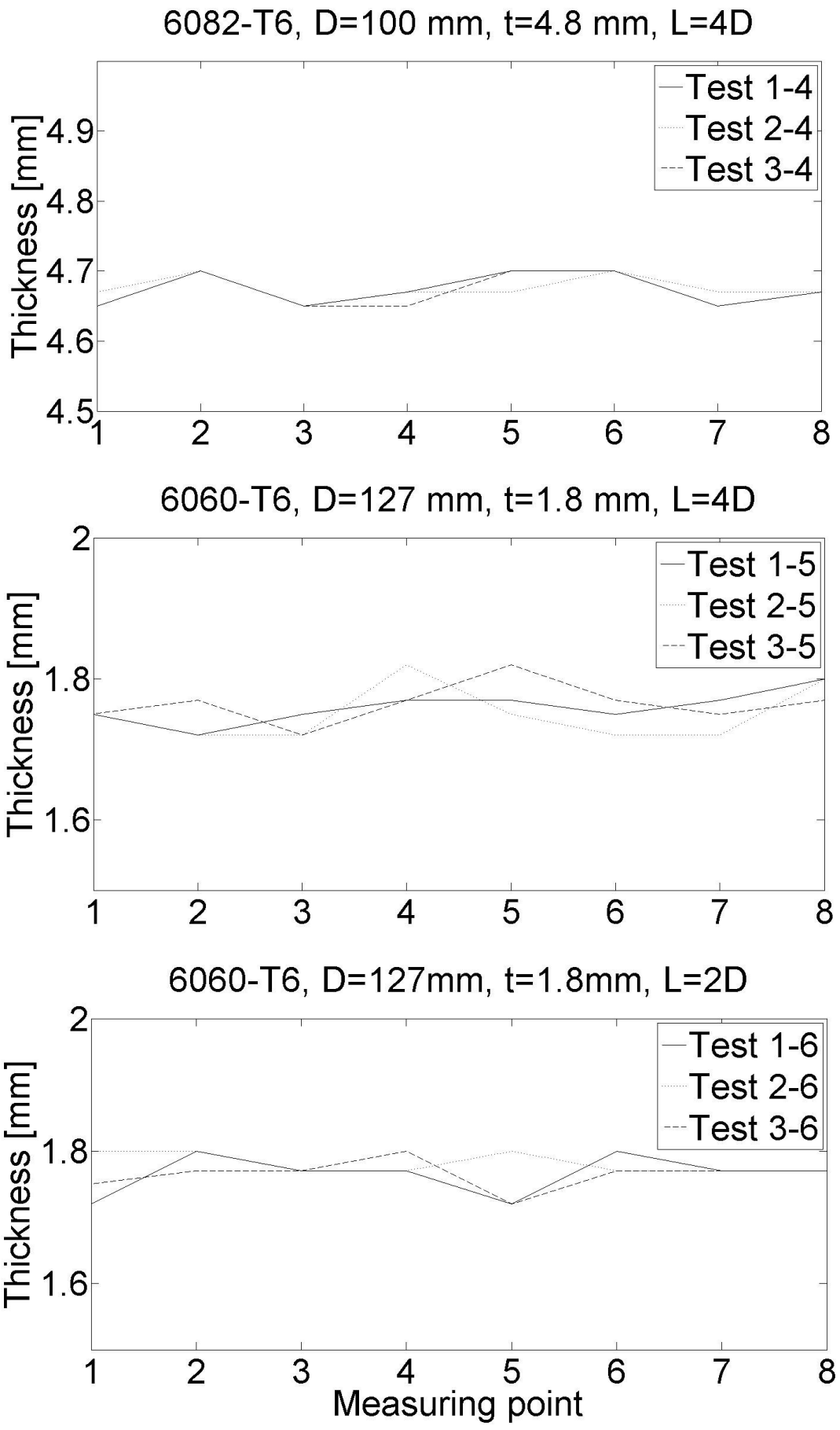

Figure H.2 – Thickness of unwelded cylinders.

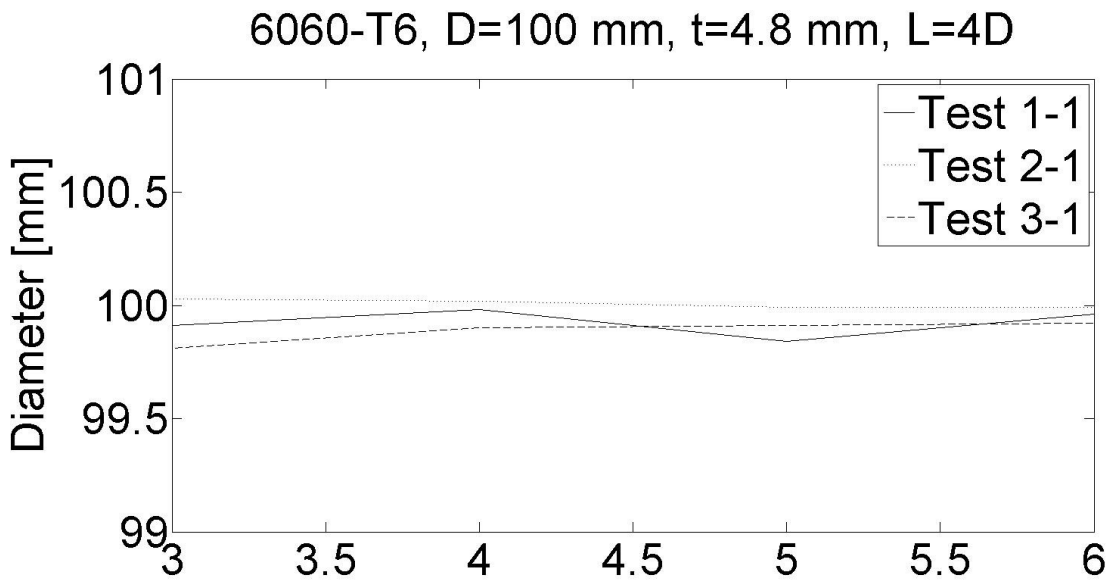
6060-T6, D=100 mm, t=4.8 mm, L=4D
Diameter [mm]
101
100.5
100
99.5
99
3
3.5
4
4.5
5
5.5
6
Test 1-1
Test 2-1
Test 3-1

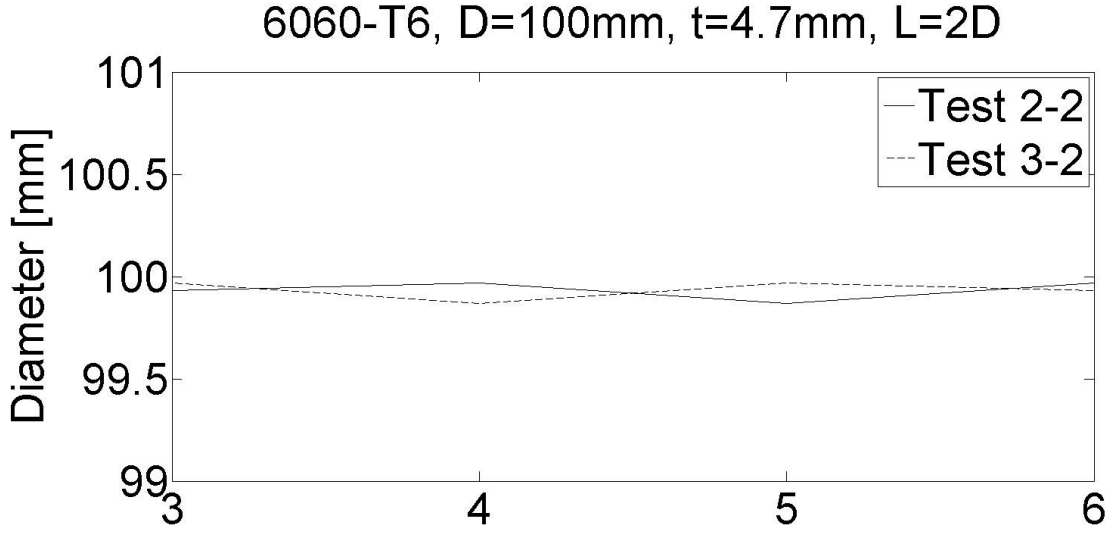
6060-T6, D=100mm, t=4.7mm, L=2D
Diameter [mm]
101
100.5
100
99.5
99
3
4
5
6
Test 2-2
Test 3-2

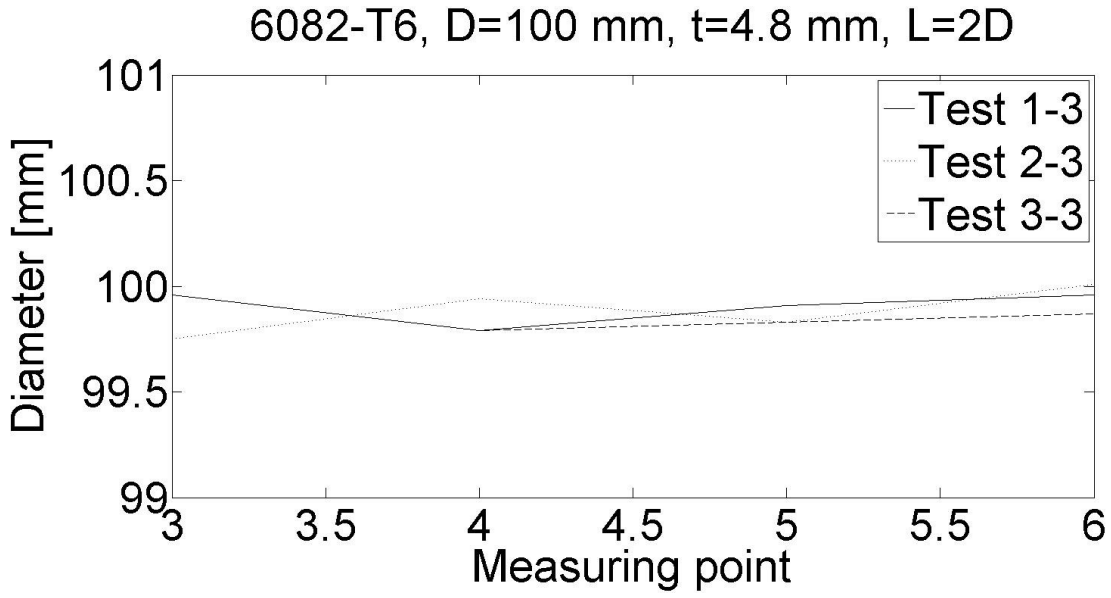
6082-T6, D=100 mm, t=4.8 mm, L=2D
Diameter [mm]
101
100.5
100
99.5
99
3
3.5
4
4.5
5
5.5
6
Measuring point
Test 1-3
Test 2-3
Test 3-3

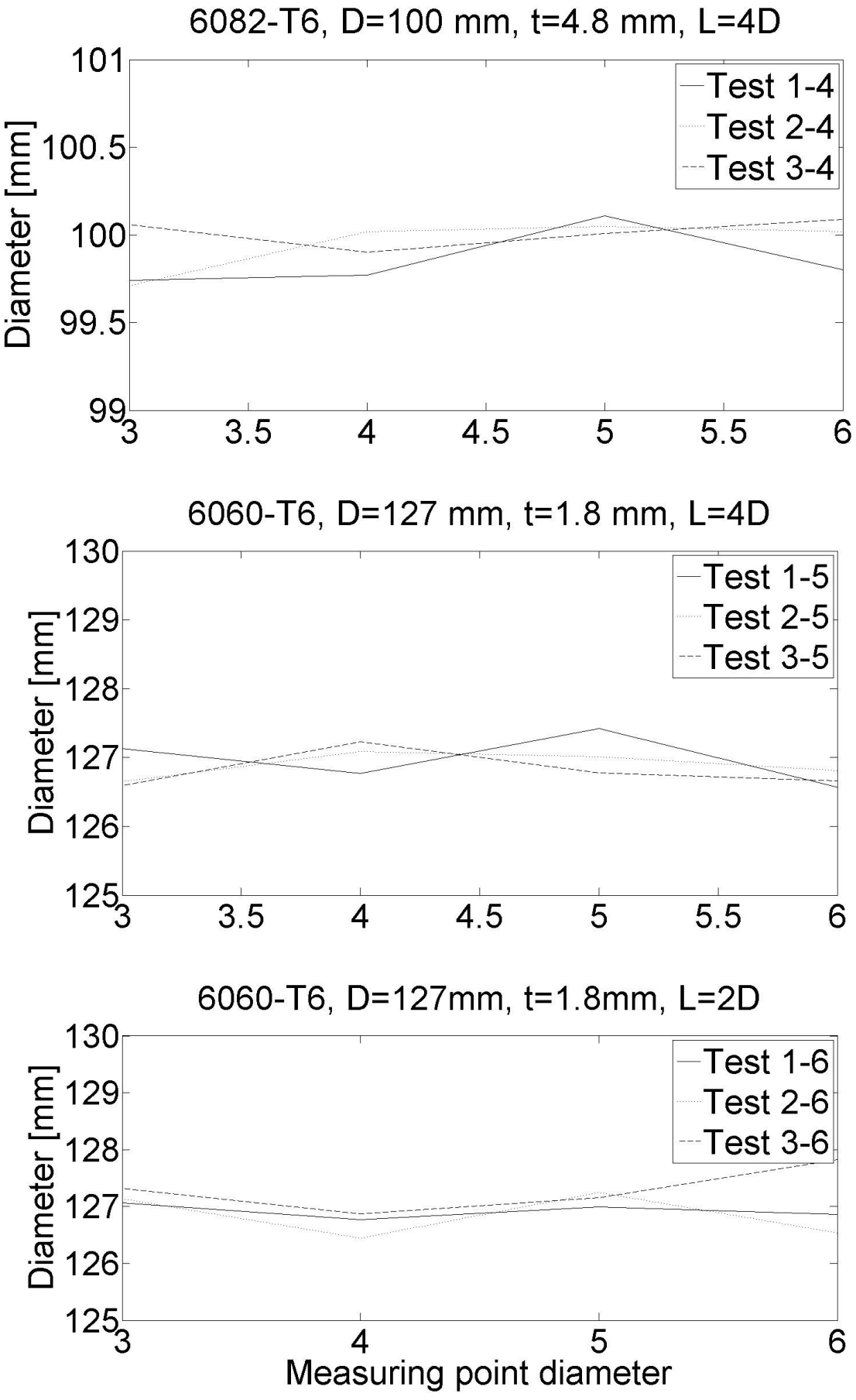

Figure H.3 – Diameter of unwelded cylinders.

H.2 Welded Cylinders

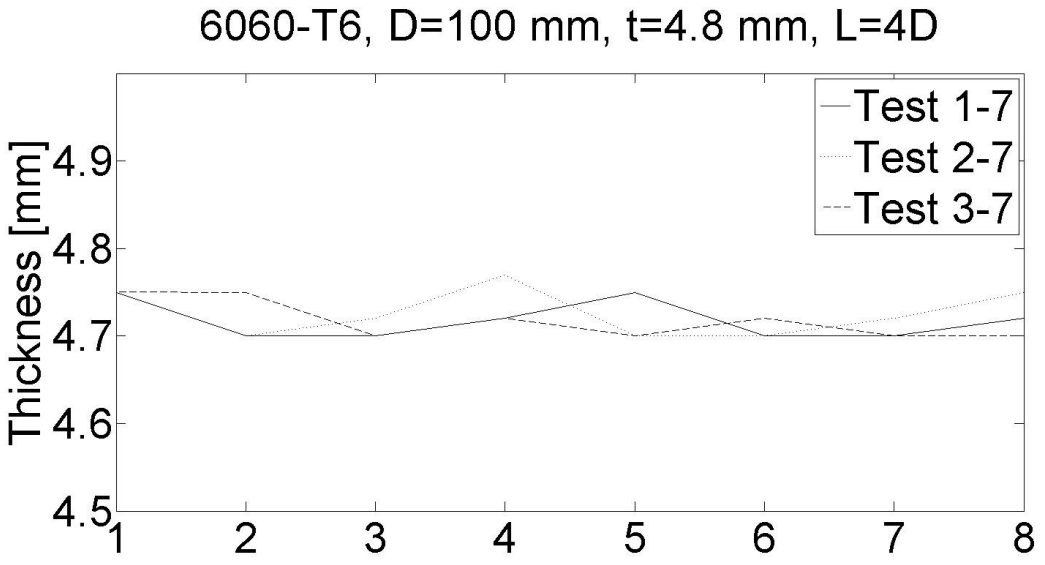

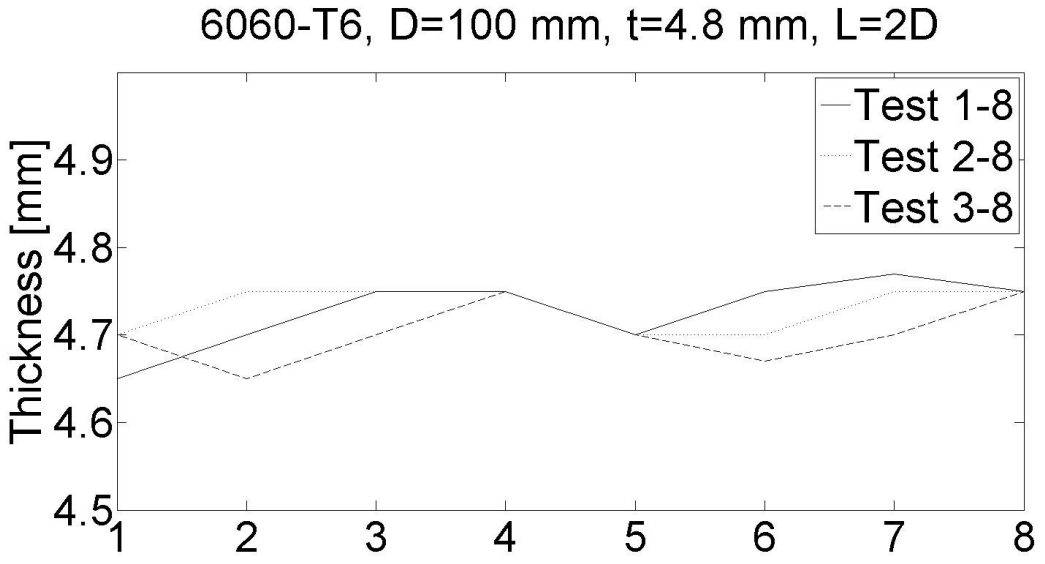

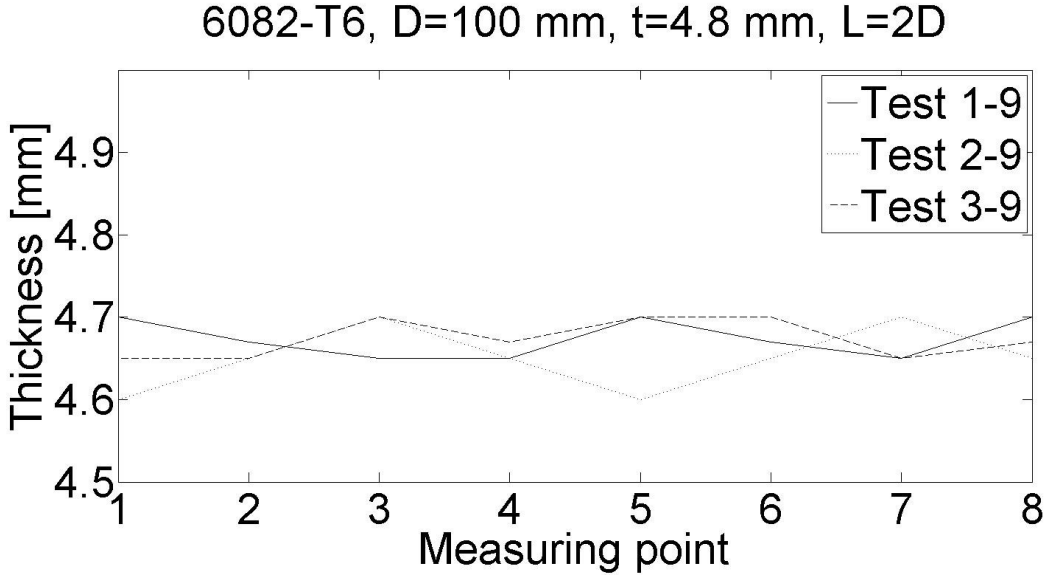

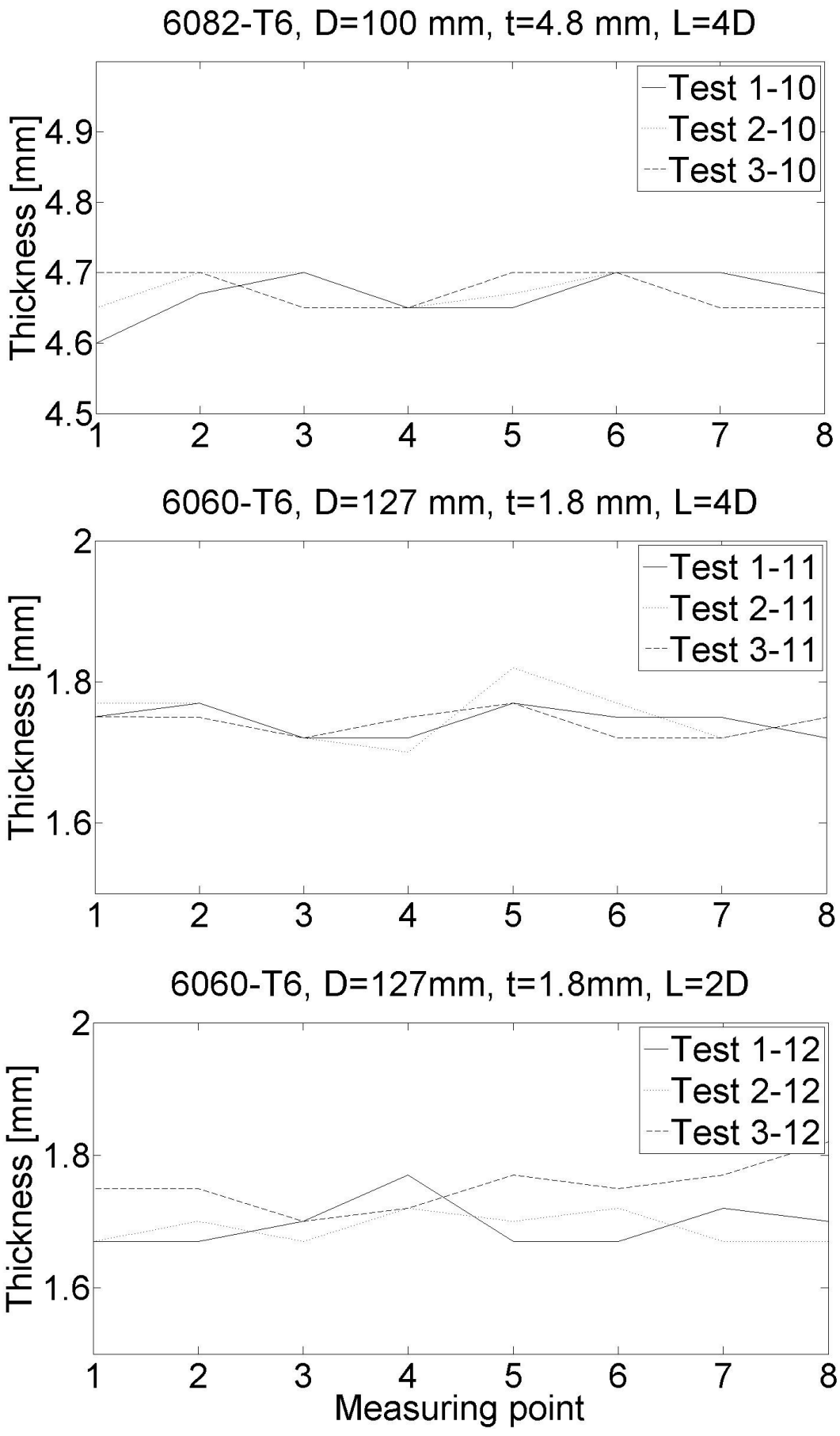

Figure H.4 – Thickness of welded cylinders.

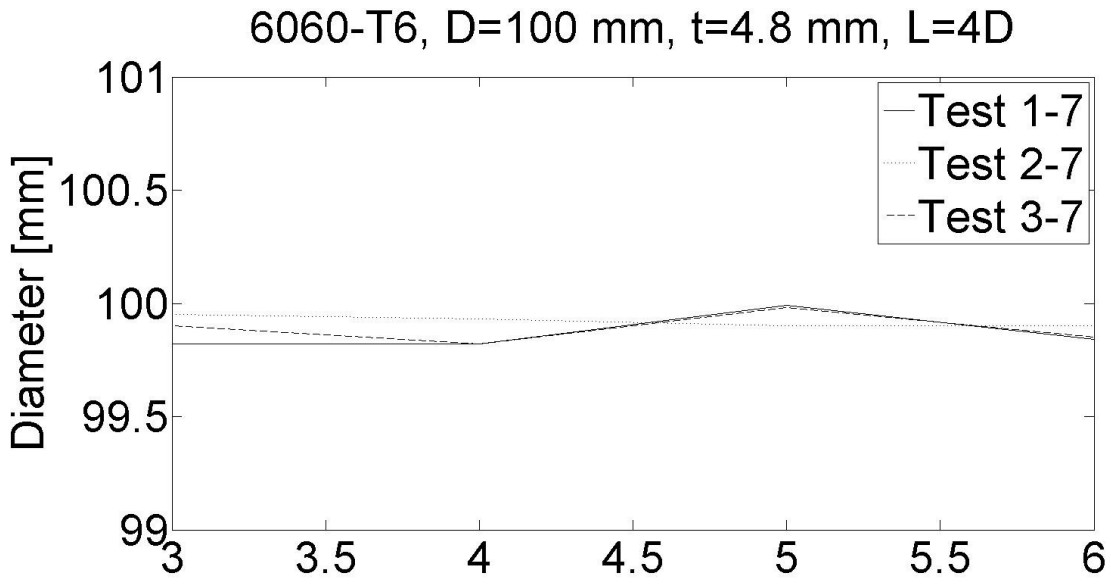
6060-T6, D=100 mm, t=4.8 mm, L=4D
Diameter [mm]
101
100.5
100
99.5
99
3
3.5
4
4.5
5
5.5
6
Test 1-7
Test 2-7
Test 3-7

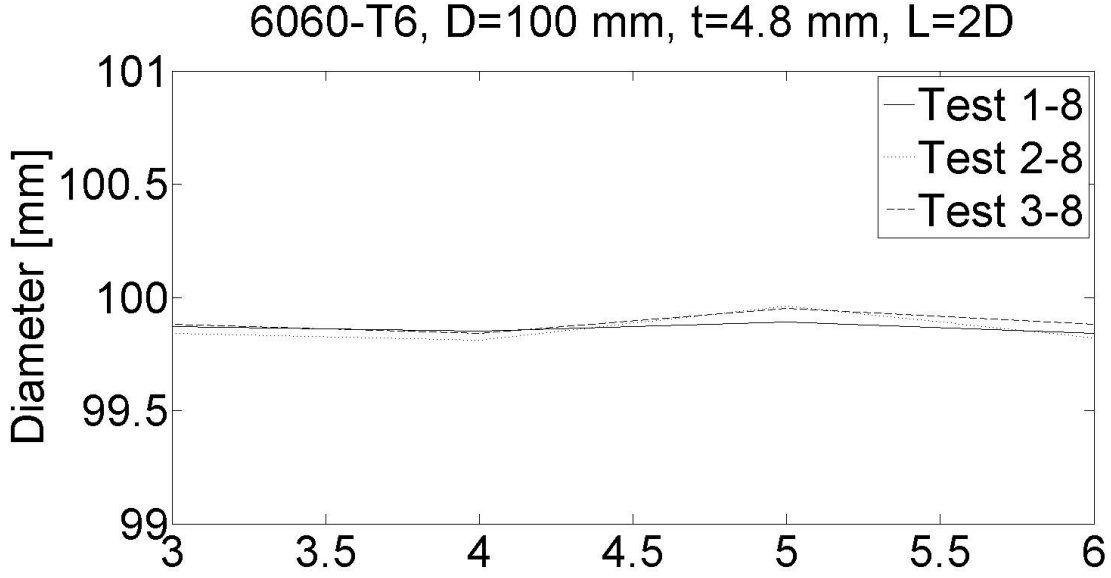
6060-T6, D=100 mm, t=4.8 mm, L=2D
Diameter [mm]
101
100.5
100
99.5
99
3
3.5
4
4.5
5
5.5
6
Test 1-8
Test 2-8
Test 3-8

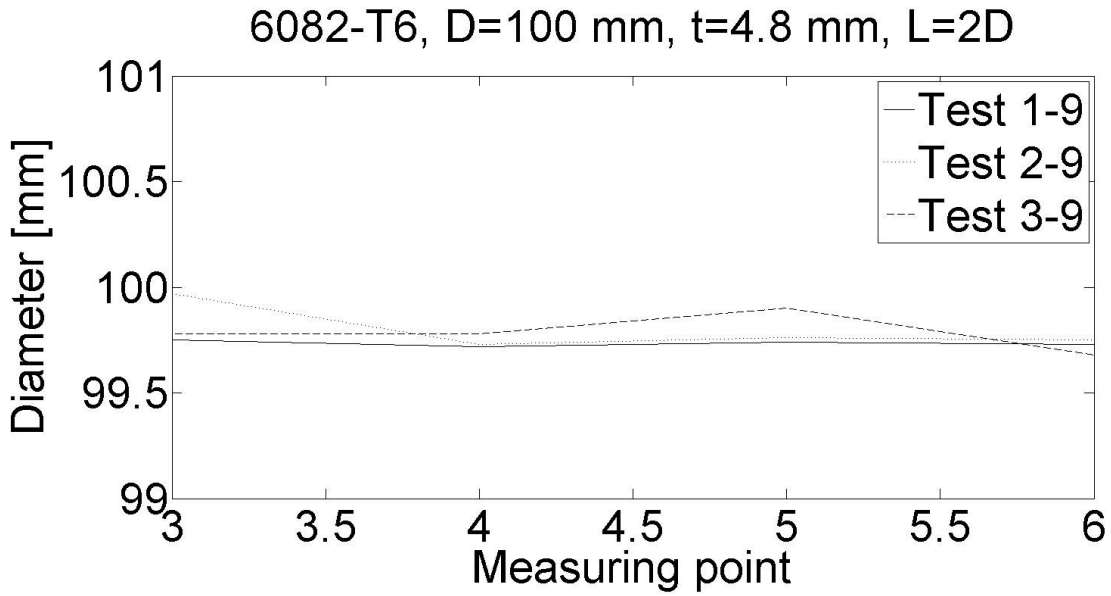
6082-T6, D=100 mm, t=4.8 mm, L=2D
Diameter [mm]
101
100.5
100
99.5
99
3
3.5
4
4.5
5
5.5
6
Measuring point
Test 1-9
Test 2-9
Test 3-9

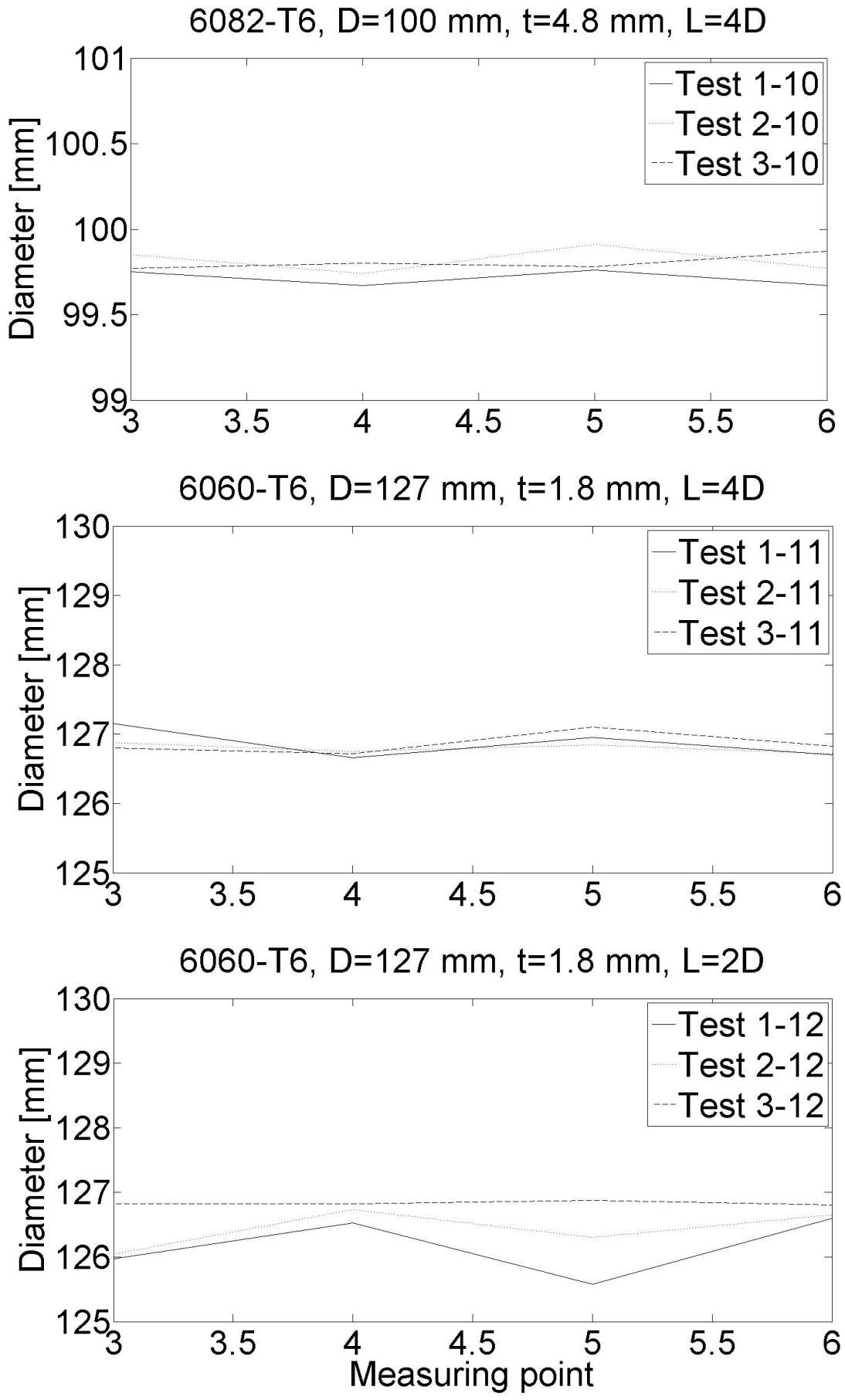

Figure H.5 – Diameter of welded cylinders.